UNIVERSITÀ DEGLI STUDI DI PADOVA

Dipartimento di Fisica e Astronomia "Galileo Galilei"

Master Degree in Physics

Final Dissertation

Studies for the next generation monolithic pixel trackers for the ALICE experiment at the CERN LHC

Thesis supervisor

Prof. Piero Giubilato

Thesis co-supervisor

Dr. Serena Mattiazzo

Candidate

Caterina Pantouvakis

Academic Year 2022/2023

Abstract

The most used sensors in the context of vertex and tracker detectors at High Energy Physics (HEP) experiments are hybrid silicon pixels sensors, in which the sensing diode and the front-end electronics are separated elements bonded together by means of bump contacts. A different design of silicon pixel sensors is emerged and is the future for inner trackers: Monolithic Active Pixel Sensors (MAPS). Both the sensing part and the front-end electronics are hosted on the same silicon wafer. This leads to a strong reduction of the material budget and of production costs, to lower power consumption, and lower noise. The drawbacks of reduced radiation tolerance and slower charge collection can be partially overcome by the implementation of depleted MAPS (DMAPS), where the width of the depletion region is enhanced. The ALICE experiment, installed at the CERN Large Hadron Collider (LHC), studies the collisions of nuclei at ultra-relativistic energies. It is the first experiment to implement MAPS on a large scale: the current Inner Tracking System (ITS2) of ALICE employs MAPS based on 180 nm CMOS technology. The goal of future ALICE upgrades is to push forward the development of MAPS improving radiation hardness and high rate capabilities, increasing depletion depth, and reducing power consumption and material budget. It aims at replacing the three innermost layers of the ITS2 with a first truly cylindrical tracker (ITS3) made of bent, wafer-scale, depleted monolithic pixel sensors based on 65 nm CMOS technology and at developing a new tracker detector for the next decade, foreseen to operate just 5 millimeters from the interaction point.

Many R&D activities on the design and characterisation of MAPS prototypes are going on. Standard and complete sensor tests are usually done at test beams at accelerator facilities; however, quicker, more affordable techniques could be very useful as test beams are expensive, logistically complicated, and nearly impossible to schedule as needed, on demand.

The goal of this thesis work was to design, implement, and validate a fully working, pulsed laser beam based table-top setup for testing MAPS. Using laser wavelengths smaller than 1100 nm, with photon energies just above the silicon band gap, the signal is induced in the MAPS under test via the emission of photo-electrons.

Contents

Executive Summary

The ALICE experiment, installed at the CERN Large Hadron Collider (LHC), studies the collisions of nuclei at ultra-relativistic energies. The goal is to study the physics of strongly interacting matter at the highest energy densities reached so far in the laboratory, at which the Quark-Gluon Plasma (QGP) forms. QGP is a deconfined state of gluons and quarks. At these high energy densities it is possible to address fundamental questions on Quantum Chromo Dynamics (QCD), such as quark confinement, and study the conditions of matter such as they were the first few microseconds after the Big Bang.

The most used pixel detectors for vertexing and tracking in High Energy Physics (HEP) experiments are hybrid silicon pixel detectors. In this type of detectors, the sensor and the front-end electronics are actually separate elements that are bonded together by means of bump contacts. A more recent technology is given by Monolithic Active Pixel Sensors (MAPS). In this case, both the sensing part and the front-end electronics are hosted on the very same silicon wafer. The sensing volume of conventional MAPS is a thin (10-20 µm) high resistivity epitaxial layer; CMOS transistors can be integrated on a thin, highly doped layer on top of that.

MAPS show a lower power consumption, lower noise, present a lower material budget, and they are less expensive, since they do not require complex techniques as the bump bonding in hybrid pixels. However, they are less radiation tolerant and they are slower due to the fact that the charge is collected mainly by diffusion in the small locally depleted region around the collecting diode. These issues can be partially overcome by the implementation of Depleted MAPS (DMAPS) where charge collection happens by drift in larger depletion widths yielding larger and faster signals [6].

The current Inner Tracking System (ITS2) of ALICE employs MAPS based on 180 nm CMOS technology. The sensor is the ALPIDE chip, a matrix of 1024×512 pixels covering an area of 30×15 mm^2. This is the first large-scale implementation of MAPS. The goal for future ALICE upgrades is to push forward the development of MAPS improving radiation hardness, high rate capability, increasing depletion depth, further reducing power consumption and material budget. As a first step, the ALICE experiment aims to replace the three innermost layers of the ITS2 with a first truly cylindrical tracker (ITS3) made of bent, wafer-scale, depleted monolithic pixel sensors based on 65 nm CMOS technology [3]. In addition, the ALICE experiment is now looking forward to starting the design phase of a completely new detector for the next decade (ALICE3). The new detector will embody the most advanced pixel tracker in the world, foreseen to operate just 5 mm from the interaction point in the LHC beam-pipe: to reach that proximity, the first three layers of the tracker will be housed within the vacuum pipe itself, posing enormous technical challenges [4].

Several studies can be performed on MAPS in order to characterise them. Standard and complete tests are usually done at test beams at accelerator facilities; however, they are time consuming and expensive. It is therefore desirable to have the possibility to carry out characterisation studies using quicker and more affordable techniques. This is particularly useful during the sensor R&D phase, when many different chip flavours and versions are produced. The testing campaign would be unmanageable and expensive if only performed through test beams.

This thesis work is focused on the design and implementation of an optical setup with a pulsed laser beam to test and characterise MAPS. The goal of the project is to validate the experimental setup in

order to have a fully working and stand-alone structure available in the laboratory.

Laser beams in the IR region with wavelength smaller than 1100 nm have an energy just above the silicon band gap, thus inducing signal via the emission of photoelectrons in the sensitive volume. The absorption length in silicon depends on the wavelength.

In my thesis work, two wavelengths are discussed: 910 and 1060 nm. The first one is characterised by a small absorption length and can be used in tests of fully depleted MAPS that can be illuminated from the backside; the latter one is interesting because it has absorption length much larger than the typical sensor thickness, hence the charge density it creates along the whole detector thickness is uniform. By tuning the power of the incident laser beam, one can emulate the charge released in the sensor by a Minimum Ionizing Particle (MIP).

For what concerns the design of the optical setup, the key elements that are fundamental to control the beam are the optical components, i.e. optical fibres and diaphragms, used to attenuate the beam to avoid pixel saturation. In addition, the spot size has to be comparable with the pixel size; therefore, the beam focusing is extremely important. Microscope objectives are used to focus the beam on the sensor to achieve a small laser spot size. The setup is mechanically mounted in order to have the sensor lay horizontally. The optics can be moved along the vertical direction to optimise the beam focusing on the sensor surface. Using a mirror and a beam splitter, the optical setup includes a camera with a coaxial illumination system to monitor the position of the device under test. In addition, a photodiode is used to simultaneously measure the beam power in order to check the laser power stability while operating.

After the characterisation of the setup, measurements were made to validate the system. The device under test, for the measurements presented in this work, was the MATISSE chip. MATISSE is based on 110-nm CMOS technology by LFoundry, designed and produced in the context of the INFN SEED and ARCADIA collaboration. It is a 300 μm thick 24×24 fully depleted pixel matrix, covering an area of 2×2 mm^2, with a pixel cell size of 50 μm.

The thesis work is organised as follows: in Chapter 1, there is a description of the ALICE experiment with main focus on the implementation of MAPS in the Inner Tracking System. Chapter 2 provides a description of silicon pixel sensors and of the interaction of low-energy photons in silicon. In Chapter 3, the experimental setup and its characterisation are presented. Chapter 4 is devoted to the description of the chip MATISSE, and the measurements and results are given in Chapter 5. In Chapter 6, final conclusions and some ideas for future development will be drawn.

Chapter 1

ALICE Experiment

In this chapter, after a brief overview of the ALICE experiment, the tracking system is described in detail focusing on the current design and future upgrades that are strongly based on the development of Monolithic Active Pixel Sensors (MAPS).

1.1 Overview of ALICE experiment

The ALICE experiment (A Large Ion Collider Experiment) at the LHC is devoted to the study of strongly interacting matter. ALICE studies what happens in heavy-ion collisions (e.g. Pb-Pb and p-Pb), in addition to p-p collisions which are instead the exclusive focus of the other three experiments at LHC.

In ultra-relativistic heavy-ion collisions, a very high temperature and high density quark-gluon plasma (QGP) is formed. QGP has properties that are very different from those of ordinary hadronic matter, as it is dominated by partonic dynamics, where quarks and gluons are de-confined. The study of QGP therefore provides the opportunity to test Quantum Chromo Dynamics (QCD), the gauge theory of strong interaction. Furthermore, QGP investigations are also of great interest for cosmology, as a few microseconds after the Big Bang the Universe was in such a state, a state that can be only accessed in heavy-ion collision at accelerators [5].

Nuclei are much more extended objects with respect to nucleons (protons, neutrons) and collisions between two nuclei can be usually treated as an overlap of independent nucleon-nucleon interactions. The fundamental parameter to characterise events in terms of nucleon-nucleon collisions is the impact parameter. Central collisions are characterised by a small impact parameter; peripheral collisions have a very large impact parameter.

The centrality of heavy-ions events are classified on the basis of a few observables that can be measured since the impact parameter is an indirect observable. These direct observables are the multiplicity of charged particles, the transverse momentum at midrapidity, and the energy measured in the forward rapidity[1] region [10].

The physics goals of the ALICE collaboration in the field of QGP physics are expressed in terms of requests on these observables, that then translate into performance requirements on the different components of the ALICE detector. Particularly essential are: high readout rate capabilities; excellent resolution and efficiency; tracking and vertexing capabilities, especially at low transverse momentum; very good particle identification [4].

The ALICE detector, the schematic of which is shown in Fig.1.1, is made of several subdetectors. Currently, the full detector is structured as follows:

[1] In hadron collider physics, rapidity is used, instead of the polar angle, as a spatial coordinate. Rapidity differences are Lorentz invariant under boosts along the beam axis.

- Tracking and Particle Identification
  - Silicon vertex detector Inner Tracking System (ITS)
  - Time Projection Chamber (TPC) for charged particles momentum tracking and identification
  - Transition Radiation Detector (TRD) for fast electrons identification
  - Time Of Flight (TOF) and High Momentum Particle Identification Detector (HMPID) for hadron identification
- Energy
  - Electro Magnetic Calorimeter (EMCal) and Photon Spectrometer (PHOS) for electron and photon energy measurement
- Muons
  - Muon Forward Tracker (MFT) and Muon Spectrometer for muon tracking and vertexing
- Triggering and global characteristics
  - Detectors for trigger as: Fast Interaction Trigger (FIT), which is made of three sub-detectors (FV0, FT0, and FDD)
  - Detectors for multiplicity, centrality and event plane determination, as the Forward Multiplicity Detector (FMD), Photon Multiplicity Detector (PMD) and Zero Degree Calorimenter (ZDC) and a veto detector, Alice COsmic Rays Detectors (ACORDE), to reject cosmic rays events.

The central barrel is placed inside a solenoid magnet, that generates a magnetic field of 0.5T, whereas the muon sector is placed on an external arm.

After the Long Shutdown 2 (LS2), which took place from 2018 to 2022, several parts of ALICE detector underwent a significant upgrade in order to improve readout rate and tracking capabilities, making it possible to study very short-lived systems, such as low-mass dileptons, quarkonia or heavy-flavour hadrons.

The new subdetectors have been installed, and the ALICE experiment is currently undergoing the Run 3 of data taking.

This upgrade has seen, for the first time, the use of Monolithic Active Pixel Sensors (MAPS) on a large scale, for a total coverage of about 10 m^2 of area, as it will be detailed in the next section.

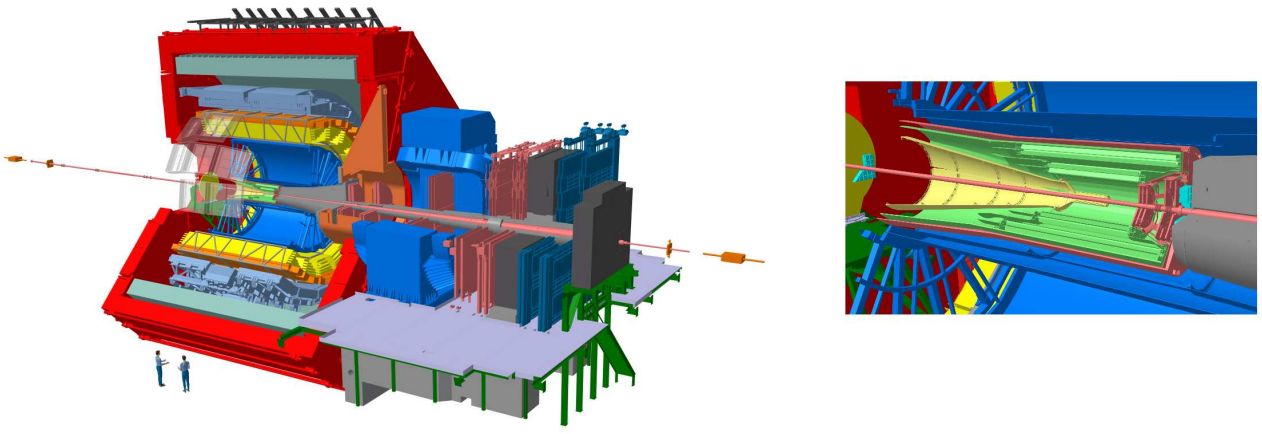

Figure 1.1: ALICE schematic and ITS2 schematic, taken from [19]

1.2 Inner Tracking System

1.2.1 Tracking and vertexing

The tracking system is of fundamental importance for event recostruction.

The basic principle in tracking a charged particle is to use a number of position measurements, using non-destructive minimally perturbing detectors, organised in layers, to reconstruct the track of a charged particle with high pointing resolution. When the tracking system is placed inside a magnetic field, the charge and the momentum of the particle can be determined.

Tracking algorithms correlate hits detected in the different tracking layers related to the same particle. When the track is reconstructed, the charge and momentum of the particle can be obtained. Vertexing is instead the reconstruction of secondary vertices of any tracks left by charged decay products of unstable particles produced in primary interactions; this detailed reconstruction is essential in order to characterise the topology of the decays.

In the case of pixel trackers, the momentum, impact parameter, and point resolution are all related to the spatial resolution of the pixel detector.

Two fundamental quantities determine spatial resolution: the pitch of the pixels p and the number of tracking layers N. Being σ_{pix} the spatial resolution of a single pixel layer, the resolution of the full tracker scales as:

$$\sigma \propto \frac{\sigma_{pix}}{\sqrt{N-1}}$$

In the simplest case of binary readout and a particle generating signal only in one pixel per layer, the spatial resolution is given by:

$$\sigma_{pix} = \frac{pitch}{\sqrt{12}}$$

In case of a cluster of firing pixels, the resolution is improved. Anyway, the pixel pitch is the quantity which determines the pixel intrinsic resolution.

As a consequence, there are two main approaches to improve spatial resolution: a smaller pixel size and a larger number of tracking layers.

Another important element that plays a role in the tracking and vertexing resolution is multiple scattering.

Particles traversing several media, both active and dead layers, scatter, and this affects the momentum resolution. To reduce this effect, the material budget has to be very small.

1.2.2 ITS2

As declared in the Letter of Intent of the ALICE upgrade during the LS2, the physics programme focuses on rare probes and their interaction with the medium, in particular heavy-flavour particles, quarkonia, real photons, and low-mass dilepton and jets. In addition, ALICE also aims at studying exotic heavy nuclear states. To do so, measurements with high precision and high statistics in particular at low transverse momentum are needed. The vertexing and tracking performance at low momentum and readout rate of the detector must be improved, keeping the same particle identification capability [5].

The current tracker is the Inner Tracking System 2 (ITS2) which has replaced the previous ITS, representing one of the major upgrades of the detector.

During LHC Run 1 and Run 2, the ITS was made of six layers implementing different types of silicon detectors: hybrid pixel, drift and strip detectors.

The ITS2 was designed in order to have several improvements with respect to the previous ITS [14].

- The number of tracking layers has been increased from six to seven.

- The innermost layer is moved closer to the interaction point, from 39 mm to a radial distance of 23 mm.
- The material budget of the inner layers is reduced from 1.14% to 0.35%X_0.
- The ITS2 is completely made of MAPS. The pixels are much smaller and the granularity of the detector is enhanced. For comparison, in the previous ITS, the cells of the hybrid pixel cells were 50×425 μm^2, while the ITS2 implements the ALPIDE chip with a pixel size of 29.24×26.99 μm^2.
- The readout rate is enhanced by a factor 100 in Pb-Pb and 200 in pp collisions.

With this design, the resolution of the impact parameter, the tracking and vertexing efficiency and the transverse momentum resolution at low transverse momentum are improved [14].

ITS2 is totally based on silicon MAPS and is the tracker detector with the smallest pixel size of all LHC experiments, as can be seen in Tab.1.1. The full tracker hosts 12.5×10^9 pixels.

The layout is shown in Fig.1.2. The Inner Barrel is made up of three layers. Four additional layers constitute the Middle and Outer Barrel. Each layer is made of detector modules called staves, which consist of the carbon fibre support, the cold plate, the flexible printed circuit and the pixel chips. The

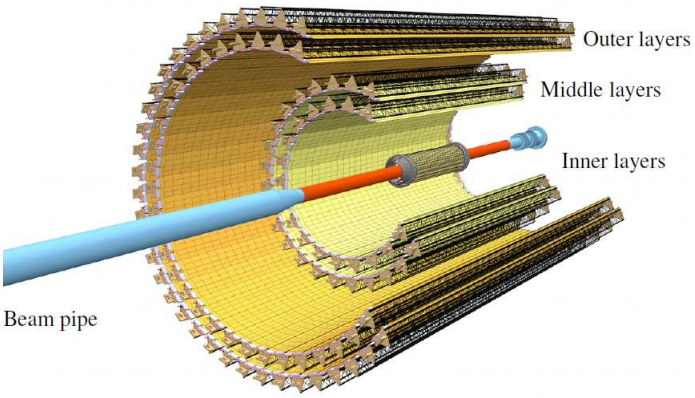

Figure 1.2: ITS2 scheme [14]

basic element of the ITS2 is the MAPS chip ALPIDE (ALice PIxel DEtector). The sensitive volume is represented by a p- epitaxial layer on top of a p++ substrate. CMOS electronics for readout are hosted on top, exploiting a pwell for the NMOS transistor and a deep pwell for the PMOS transistors.

Table 1.1: ALPIDE chip characteristics [14]

Technology	TowerJazz 180 nm CMOS
Pixel area	29.24 μm × 26.88 μm
Chip size	15 mm × 30 mm
Spatial resolution	5 μm

The ALPIDE chip is the sensor which the Muon Forward Tracker (MFT) is also based on. The MFT is a subdetector installed during the LS2 as the ITS2 in order to enhance the muon tracking and vertexing capabilities. The muon tracks in MFT are then matched with the muon tracks in the muon spectrometer. The MFT has a cone structure formed by ten half-disks, on which the chips are hosted, placed in front of the absorber inside the ITS Outer Barrel.

As will be further described in the next section, the ALICE experiment and R&D projects for next upgrades are strongly pushing the development of innovative MAPS.

1.3 Further upgrades

1.3.1 ITS3 upgrade

During the Long Shutdown 3 (LS3 2026−2028), the Inner Barrel of ITS2 is planned to be replaced by the Inner Tracking System 3 (ITS3).

It will be the first truly cylindrical wafer-scale MAPS vertex detector.

Each inner layer of ITS2 will be replaced by two half-layers. The design concept of the ITS3 is shown in Fig.1.3.

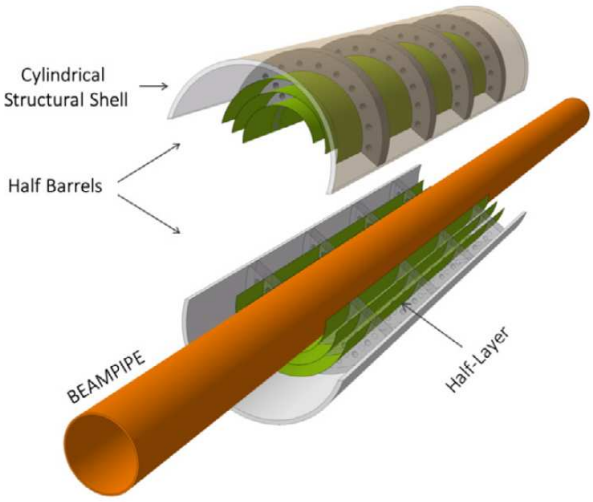

Figure 1.3: ITS3 conceptual design [3]

This design can be achieved applying the industrial technique of stitching to get wafer-scale chips. Stitching is a technique based on the periodic repetition of reticles that slightly overlap. In this way, it is possible to create a single sensor that covers the full length of the half-layer that is 280 mm.

A wafer-scale sensor allows to have a very large pixel matrix that constitutes the sensitive area whereas all the peripheral circuits can be placed on one side. The idea is to replace the 180 nm with 65 nm CMOS technology which implements 300 mm silicon wafers. In this way, it is possible to get a whole half-layer from a single wafer. The chip design has to be optimised to be able to use a smaller size technology. However, this also provides the advantage of even lower power consumption, making it feasible to use only air cooling in the sensitive area. The ITS2 water cooling system will be kept for the cooling of the peripheral part.

The other key challenge is to achieve a thickness of the pixel sensors of the order of 20−40 µm. With a reduction in the thickness, the flexibility of the sensor is greatly increased. Several bending tests of the sensors have already been successfully performed up to the planned bending radius for the innermost layer, which is planned to be equal to 18 mm, focussing both on the mechanical and electrical characterisation. Bent sensors are much stiffer, and this allows the implementation of a much lighter mechanical support based on carbon foam. These are the principles on which the concept of the first truly cylindrical tracking detector is based.

Moreover, the beampipe will be replaced by a thinner beryllium beampipe. Therefore, the innermost layer will be at a smaller radial distance from the IP, from 23 down to 18 mm.

All these improvements will lead to an extremely reduced material budget down to $0.05\%X_0$ per layer, to an improvement of the spatial resolution and tracking efficiency enhancing the performance in terms of heavy-flavour hadrons and low-mass dielectrons detection [3].

1.3.2 ALICE3 experiment

The concept of the ALICE3 experiment has been submitted to set the goals for the next decade of the new ALICE detector to further improve detection performance. The scheme can be observed in Fig.1.4.

Inside the superconducting solenoid, there are four sub-detectors for tracking and particle identification: the MAPS-based tracker, the TOF layers, the Ring Imaging CHerenkov detector (RICH) and the electromagnetic calorimeter (ECal). An additional dipole magnet hosts the Forward Conversion Tracker (FCT) for tracking in the forward rapidity region. Moreover, in the central region outside the magnetic field and right after a thick absorber, the muon detector is located.

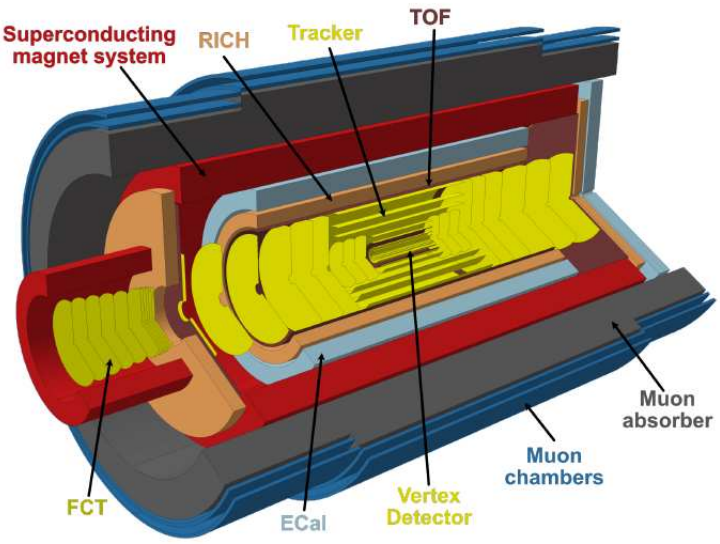

Figure 1.4: ALICE3 Detector concept scheme [4]

As it can be seen in Fig.1.5, the tracker is divided into two detectors: a Vertex Detector conceived to be made of three forward disks on both sides of the IP and three cylindrical layers; an Outer Tracker made of eight layers and nine forward disks per side. One of the most innovative and challenging ideas

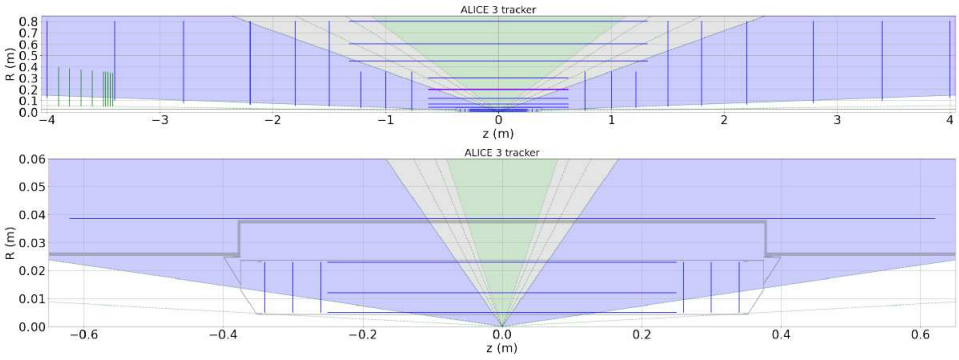

Figure 1.5: Top: Concept design of ALICE3 full tracker. Bottom: Concept design of ALICE3 Vertex Detector [4]. The blue lines represent the tracker layers. The z-axis represents the beam direction, with the interaction point located at (0,0). R is the radial distance.

is the placement of the inner tracker inside the beampipe in order to be as close as possible to the interaction point for primary vertexing. The minimum of the radial distance is set by the aperture required for the LHC colliding beams, which depends on the energy. At the injection, it is $\sim$ 15 mm whereas it goes down to 5 mm at the maximum of the energy.

The idea is to design the innermost layer in order to be retractable. In this way, it could be set in place after the beam has reached the maximum energy. This requires the vertex detector to be mounted inside a secondary vacuum within the beam pipe.

A design that has been suggested is a sort of iris optics diaphragm made by assembling the sensors in four petals-like layers.

In addition to the work on the improvement of the pointing resolution, there are several aspects on which studies are being carried out. There are stringent requirements on material budget, hit time and spatial resolution, rate capability, power consumption, and radiation hardness.

The reference technology is represented by CMOS MAPS and the starting point is the development that has been carried on in the ITS2 and ITS3 projects taking into consideration that the two subdetectors need different sensor designs:

- Vertex Detector: wafer-scale sensors with very high position resolution.
- Outer Tracker: reticle-size sensors with good position resolution.

In order to reach the ambitious and challenging goals of ALICE3, many R&D projects focusing on different aspects of MAPS are going on giving the possibility of exploring new conceptual designs and developing prototypes [4].

Chapter 2

Silicon Pixel Sensors

This chapter is devoted to the description of silicon sensors, focusing on the comparison between hybrid pixel and monolithic pixel devices. The key features of these types of sensor and the typical characterisation studies are mentioned in order to introduce and motivate the principle of laser beam testing. To better support the reasons for laser testing, the interaction of light in silicon is also briefly described.

In crystals, the periodic lattice structure determines the energy bands which can be occupied by atomic electrons. The electrical properties of a material depend on the band gap between the valence and the conduction band. The valence band is the energy band of the bound electrons that belong to the outermost shell. Above the valence band, the conduction band is present, and electrons belonging to this band are free to move along the crystal. Semiconductors have a relatively small band-gap energy: in the case of silicon, it is around 1.12 eV.

The working principle of silicon detectors is that a particle traversing the detector creates electron-hole pairs by ionisation. The average energy needed to produce an electron-hole pair in silicon is 3.6 eV. If this process occurs in a region that is free from charge carriers, recombination cannot take place, and if an external electric field is applied, the released charges drift towards the electrodes. While drifting, a signal is induced on the electrodes. The signal related to the released charge is processed by the readout electronics, the main component of which is a charge-sensitive preamplifier.

The basic element of most silicon detector is the p-n junction, which is the interface between a p-type silicon (doped with an element of the III group, e.g. B) and an n-type silicon (doped with an element of the V group, e.g. P). In n-doped silicon, there are extra negative charge carriers, whereas in p-type silicon there is a surplus of positive charge carriers. The diffusion of charge carriers in the adjacent semiconductor takes place to restore the thermal equilibrium. As the charge carriers diffuse, the electric field resulting from the presence of the ionised dopant atoms increases. When the thermal equilibrium is reached, at the interface there is a region where only the space charge is left and where there is a potential difference, called the built-in potential.

This region, called the depletion zone, can be enlarged if the junction is reverse biased, meaning that an external potential difference, called bias voltage, is applied with the cathode to the p-type silicon and the anode to the n-type silicon.

Silicon detectors are used for different purposes: one of the most important applications is tracking in experiments at colliders.

Before 1984, silicon strip detectors were mainly used as inner tracking detectors in collision experiments. In these kind of detectors, the collection electrodes are typically p+ strips implanted on a n-type substrate. The development of new silicon sensors, such as microstrip detectors, was mainly driven by the goal of achieving higher spatial resolution by decreasing the strip pitch, in order to en-

hance track resolution in multiple track events, such as jets. This was particularly needed in heavy-ion collision experiments, where the density of tracks per collision is very large.

In 1984, the realisation of a pixel detector was suggested for the first time. After a long R&D phase on both the hardware and readout techniques, pixel detectors were introduced in experiments, especially in the innermost layer of the trackers. In addition to an improved spatial resolution due to the higher segmentation, pixel detectors feature also a higher signal-to-noise ratio as a consequence of the small pixel area, which implies a small capacitance.

The inner tracking and vertexing systems of the four experiments at the LHC implement silicon sensors in pixel, microstrip, or strip configurations [17].

2.1 Hybrid pixel sensors

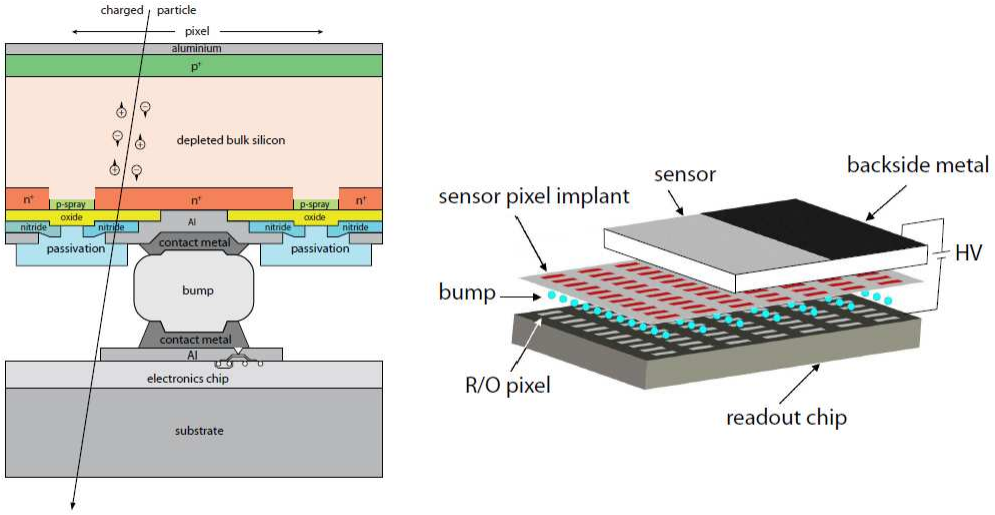

(a) Hybrid pixel (b) Pixel matrix

Figure 2.1: Hybrid pixel silicon detector: pixel unit and full matrix scheme [6]

In hybrid sensors, the pixel unit is made up of two separate parts: the sensor and the readout chip, which are electrically connected together through the flip chip bump bonding technique.

The sensor is realised starting from a silicon wafer which can be n or p, which is called bulk. Pixel electrodes are then implanted in the substrate. Guard rings are used to bring the potential applied to the bias implants to zero at the pixel electrodes. Different configurations are possible by implementing the planar process. This technique is a well-established industrial semiconductor manufacturing process based on photolithography and ion implantation. A scheme of the pixel cell and the full sensor matrix can be seen in Fig.2.1.

On an n-type bulk, a segmented n+ implant is obtained on one side in order to get the collecting diodes; therefore resulting in sensors based on the collection of electrons. On the backside, a large p+ implant is needed to apply the bias. It is surrounded by guard rings to have a gradual potential drop to zero at the edge. This configuration requires two-sided processing, and at first it was adopted for the pixel layers of the trackers of all LHC experiments.

As the radiation fluence increases, the process of type inversion can occur, since the presence of radiation-induced extra charge carriers affects the conductivity of the n-substrate, even converting it into a p-type. This is more relevant in an n-type substrate, where electrons are the majority carriers, because of the higher mobility of electrons with respect to holes. This can lead to an increase of the bias voltage needed to have a fully depleted sensor. For this reason, studies on hybrid pixel sensors for LHC upgrades have focused on this aspect, and a better solution has been achieved by

implementing n+ pixel implants on a thin and high resistivity p-substrate. This configuration requires only single-sided processing, which is cost saving; however, for this reason a lot of effort has been put in developing efficient and safe guard-ring structures on the electrode side that are very close to the readout electronics. This solution is cheaper and results in sensors that are reasonably thin and operate at lower bias voltages.

This is the main type of hybrid planar pixel sensor that has been used for the upgrades of the LHC experiments.

The current R&D activties on hybrid pixel technology are also focused on 3D silicon technology, which has been chosen, for example, for the inner layer of the ATLAS tracker: with the implementation of a non-standard technology, electrodes are vertically implanted in the substrate. In this way, the charge collection is full and fast, due to the shorter drift path, at very low bias voltages, and the radiation tolerance is strongly improved because of the reduced probability of trapping; however, this approach is much more costly and an implementation on large area is difficult due to the complex fabrication process. In parallel, studies are also being conducted on wafer thinning and 3D integration [6].

Hybrid pixel detectors are consolidate devices with very good modularity, customisation features, and radiation tolerance properties. However, hybrid pixel detectors have some drawbacks that can be overcome by choosing the monolithic pixel structure, which will be described in the next section.

As already highlighted, hybrid pixel sensors require expensive and laborious techniques, especially because of the bump-bonding and flip-chipping processes. Furthermore, as a consequence of the need for one-to-one vertical bump connections for all pixel cell, support, and cooling structures of the pixels, the material budget is relatively large, more than $1.5\%X_0$ per layer, and the spatial resolution is of the order of 10 μm [6, 20].

2.2 Monolithic Active Pixel Sensors

In monolithic pixel cells, hybridisation technology is not necessary because the sensing region and the readout electronics are built on the same silicon substrate. The basic structure of MAPS consists of an epitaxial layer, grown on top of a substrate and hosting the CMOS front-end and readout electronics. This configuration implies a very localised depletion region surrounding the collection electrode; therefore, the charge collection is incomplete and slow due to the fact that it is dominated by diffusion rather than drift.

NMOS electronics are placed inside a pwell whereas the nwell which hosts PMOS electronics is shielded from the epitaxial layer by a deep pwell to ensure that charges are collected only by the nwell collection diode.

As an example, the ALPIDE chip, implemented in the ITS2 as already mentioned in 1.2.2, consists of a high-resistivity p-type epitaxial layer grown on a p-type substrate. It has a full thickness of 50 μm; the epitaxial layer is around 25 μm thick, and it can be reversely biased. As already mentioned and highlighted in Fig.2.2, charge collection by drift takes place only in a small depletion region around the collection electrode.

Being characterised by a relatively slow charge collection and a moderate radiation tolerance, conventional CMOS MAPS have been adopted only in the inner trackers of heavy ion collision experiments, such as ALICE and STAR, which operate at a lower radiation fluence and rate with respect to the pp collision experiments like CMS and ATLAS.

In order to enhance the charge collection speed and radiation resistance to meet the requirements of future pixel trackers at the LHC, it is necessary to increase the depletion region depth by modifying the standard CMOS technology. At the same time, to get a low analog power consumption and high signal-to-noise ratio, the key requirement is to keep the pixel capacitance as small as possible.

To do so, several ongoing studies focus on different CMOS processes possible modifications. Two main paths can be pursued to develop Depleted MAPS (DMAPS): using a substrate with mid-to-high

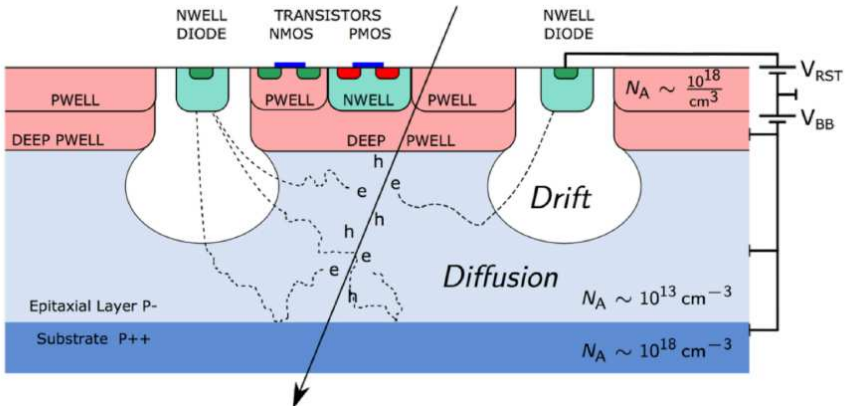

Figure 2.2: MAPS implemented in ALICE ITS2 [4]

resistivity, or adopting specific High Voltage (HV) technologies to manage larger bias voltages.

In the HV case all the electronics is hosted inside a deep n well, which acts as collection electrode. This solution provides good charge collection thanks to the large fill factor, and an improved radiation tolerance; however, it implies an intrinsic large capacitance, thus a larger power consumption and noise.

The high-resistivity substrate approach uses a small implant as collection electrode, outside the well hosting the electronics as collection electrode, as in the ALPIDE design. An extra deep low-dose n-implant is added beneath the electronics, leading to the formation of a planar junction at the interface between the implant and the epitaxial layer. In this way, it is possible to deplete the full epitaxial depth with a relatively low bias.

This configuration has the drawback of having a non-uniform electric field along the pixel length due to the fact that the collection electrode is very small, in particular it drops to zero at the corners. To compensate for this effect by increasing the electric field on the sides, two modified geometries have been suggested, as can be seen in Fig.2.3.

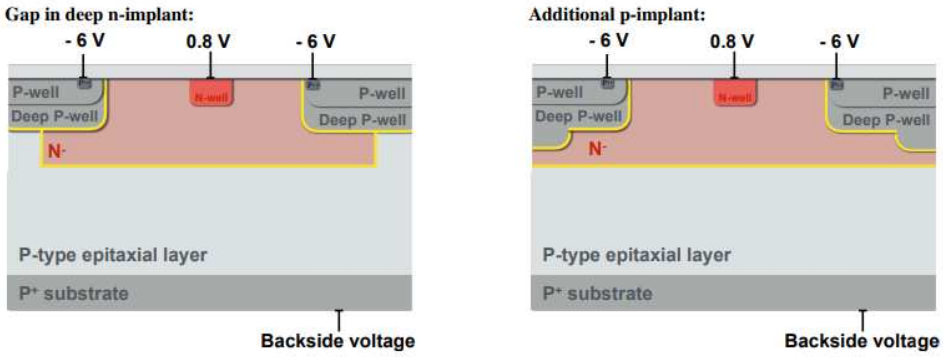

Figure 2.3: Modified CMOS MAPS for full depletion of epitaxial layer: on the left, gap in deep n-implant and, on the right, additional p-implant configuration [9]

This designs family has the key advantage of keeping the collection electrode small and, therefore, presents a very low detector capacitance (on the fF order), leading to a high signal-to-noise ratio, low analogue power consumption, and increased charge collection speed and radiation tolerance [9]. However, this approach works effectively for depletion thicknesses smaller than 100 µm, after which the bias voltage necessary to further increase the depletion layer negatively affect the electronics. To develop MAPS with thicker active substrate, of the order of 300 µm and more, a specific process has been designed and produced in the context of the INFN SEED and ARCADIA collaboration, based on 110-nm CMOS technology by LFoundry.

The structure of the SEED/ARCADIA design is shown in Fig.2.4. The substrate is high-resistivity n-type, and on the bottom surface a p+ implant surrounded by a guard-ring structure forms a pn junction where to apply the bias voltage. In this way the depletion region forms starting from the backside, with the HV bias applied to the backside implant, so keeping a low voltage on the electronics side.

On the top surface a low-resistivity n-type epitaxial layer is grown on top of the n-substrate, and deep pwells enclose the PMOS nwells; this arrangements allows a better control of the punch-trough current, and to maintain the bias on the sensing electrodes lower than 1 V, as required by the 1.2 V constraint of the 110 nm technology node. In this way, negative backside HV bias of the order of $|V|$ = 100−150 V can be applied to reach the full depletion of the substrate [13].

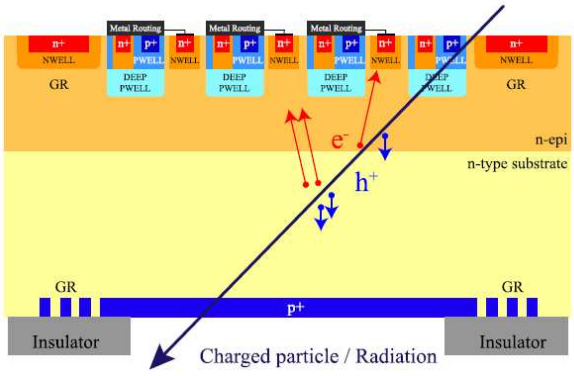

Figure 2.4: Modified CMOS MAPS for full depletion of thick active substrate [13]

2.3 MAPS characterisation

A standard procedure for the characterisation of new devices is to perform test beam at accelerator facilities. Depending on the facility, beams of different charged particles can be chosen, such as protons, electrons, muons or pions. Typically, the beam energy is such that particles interact as a Minimum Ionizing Particle (MIP), thus providing the smallest signal that can be released in a detector. In silicon, as a rule of thumb, a MIP releases around 80 e^-/h^+ pairs/μm[1] [13].

Typically, the Device Under Test (DUT) is placed inside a beam telescope structure for particle tracking. A telescope is made of several layers of silicon detectors used to generate a reference signal. In fact, exploiting a telescope structure, the particle tracks can be reconstructed before and after traversing the DUT. In test beams, many studies can be done: for instance, the sensor can be characterised in terms of detection efficiency, spatial resolution, and fake hit rate.

Test beams provide effective and complete characterisation of the sensor performance; however, they are time consuming and expensive. It is therefore desirable to have the possibility to execute characterisation studies using quicker and more affordable techniques, especially when the necessity to test many different flavours and versions arises during the sensor R&D phase, which would lead to an unmanageable and expensive testing campaign if only performed through test beams.

While energy response and calibration can be done using radioactive sources, pulsed laser beams can be utilised to precisely characterise the charge collection performance in terms of linearity, geometrical uniformity, and time dependence. In fact, a laser beam can be focused in order to hit the sensor in a specific position with micro-metric precision and, using controlled motion stages, it is possible to move the laser spot choosing a specific direction along the pixel matrix.

Performing studies in terms of absolute response of the sensor is complicated. Laser pulses are not so stable in terms of power, and show fluctuations and thermal drifts. In addition, photons can undergo several optical processes when entering the sensor, depending on the properties of the medium, which

[1] In the following, this value is referred to in terms of 80 e^-/μm because the devices used collect only electrons.

are difficult to predict. However, having a good knowledge of the behaviour of the laser source and by continuously monitoring it through a reference signal, it is possible to perform such studies in terms of relative response, as it will be further explained in Sec.3.1.

As photon interaction in silicon, especially at low energy, is different from charged particle interaction, in the following subsection a description of the interaction process is presented.

2.3.1 Interaction of low energy photons in silicon

Silicon sensors can detect electromagnetic (EM) radiation from the infrared (IR) range up to the X-ray range. Photon interaction in matter occurs through three different processes: photoelectric effect, Compton scattering, and pair production.

In the energy range $E \lesssim 100$ keV, the photoelectric effect is the dominant process; therefore, the basic principle for low-energy photon detection in silicon sensors is photoelectric absorption.

A photon is absorbed, causing the transition of an electron from a lower energy level to a higher one. In the simplest case, if E_1 and E_2 are two energy levels with $E_2 > E_1$, to have an electron transition between the two levels, the incident photon should have an energy at least equal to $h\nu = E_2 - E_1$. As a result, if the transition is interband, the electron is promoted to the conduction band and the initial energy state is left unoccupied, implying the creation of a hole in the valence band. Therefore, the interband absorption is equivalent to electron-hole pair creation, which is the basic process that is exploited in silicon sensors. However, this description of the process is very simplified. In semiconductors, the band structure plays a fundamental role, and the electronic states near the band extrema are those involved in optical processes. Before focusing on optical processes, it is useful to take a step back.

The key feature of semiconductors is that the valence and conduction band are separated by an energy gap E_g, greater than the energy gap of conducting materials and smaller than the one of insulating materials. Usually, the band structure is described in the E-k diagram, where $\hbar\vec{k}$ is the crystal momentum with the k-vector $\vec{k}$ being the wave vector of the electron in the crystal, which is involved in the electronic wave function that is the solution of the one particle Schrödinger equation.

The band gap of semiconductors can be direct or indirect. In direct-gap semiconductors, the extrema of the valence and conduction band occur at the same $\vec{k}$. However, in indirect gap semiconductors, such as Si and Ge, the conduction band minima and the valence band maxima are located at different values of $\vec{k}$. Band edge absorption process is therefore very different in direct and indirect gap semiconductors.

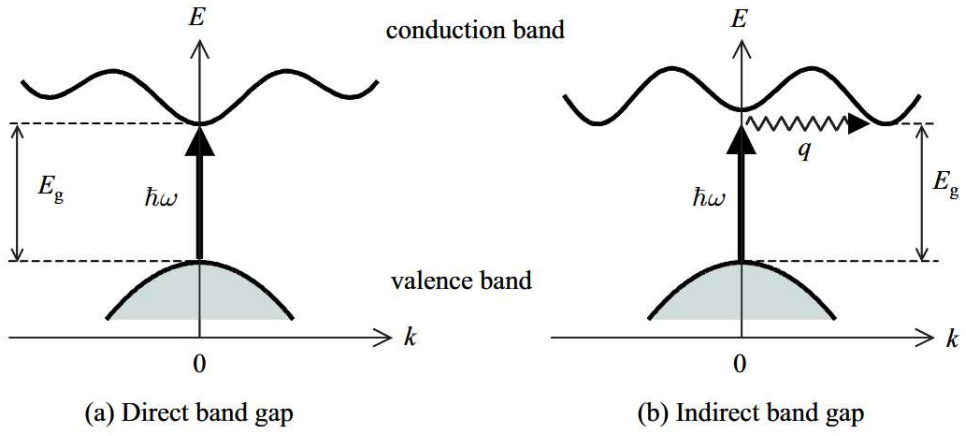

Figure 2.5: Photon absorption in direct band gap and indirect band gap semiconductor [8]

In fact, a large change in the wave vector of the electron must occur in indirect gap semiconductors as can be clearly seen in Fig.2.5.

The wave vector of photons is too small compared to the order of magnitude of the electron wave vector. The electron wave vector is of the order of the Brillouin zone size π/a with the unit cell size a of the order of 10^{-10} m, while the photon wave vector is $2\pi/\lambda$ with λ of the order of 100-1000 nm.

As a consequence, a phonon must be involved in order to satisfy momentum conservation. This makes this process a second-order process where a photon is destroyed, and a phonon is either created or destroyed. For this reason, indirect absorption has a transition rate that is much smaller than in the direct case. In indirect absorption, the energy conservation implies that[2]:

$$E_f - E_i = \hbar\omega \pm \hbar\omega_{phonon} \implies \hbar\omega = E_g \mp \hbar\omega_{phonon} \tag{2.1}$$

The threshold of the process is slightly different from the energy band gap E_g due to the fact that a phonon is taking part of the process. [8]

Assuming the gap energy to be in first approximation the threshold of the process, one can get the minimum photon energy necessary for a photon to generate a signal in a silicon detector. At room temperature (T = 300 K), silicon has a band gap energy E $\sim$ 1.12 eV thus $E = hc/\lambda \gtrsim 1.12$ eV $\implies$ $\lambda < 1107$ nm.

If an incident photon flux of intensity I_0 is incident on silicon, the flux will be absorbed while traversing the medium, as described by the following equation:

$$I(x) = I_0 \cdot e^{-\alpha x} = I_0 \cdot e^{-\frac{x}{\mu}} \tag{2.2}$$

where α is called the absorption coefficient and μ is the characteristic absorption thickness. The absorption coefficient depends on the incident photon energy and the temperature. In particular, it increases with photon energy and with temperature.

At room temperature, the graph in Fig.2.6 shows the absorption of photons in silicon for three different values of wavelength where it is clearly visible that at larger wavelengths the photon flux is less attenuated. The experimental values of the attenuation coefficient used in the plot are taken from [7].

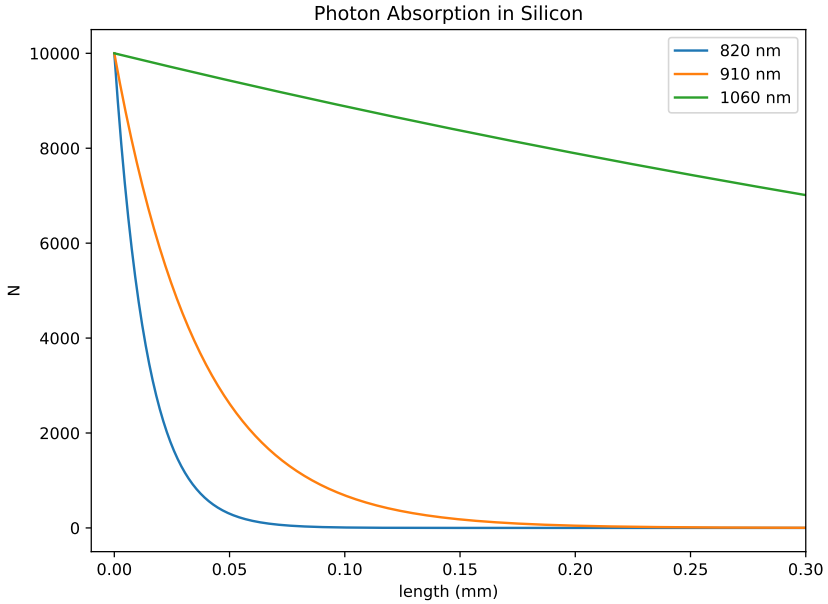

Figure 2.6: Number of photons as a function of depth in silicon at different wavelengths

[2]The sign $\mp$ depends on whether the phonon gets emitted or absorbed.

Chapter 3

Experimental Setup

In this chapter, the experimental setup is described, starting with a general overview of the layout and then going into detail of the optical setup, the power measurement system, and mechanical structure.

3.1 Description of the setup

A brief description of the setup is given, while more details and technical specifications of the different components will be given in the following subsections.

The experimental setup consists in several parts, as shown in Fig.3.1.

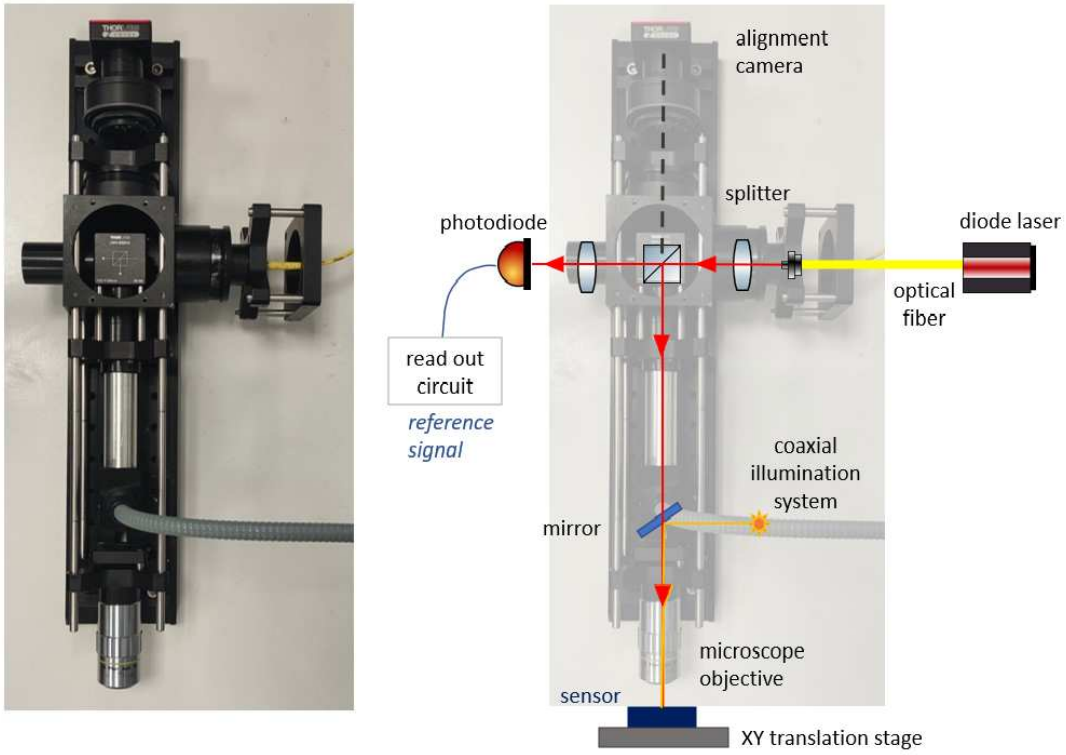

Figure 3.1: Experimental setup with the main components highlighted

The working principle is the following: a pulsed laser beam, produced by a diode laser source (1), exits from an optical fibre (2). After a lens, used to refocus the beam, the laser beam is split down to two optical paths using a non-polarising beam splitter cube (3). The splitting is done in order to simultaneously measure the response of the device under test and the corresponding signal from a reference detector.

The first optical path, followed by the transmitted beam, is used to generate the reference signal in a photodiode (4), onto which the beam is focused using another lens after the beam splitter, allowing to continuously monitor the lasing power. The part of the laser beam that is reflected by the beam splitter along the second optical path is instead focused onto the sensor under study using a microscope objective lens (6). The sensor can be moved using an xy micrometric motion stage. The optical path reaching the sensor also hosts a coaxial illumination system (5) used to illuminate the sensor under test during the positioning and alignment phase with the laser spot.

3.1.1 Optical setup

For the optical part, the following components and instrumentation have been implemented:

- Diode laser: λ = 910, 1060 nm and DC power supply up to 50.3 V;
- Single Mode optical fibres:
  - Thorlabs 780HP with operating wavelength range: 780–970 nm
  - Thorlabs 1060XP with operating wavelength range: 980–1600 nm
- Optical lenses, adjustable lever iris, diaphragm;
- Beamsplitter: Thorlabs CM1-BS014 30 mm Cage Cube-Mounted Non-Polarizing Beamsplitter with operating wavelength range: 700–1100 nm;
- Coaxial system: Microscope halogen illuminator with adjustable brightness and intensity coupled to optical fibre bundle and half-mirror;
- Objective: 20X Mitutoyo Plan Apo Infinity Corrected Long WD Objective with NA = 0.42, effective focal length = 10 mm and working distance = 20 mm;
- Camera: CS165CU/M-Zelux® 1.6MP Color CMOS Camera with objective 3.5/50.

The optical setup with the main component is the one shown in the scheme above, see Fig.3.1.

One of the key issues of the setup is laser attenuation. During tests and measurements, both the optical fibre and the diaphragm can be tuned, or the position of the first lens can be shifted, in order to modify the attenuation factor of the laser beam on the device under test. The ideal situation is having a small signal on the pixel detector, so to avoid saturation, and a larger signal on the monitoring photodiode, which can handle a much larger number of photons before saturation.

It turns out there is not a need to perform a very accurate optimisation of the optical setup. On the one hand, the output power of the laser source is of O(100 nW) per pulse, that certainly corresponds to a much larger number of photons on the sensor surface than is needed, but it is far from saturation levels; for λ = 910 nm, the wavelength that has been mostly used in these measurements, a pixel of MATISSE saturates with an equivalent number of incident photons of about 30000, that corresponds to a power per pulse of O(μW). On the other hand, the photodiode, with the readout chain described in 3.1.2 can deal with pulse power up to O(10 mW).

3.1.2 Photodiode and charge amplifier

To effectively monitor the number of photons coming from the very short and small laser pulses, it is necessary to develop a system based on a photodiode coupled with a charge-sensitive readout, e.g. a charge-to-voltage converter, where the amplitude of the output signal is related to the charge released in the photodiode. The goal is to develop a system with the capability of detecting a released charge equivalent to a MIP in silicon. A MIP is characterised by an energy loss of about 80 $e^-/\mu m$, so for a diode depleted region of 150 μm, a MIP releases a charge of about 12000 electrons or, equivalently, 1.92 fC.

The main components of the setup are the following:

- Hamamatsu Si PIN Photodiode S3590–01 with 10×10 mm^2 active area, operating range 340–1060 nm, max reverse bias 50 V, see Fig.3.2a;
- Charge-preamplifier thin-film hybrid circuit developed for high energy physics experiments. It has four low noise JFETs in input, a feedback $R_f = 100$ MΩ and $C_f = 3$ pF;
- Operational amplifiers: AD847JN, AD846AN;
- Tektronix MSO4104 Mixed Signal Oscilloscope;
- DC power supply:
  - Photodiode reverse bias: Keithley 2200–72–1 Programmable DC Power Supply: 72V, 1.2A;
  - R/O circuit power supply: AGILENT E3631A Triple Output DC Power Supply: +6V, ±25V;

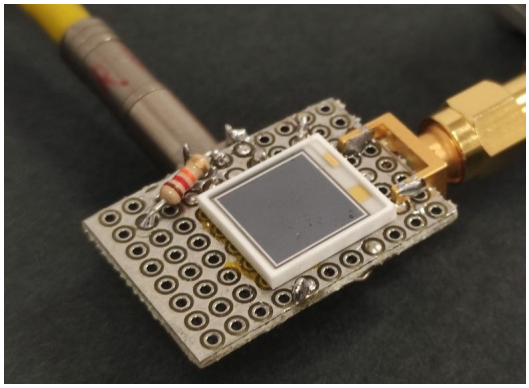

(a) Photodiode with polarisation circuit

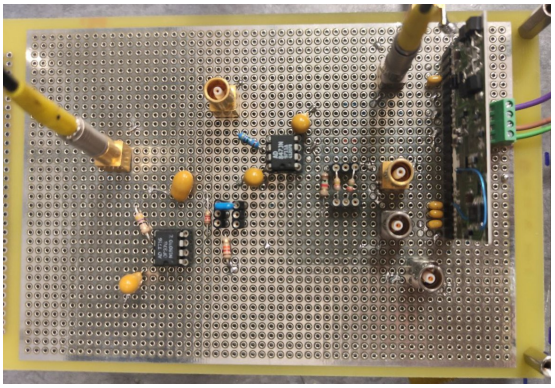

(b) Readout circuit

Figure 3.2: Pulsed laser power measurement setup

Photodiode characterisation

Using a probe station and a LCR meter HP 4284A, it is possible to perform a measurement of the capacitance of the diode and estimate the height of the depletion region. The LCR meter performs measurement of the capacitance when a sinusoidal voltage is applied to the device. The sine waveform has a fixed frequency of 10 kHz. A DC bias reverse voltage is applied, and varied from 0 to 45 V in steps of 1 V.

The measured capacitance of the diode changes with the reverse bias, as the thickness of the depletion layer changes. Fig.3.3 (a) shows the measured capacitance as a function of the voltage, whereas the depletion width curve is shown in Fig.3.3 (b). To a first approximation, the photodiode can be assumed to be a parallel plates capacitor, and therefore the capacitance C can be expressed as

$$C = \frac{\epsilon_0 \epsilon_r A}{w}$$

where $\epsilon_r = 11.7$ is the relative dielectric constant of silicon, A = 100 mm^2 is the area of the photodiode, and w is the depletion layer width. At full depletion the capacitance no longer changes with further increases of bias voltage. The measured capacitance at full depletion is ∼ 74pF and the depletion width is ∼ 140 µm.

To polarise the diode with a reverse bias, a circuit was built on a small breadboard, shown in Fig.3.2b. The bias voltage is applied using a LEMO cable; the output signal comes out on a SMA cable going to the readout chain. The bias voltage was set to $V_b = 45$ V to ensure full depletion of the photodetector, the optimal condition, as it maximises the width of the active volume, maximising the collected charge signal while minimising noise.

The schematic of the circuit can be seen in Fig.3.4

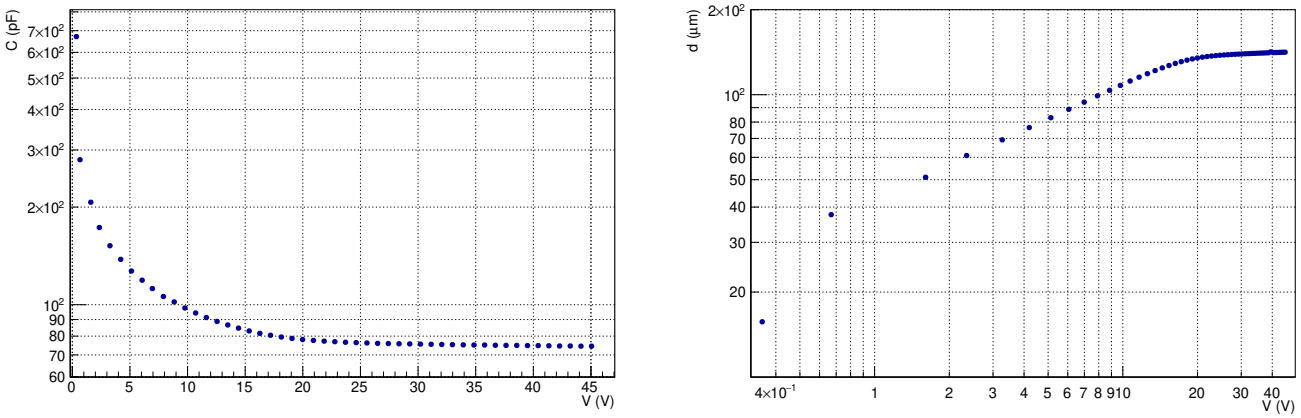

(a) Capacitance as a function of the bias voltage. The working voltage was set at 45 V for full depletion.

(b) Depletion depth as a function of the bias voltage

Figure 3.3: Photodiode characterisation with LCR meter and probe station

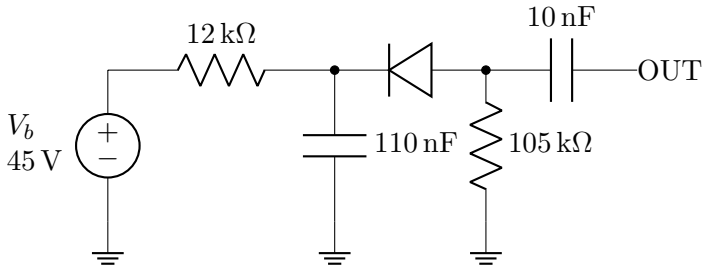

Figure 3.4: Schematic of the polarisation circuit of the diode

Charge amplifier

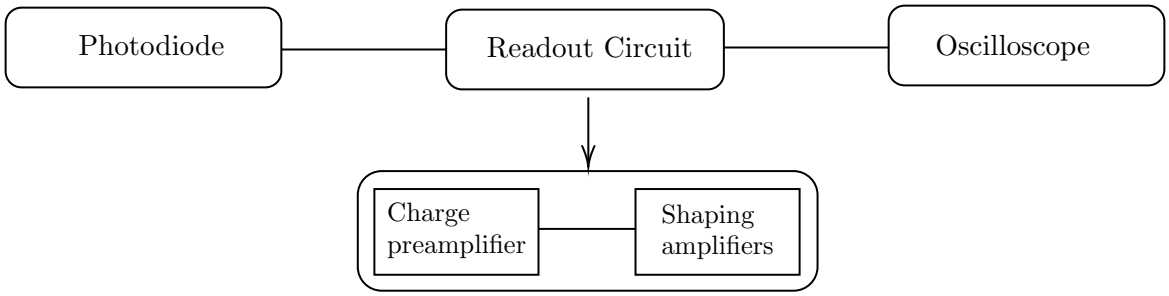

The goal is to have a readout chain with a sufficiently wide dynamic range and a large amplification gain especially for very low charges. For this reason, after the charge preamplifier, two stages have been added by cascading two operational amplifiers. The first provides a zero-pole suppression and a CR filter that differentiates the signal. The second one acts a second gain amplification, in a non-inverting configuration.

In Fig.3.5, the readout chain scheme is shown. The terminal labelled as OUT is the output of the first stage, whereas the terminal OUT2 is the one related to the second stage.

To test the response of the readout chain, a test capacitor of 1pF has been added in series with one of the input terminals of the charge integrator so that, using a pulse generator to generate a short square pulse, a known amount of charge can be injected. In this way, the response of the two stages was characterised, and the conversion factor from input charge to output voltage signal has been derived performing a linear fit of the output voltage as a function of the input charge.

The input charge depends on the input voltage step as $Q = C_{inj} \cdot V_{set,pulse}$. The amplitude of the output signal is measured using the cursors on the oscilloscope. The uncertainty associated to the

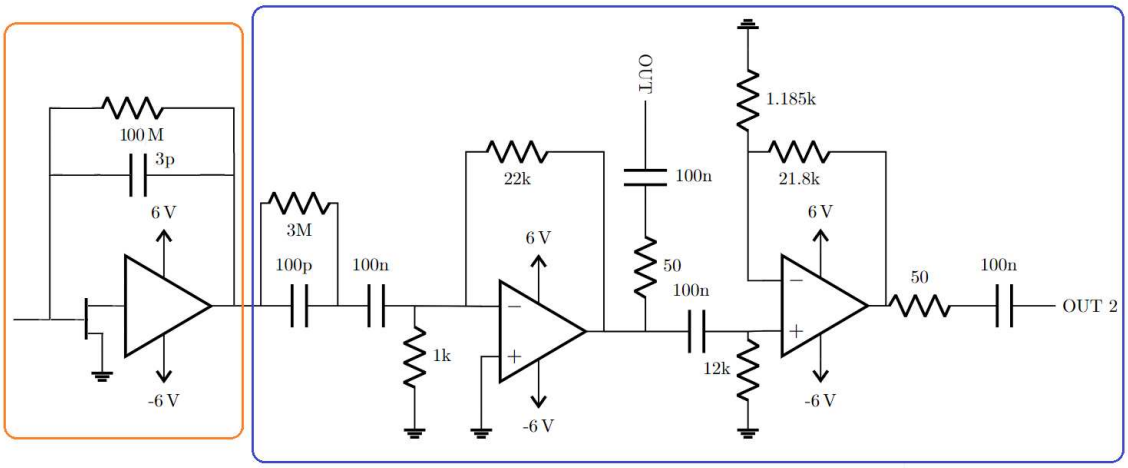

Figure 3.5: Schematic of the readout chain. In orange, the simplified schematic of the low noise JFET-input charge preamplifier (the schematic of the charge preamplifier hybrid circuit is much more complex), in blue the two shaping stages.

measurement is computed considering the different terms; e.g. DC gain accuracy, scale uncertainty and offset, as given in the DC voltage measurement accuracy section of the user manual of the oscilloscope.[1] In Fig.3.6, the response of the first amplification stage is shown.

The behaviour shows a very good linearity from 2 fC up to injected charges of the order of 450 fC with a moderate gain. In fact, the relation, obtained fitting the point in the range [0, 450] fC, is given by:

$$V_{out}[mV] = 0.6\,mV + 2.862\,mV/fC \cdot Q[fC] \tag{3.1}$$

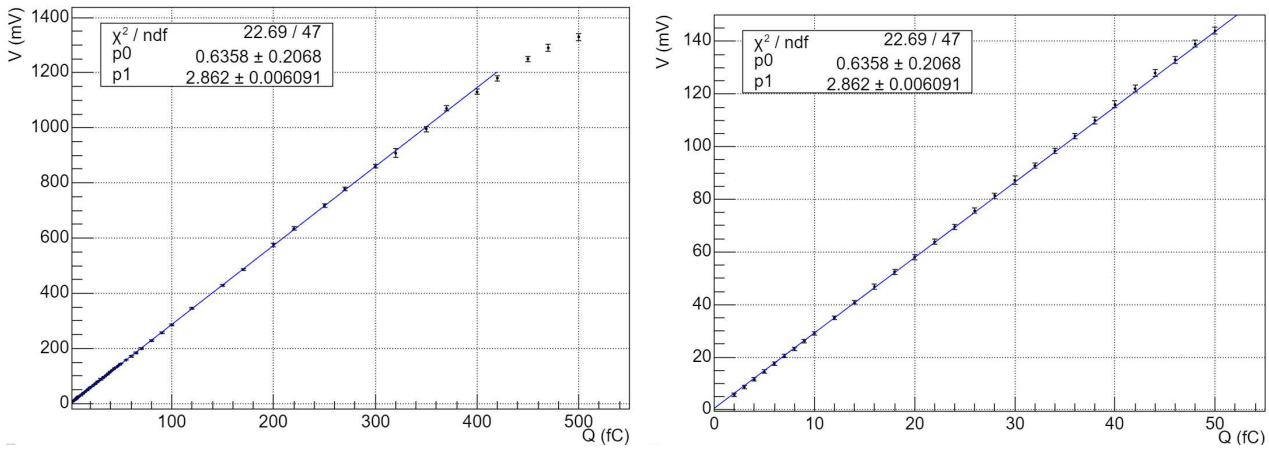

(a) Output voltage vs input charge

(b) Zoom in the range up to 50 fC

Figure 3.6: Calibration of the first amplification stage

In Fig.3.7, the response of the last amplification stage is shown. The behaviour shows a good linearity from 1 fC up to 20 fC. The gain is much larger: in fact it was set to add a non inverting amplifier with a gain ~ 20. It has to be mentioned that, for this stage, it is optimal to use the 1 MΩ internal termination on the oscilloscope, instead of the usual 50 Ω, because the operational amplifier cannot drive much current, thus resulting in an additional factor of gain.

In this case, the conversion relation, obtained fitting the points in the range [0, 20] fC, is given by:

$$V_{out}[mV] = 27\,mV + 94.3\,mV/fC \cdot Q[fC] \tag{3.2}$$

[1] See user manual at `https://download.tek.com/manual/071212104web.pdf`

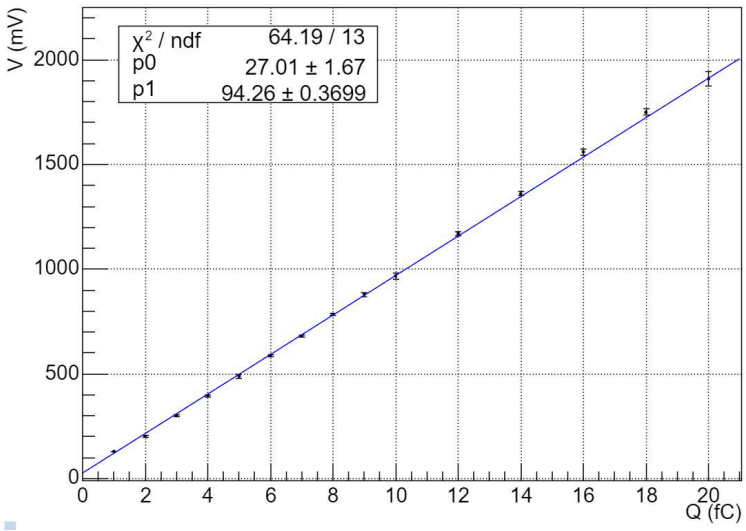

Figure 3.7: Calibration fit of the last amplification stage

Examples of waveforms corresponding to two different single laser pulses, in the same laser settings (λ = 910 nm and V = 50.3 V), at the output of the two amplification stages are shown in Fig.3.8. Both the photodiode and the readout electronics have been shielded by placing everything inside metallic boxes, as they are strongly sensitive to interference and external perturbations. However, during data acquisition, there are still occasional oscillations superimposed on the baseline, more or less evident (see Fig.3.8).

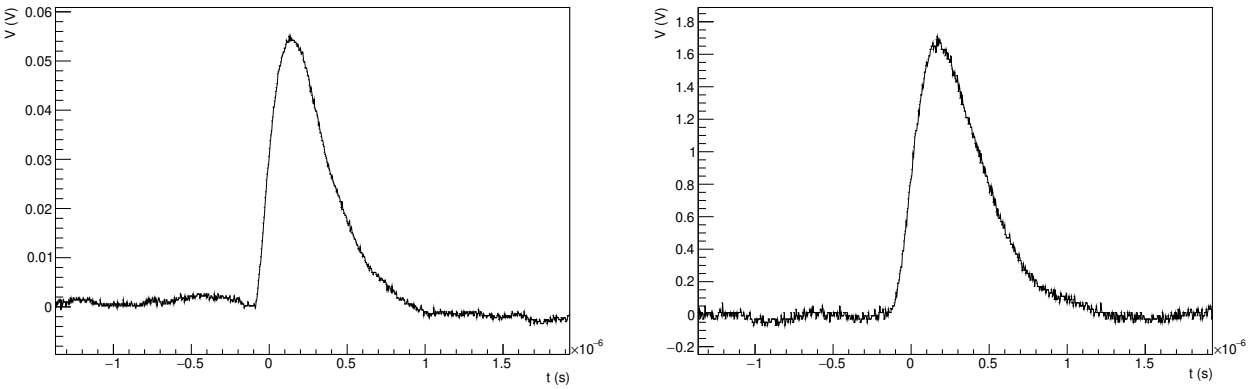

(a) Output stage 1, Q ∼ 18 fC (b) Output stage 2, Q ∼ 18 fC

Figure 3.8: Single pulse waveforms, one from each amplification stage. Noise oscillations around the baseline are evident.

It can be seen that they have a semi-gaussian shape, with similar shaping times of the order of 150µs. The shaping capability could be further improved; however, this is not strictly needed since the readout performance is good enough for the purpose of the setup. In particular, the shaping time has a strong impact both on the output pulse amplitude and the noise, which can be minimised by optimising the shaping time.

The standard parameter that quantifies the electronic noise at the output of the shaper is the Equivalent Noise Charge (ENC), which is usually expressed in terms of input charge or number of electrons. The ENC is the amount of injected charge which corresponds to an unitary signal-to-noise ratio, i.e. it is the charge that produces an input signal equal to the RMS of the output noise. It can be estimated by computing the RMS value of output waveform data points before the rise of the charge signal induced by the laser pulse.

The waveforms at the output of the second stage were acquired with the oscilloscope. In practice, the Root Mean Square (RMS) was calculated for data points in the [-2, -0.5] µs time interval, well before the rise of the charge signal induced by the laser pulse, for a sample of 500 waveforms. Therefore, the effective time interval from which the RMS noise is computed is equal to 750 µs. The histogram of the values from which the RMS is computed is given in Fig.3.9.

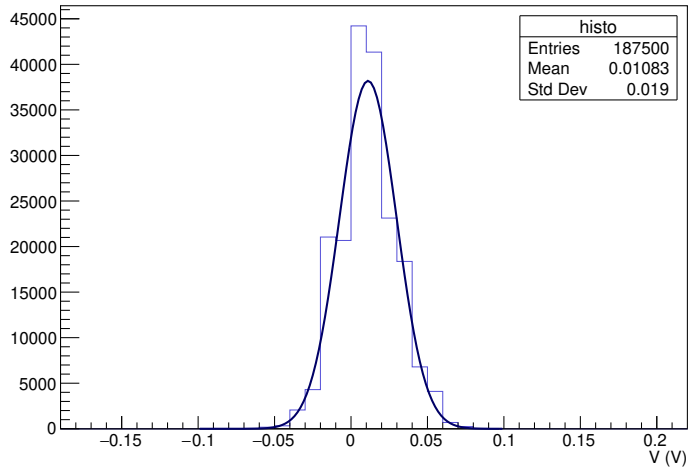

Figure 3.9: Noise distribution obtained considering the points in the [-2.5, -0.5] µs time interval for 500 waveforms

The RMS of the sample of points was computed,and the result is RMS = 21.6 mV. This value, converted into number of electrons using the gain factor, gives an RMS noise, in terms of ECN, of about 1430 electrons.

3.1.3 Mechanical structure

The optical system was mounted vertically in order to keep the device under test in the horizontal plane, the optimal mechanical solution.

An aluminium plate (45.6×8.5 cm^2, thick 2.5 cm) is used to mount all the optics and the mechanical components for holding in place the different elements. The opto-mechanical elements are all by Thorlabs; the cage system (60 mm and 30 mm with assembly rods) is implemented to fix the structure. In order to guarantee stability on the vertical direction, two types of supporting elements have been designed. The 3D model of the full assembly mounted on the supporting platform is shown in Fig.3.10a and the two types of supports are shown in Fig.3.10b: the one on the left is used to fix the CMOS camera, and three supports of the second type are screwed on the platform to hold the structure at three different heights.

The full assembly is then positioned on a microscope-like bearing structure which provides also XYZ manual motion knobs. The position and motion of the device under study is controlled using a XY translation stage: M30XY/M-Kinesis® 30 mm Motorized XY Translation Stage. This translation stage can be remotely controlled via script or via the Kinesis® software provided by Thorlabs. From the technical specifications, it has a ±1.0 µm bidirectional repeatability and 2.5 µm minimum incremental movement.[2]

In Fig.3.11b, the complete setup is shown. On the left of the splitter, the photodiode is placed inside the metallic box and it is held in place using additional cage-system mechanical elements. On the right, the optical fibre is mounted on a specific connector. On top, there is the CMOS camera. In the central part, there is the illumination tube and the microscope objective. Below, one can see the green board, where the chip is located, mounted on top of the xy motorised stage.

[2]The technical datasheet can be found at: `https://www.thorlabs.com/newgrouppage9.cfm?objectgroup_id=14597`

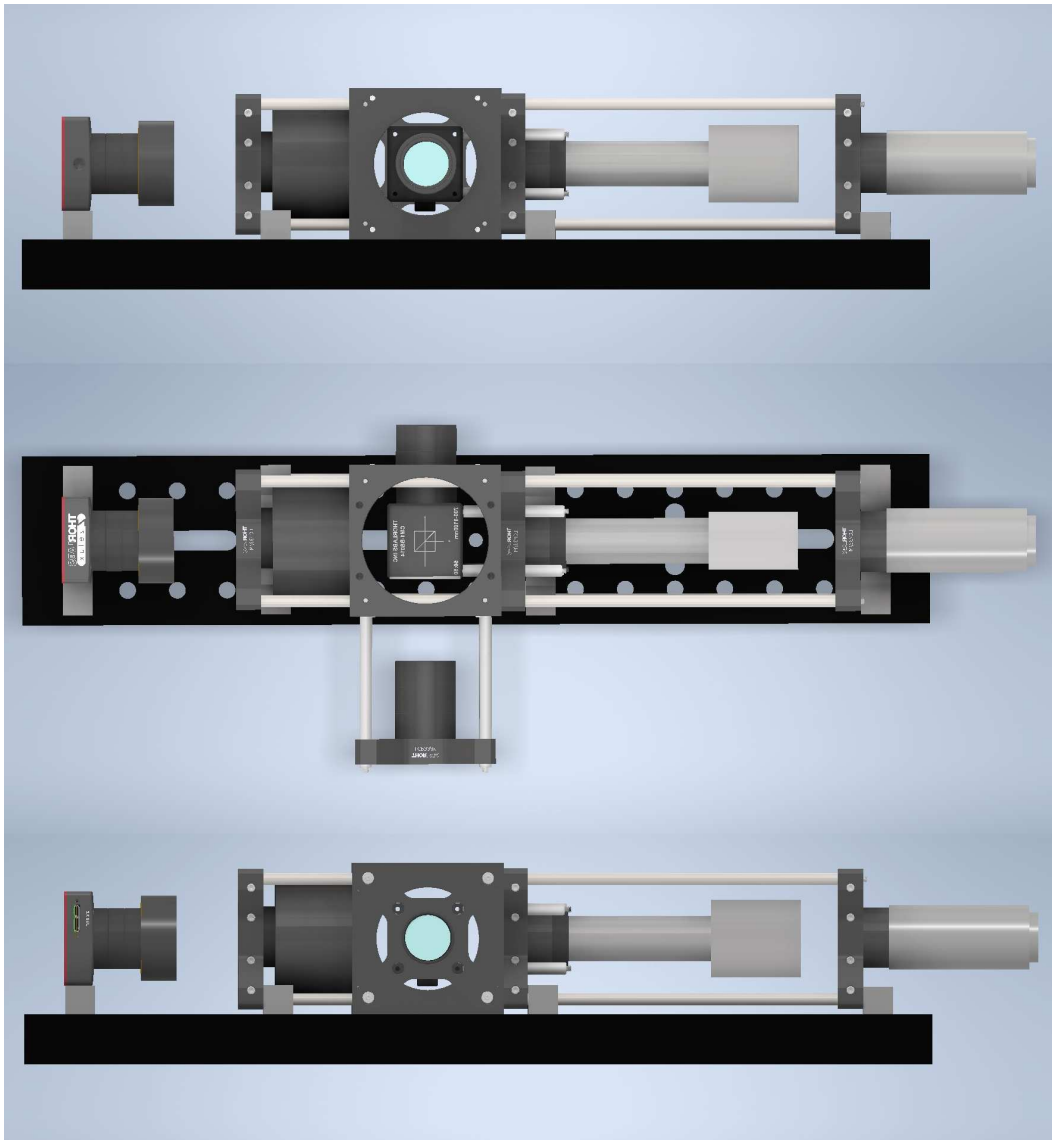

(a) 3D model of the full mechanical design, done with Autodesk® Inventor®

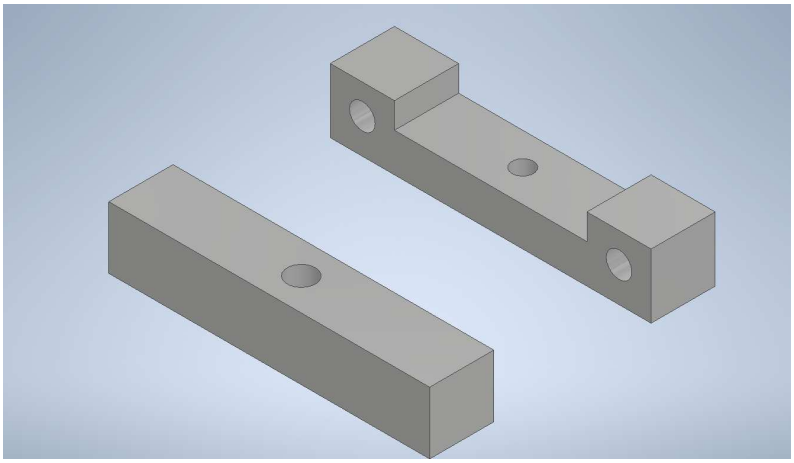

(b) 3D model of the mechanical supports done with Autodesk® Inventor®

Figure 3.10: 3D models of the mechanical assembly

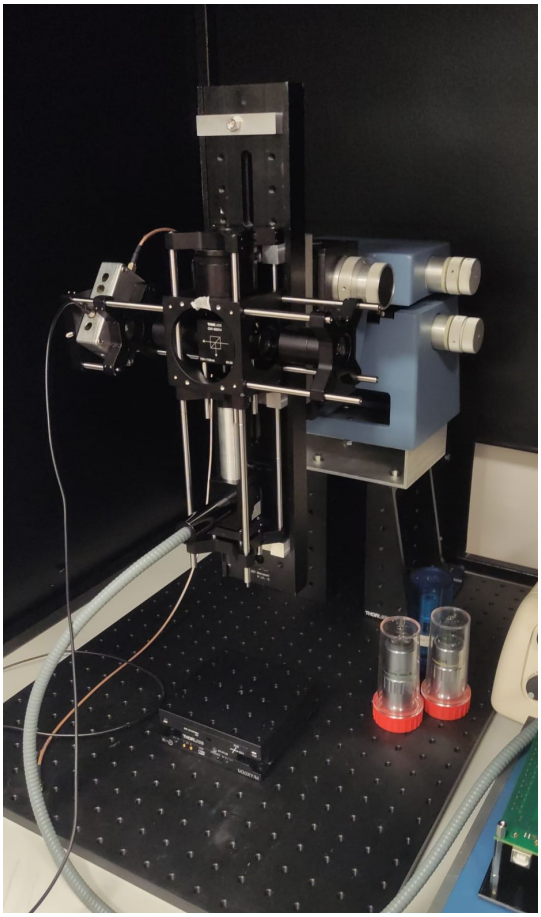

(a) Mechanical assembly with no camera, no optical fibre and no microscope objective. The light blue support is the bearing structure with xyz translation control. On the bottom part, the xy motorised stage is mounted on the optical breadboard.

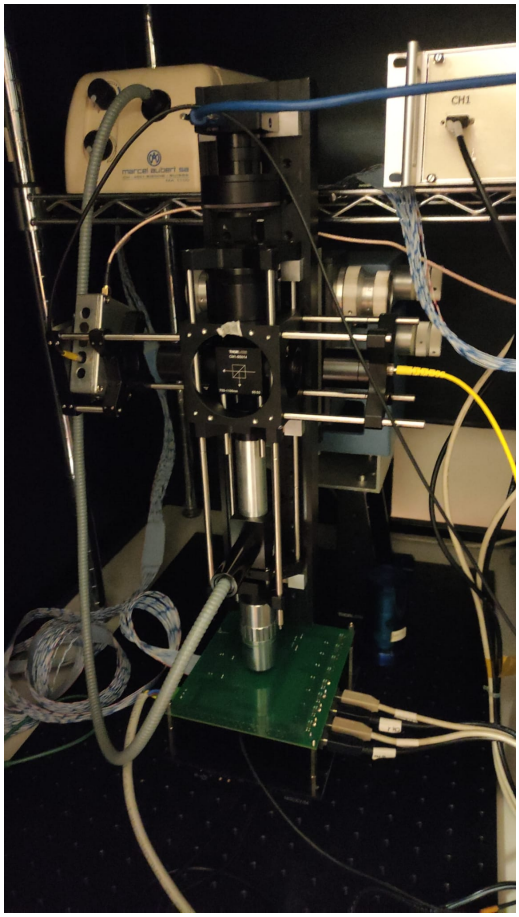

(b) Full assembly: on the right, the yellow optical fibre is visible. On the left, inside the metallic box, there is the photodiode. On the bottom, the microscope objective is visible.

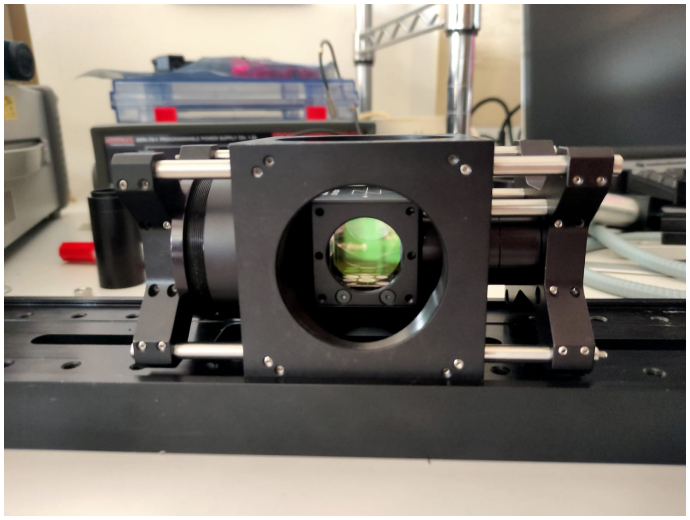

(c) Mechanical assembly to hold beam splitter in place

Figure 3.11: Mechanical assembly of the setup

3.2 Characterisation of the setup

3.2.1 Beam focusing

Given that the typical size of the pixels in silicon pixel detectors is of the order of 25-50 μm and that the goals for future trackers based on MAPS is to have pixels sizes of O(15 $\times$15μm^2), the goal for the laser beam spot is to have a diameter of O(10–20 μm). Regarding the typical material thicknesses that the laser beam has to go through, MAPS with depleted epitaxial layers have an active region of the order of 15-25 μm whereas fully depleted MAPS can be much thicker. Illumination from the frontside has the drawback that typically there are many metal layers deposited leading to a strong reflection of the laser light. Thus, if it is feasible, it would be optimal to illuminate the sensor from the backside, where no metal layers are present. In case of MAPS with depleted epitaxial layers, one must keep in mind that photons have to traverse a layer of undepleted substrate, typically of O(25–35 μm) thick, before getting to the sensitive region. In this case, a careful choice of wavelength is particularly relevant: it is preferable to use a laser beam wavelength with an absorption length not too short in order to reach the depleted region. On the other hand, testing depleted MAPS, like MATISSE, is straight-forward: they can be tested using short IR wavelength.

A preliminary test to characterise the focusing properties of the optical setup was performed. For this purpose, a continuous visible red light laser diode was used as the available infrared laser diodes were all pulsed. The CMOS camera is used to inspect the red beam spot. It is placed on a manual linear XYZ stage, Newport M-562-XYZ, at the end of the optical setup (reflected beam path), mounted on the horizontal direction. The laser diode is powered using a DC power supply; a regulating circuit was built to protect the diode from an accidental over-voltage. The measurements were done with fixed values set on the DC power supply: V=3.5 V and I=21 mA.

By moving the camera along the optical axis (z-direction) it is possible to observe how the laser spot changes. The camera acquisition is performed using the provided software, ThorCam™Software for Scientific and Compact USB Cameras. The images are analysed using the software *Fiji*, an image processing package distribution of ImageJ2 [15]. In particular, the profile plots of the beam spot along the x- and y-direction are obtained and fitted with a gaussian distribution. As an example, in Fig.3.12, two surface plots corresponding to different z-coordinates are presented, where it can be seen that the beam gets narrower. In Fig.3.13, the beam spot can be seen and the horizontal line is the line along which the profile plot is performed. The profile is fitted with a gaussian distribution using ROOT [2].

From the σ of the gaussian fit, the beam waist w, in the approximation of a gaussian beam, can be computed as:

$$w = \frac{1.699}{2} \cdot FWHM = 0.8495 \cdot 2.355\sigma \tag{3.3}$$

The beam waist is taken to be the effective radius of the beam spot, i.e. an estimation of the size of the spot on the transverse plane. In this sense, the beam spot of Fig.3.13 has a radius of (18.7 ± 0.6) μm. Further details on the theory of gaussian beams are given in Appendix.

The position of the focus was determined by varying the position of the camera. In Fig.3.14, the profile along the x- and y-direction are shown for the minimum measured beam spot size. The error bars associated to the abscissa axis are obtained considering the camera pixel size of 3.45 μm and assuming a uniform distribution. The beam spot does not show significant asymmetry. In this minimum waist case, the beam radius, obtained using Eq.3.3, is (8.4 ± 0.3) μm.

From these measurements two considerations on the experimental conditions can be made on the basis of gaussian beam theory. First, the minimum beam waist of a gaussian beam is directly related to the Rayleigh length, the distance from the beam waist where the radius is increased by a factor $\sqrt{2}$; second, the depth of field or Rayleigh range, i.e. the depth of the region in which the beam can be considered as focused, is equal to twice the Rayleigh length. The explanation and formula are given in Appendix, see Eq.A.6. For a wavelength of 650 nm and taking the minimum measured beam waist to be the absolute one, the Rayleigh length is of the order of 300 μm, so the depth of field is 600 μm.

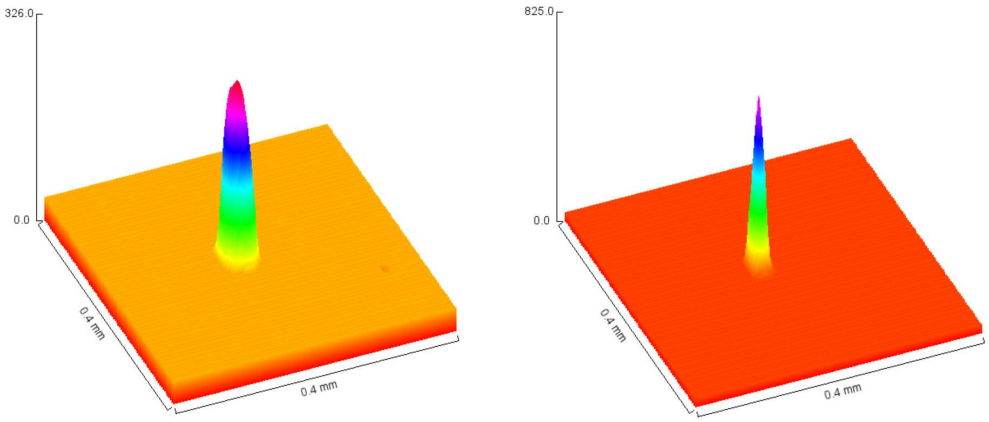

(a) (b)

Figure 3.12: Two surface plots of the laser at two z-coordinate values (surface: 400×400 μm^2)

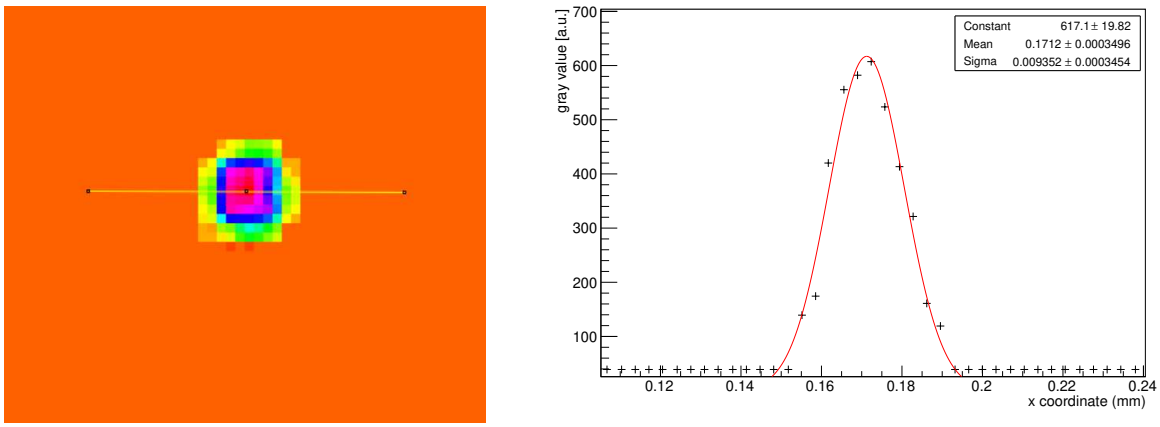

(a) Laser beam spot (b) Profile plot along x-direction fitted with a gaussian

Figure 3.13: Example of analysis of the beam spot size

It must be noticed that the spatial resolution, that is related to the pixel size of the CMOS camera, represents a limiting factor in taking very precise measurements of smaller beam spots and thus, the beam waist value we report could be an overestimate. However, while moving the camera with a precision of the order of 1-10 µm, it never happened that only one pixel was on. From this fact, it can be assumed that the beam diameter is not smaller than about 4 µm (given that the camera pixel size is 3.45 µm). With a minimum beam waist of 2 µm, the minimum field of depth is now 38 µm. We conclude that the beam characteristics at focus are of the order of the goal requirements.

However, these considerations are an approximation, as they assume an ideal gaussian beam. A real gaussian beam is characterised by a quality factor, called M^2, which is equal to 1 for an ideal beam and > 1 for real beams, resulting in a slightly reduced Rayleigh range. In addition, these measurements have been made in air and with a wavelength that belongs to the visible light range. The Rayleigh ranges at wavelengths of 910 nm and 1060 nm are reduced respect to the 650 nm value by factors given by 650 nm/910 nm ~ 0.7 and 650 nm/1060 nm ~ 0.6. The propagation of the laser beam in a silicon device is much more complex since there are many other effects that have to be considered: in particular, refraction, reflection and absorption. Due to refraction, the Rayleigh range gets shrunk by a factor equal to the refractive index of silicon, that is about 3.4 at the IR wavelengths. Part of the beam can also be reflected as a result of the change in the refractive index. Moreover, due to absorption, as the intensity of the laser beam goes down, the beam becomes broader with an increase of the beam waist. It also has to be taken into account that, as already described in 2.3.1, the absorption length depends strongly on the wavelength: according to Eq.2.2 at 910 nm the beam flux decreases

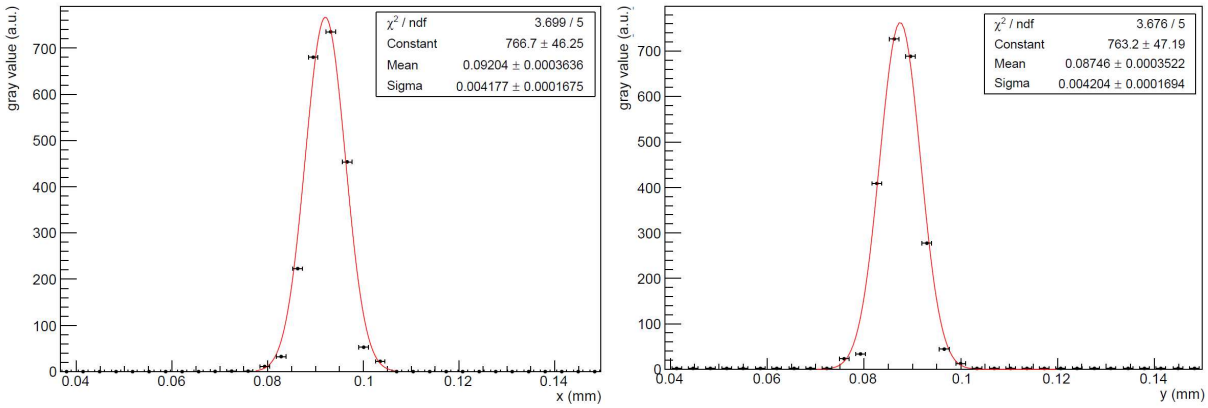

(a) Profile plot along x (b) Profile plot along y

Figure 3.14: Minimum beam spot size

to 36% of its initial value after 37 µm and to about 2% in 150 µm, whereas at 1060 nm the photon flux is decreased to 70% in 300 µm.

Since there is an interplay of several processes and the laser propagation strongly depends on the sensor characteristics, such as thickness of the active region, properties of the surface, and presence of other materials, it is difficult to predict the laser beam characteristics in the device, and it is necessary to perform experimental tests for each specific sensor.

3.2.2 Laser power stability

The amplitude of the reference output signal from the photodiode is computed starting from the waveform acquired by the oscilloscope. In order to have a simultaneous measurement of the reference signal, the data from the oscilloscope are saved on the PC using the free software TekScope Utility (version 1.4.0.0)[3].

This procedure has the drawback of having a data saving rate of $\sim$ 1 Hz. Thus, this has to be taken into consideration when performing tests on sensors: even if the laser pulse rate is much higher, data acquisition has to be sufficiently long to have enough statistics on the reference diode. This issue will be further addressed in Sec.4.2.1. The analog data saved in a .csv file are analysed using a script that first fits the data in a chosen range before the signal to estimate the baseline, and then takes as the peak value the difference between the average of 10 points centered on the experimental maximum value and the baseline.

In Fig.3.15, the fitted baseline is shown and the dotted line represents the value assumed as peak voltage. The signal amplitude is obtained as the difference between these values. The baseline value is (0.87 $\pm$ 0.03) mV and the mean value assumed as the peak value is (54.8 $\pm$ 0.8) mV, therefore the signal amplitude is (53.9 $\pm$ 0.8) mV.

A data acquisition has been done with the following optical settings: λ = 910 nm, V = 50.3 V and the 780HP single mode fibre to test the laser behaviour in terms of power distribution and power fluctuations in time. Data taking was about 500 s long. The σ parameter of the gaussian fit is equal to the 7% of the mean value. A distribution of output amplitude measured by photodiode is shown in Fig.3.16a; during the data taking there were no evident trends in the fluctuations of the laser power (Fig.3.16b).

[3]TekScope Utility Free Software reference: `https://forum.tek.com/viewtopic.php?t=140451`

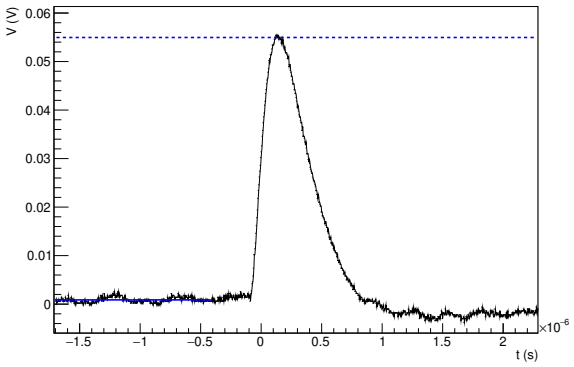

Figure 3.15: The amplitude of a pulse is the difference between the fitted baseline value and the average value of 10 points centered at the experimental maximum.

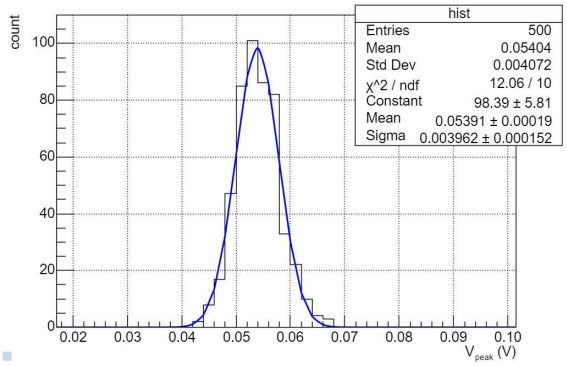

(a) Output amplitude distribution measured with the photodiode in its nominal position.

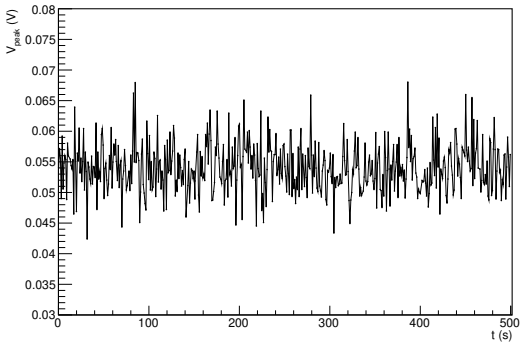

(b) Output amplitude as a function of time

Figure 3.16: Measurement of the amplitude of the output signal of diode during a 500 s time interval (at the nominal diode position along the transmitted beam optical path).

The diode was then moved, from its nominal position on the transmission optical path, to the sensor position, and several acquisitions were made in order to evaluate the effect of statistics on the mean and sigma value of the distribution. The histograms obtained considering samples of 100, 200, 500, 700 pulses are shown in Fig.3.17. There is no evident temporal drift even during the longest 700 s sampling (Fig. 3.17e).

Table 3.1: Comparison of the acquisition with different number of samples

samples	V_{peak} (mV)	σ (mV)
100	30.3 ± 0.2	2.0 ± 0.3
200	29.5 ± 0.2	2.0 ± 0.2
500	28.93 ± 0.09	2.00 ± 0.07
700	28.81 ± 0.08	1.93 ± 0.05

As it can be seen, the values of the sigma of the distribution are in very good agreement with each other in all cases. As regards the mean value, the difference between the values are much larger than the uncertainties associated to the parameter as obtained from the fit. The decrease of the mean value could be due to a slow thermal drift, as it took 25 minutes to complete all these measurements. During these measurements the waveform amplitudes on the oscilloscope were continuously monitored visually; they showed no abrupt power variations, such had occurred in other occasions while performing

sequential measurements over long time intervals.

Having made these considerations, it was decided to limit the size of the data samples to of a maximum of 500 waveforms at a rate of about 1Hz.

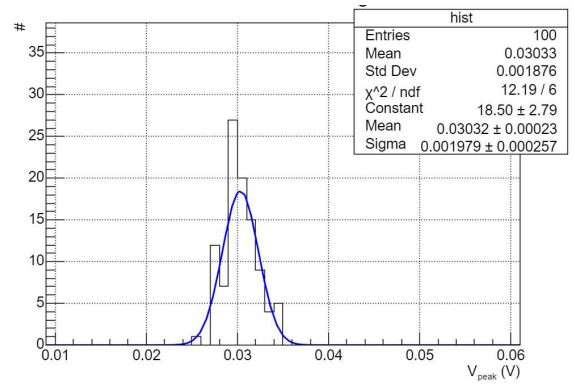

(a) Sample of 100 pulses

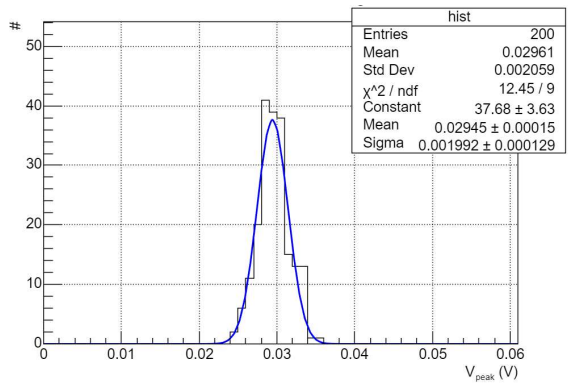

(b) Sample of 200 pulses

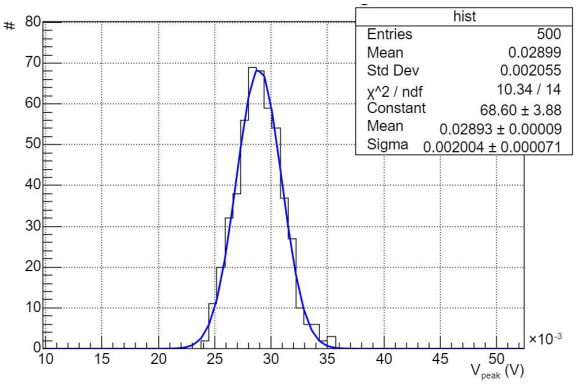

(c) Sample of 500 pulses

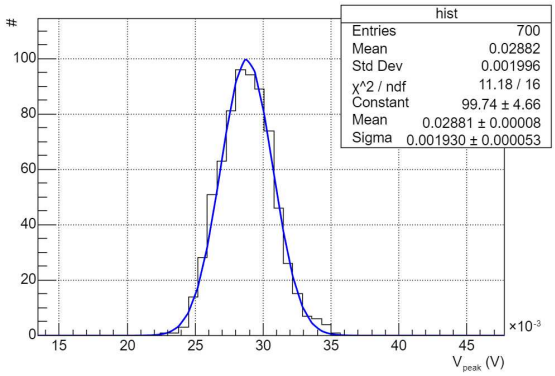

(d) Sample of 700 pulses

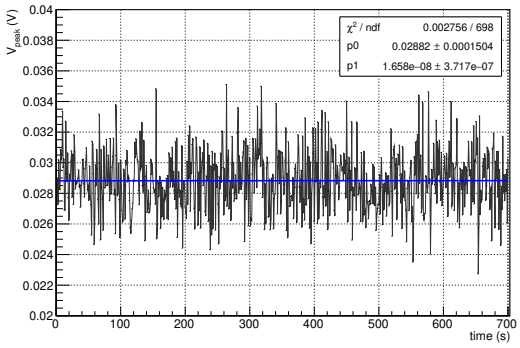

(e) Output signal as a function of time (700 sample)

Figure 3.17: Measurement of the output signal amplitudes of the diode at the sample position (reflected beam optical path)

3.2.3 Position monitoring with camera

The beamsplitter has a split ratio of 50:50. From the datasheet[1], the trasmission and reflection performances are T_{abs}= 47 ± 10% and R_{abs}= 47 ± 10%.

Placing the CMOS camera on the leftover branch of the splitter cube, it is possible to view the sensor: the beam splitter is transparent enough for the coaxial illumination light reflected back from the sensor

[1]Thorlabs Non-Polarizing Beamsplitter: technical specs can be found at: `https://www.thorlabs.us/newgrouppage9.cfm?objectgroup_id=4129`

to be detected. So, by using the objective of the camera, adjusting the focal length and the diaphragm, the device under test can be approximately positioned before using the xy-translation stages for fine motion. As an example, two pictures obtained with the alignment camera are shown in Fig.3.18.

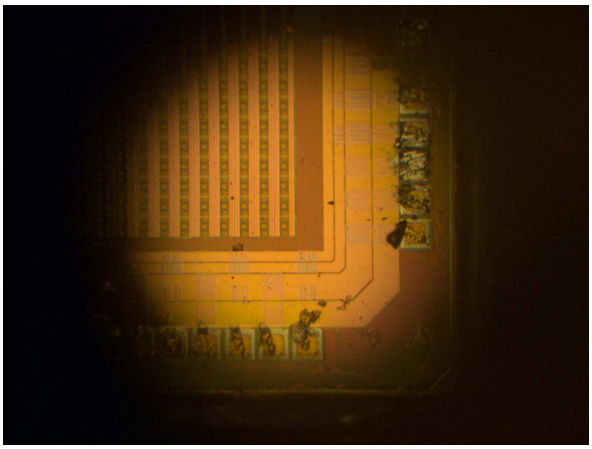

(a) Corner of the MATISSE pixel matrix

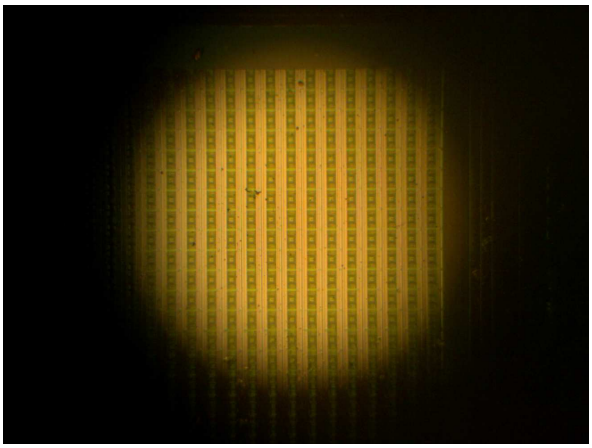

(b) MATISSE pixel matrix

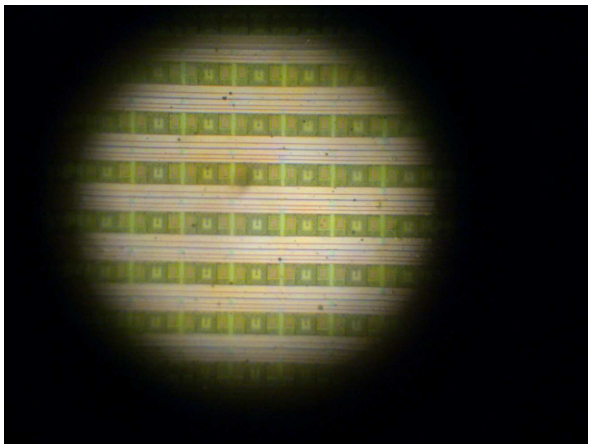

(c) Zoom on the MATISSE pixels

Figure 3.18: Alignment camera system

Chapter 4

Device Under Test: MATISSE

The sensor under study is MATISSE, developed in the context of the INFN project SEED. The device, the DAQ, and acquisition software are briefly described. Moreover, the experimental and data analysis procedure are explained.

4.1 MATISSE

MATISSE (Monolithic AcTIve pixel SenSor Electronics) is an array of fully depleted monolithic pixels developed by the SEED (Sensor with Embedded Electronics Development) collaboration.

The chip is a 2x2 mm^2 ASIC in 110 nm technology subdivided into two parts: the pixel matrix and the End of Column logic.

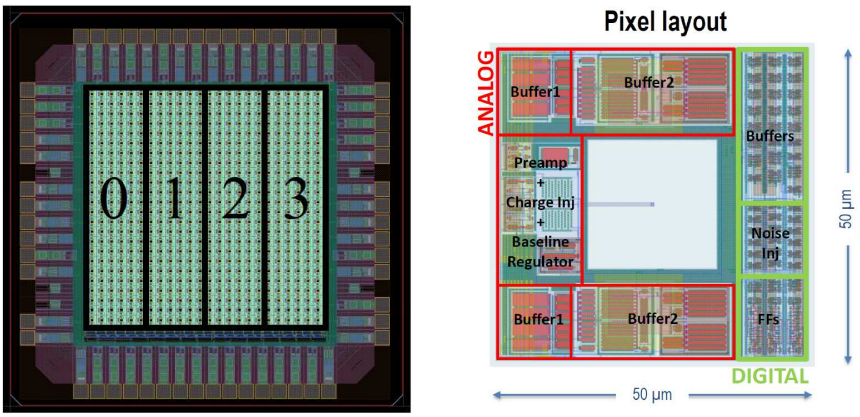

(a) Matrix layout with four sectors

(b) Pixel cell layout [11]

Figure 4.1: MATISSE layout [11, 16]

The pixel matrix hosts 24×24 pixels. Each subgroup of 6 columns of 24 pixels represents a sector of the chip. The layout of the full matrix and of the pixel cell is given in Fig.4.1 and Fig.4.1b.

A pixel cell is 50×50 μm^2. At the centre, there is the sensing diode which occupies an area of 20×20μm^2 and on the sides there is the front-end electronics operating at the low voltage 1.2V. The embedded electronics is the same in the different sectors, but the geometry of the sensing diodes is different, as can be seen in Fig.4.2.[1] The different sensor flavours can be used to identify the optimal solution to increase the signal to noise ratio of the device.

The analogue in-pixel electronics consists of a charge sensitive amplifier, with a feedback capacitance that sets the gain to 130mV/fC, a feedback reset transistor, two capacitors to store the baseline and

[1] Different flavours of the MATISSE chip have been produced and the specific sensing diode of every sector may not be the one shown in Fig.4.2. In any case, the collecting diode is always found at the centre of the pixel cell.

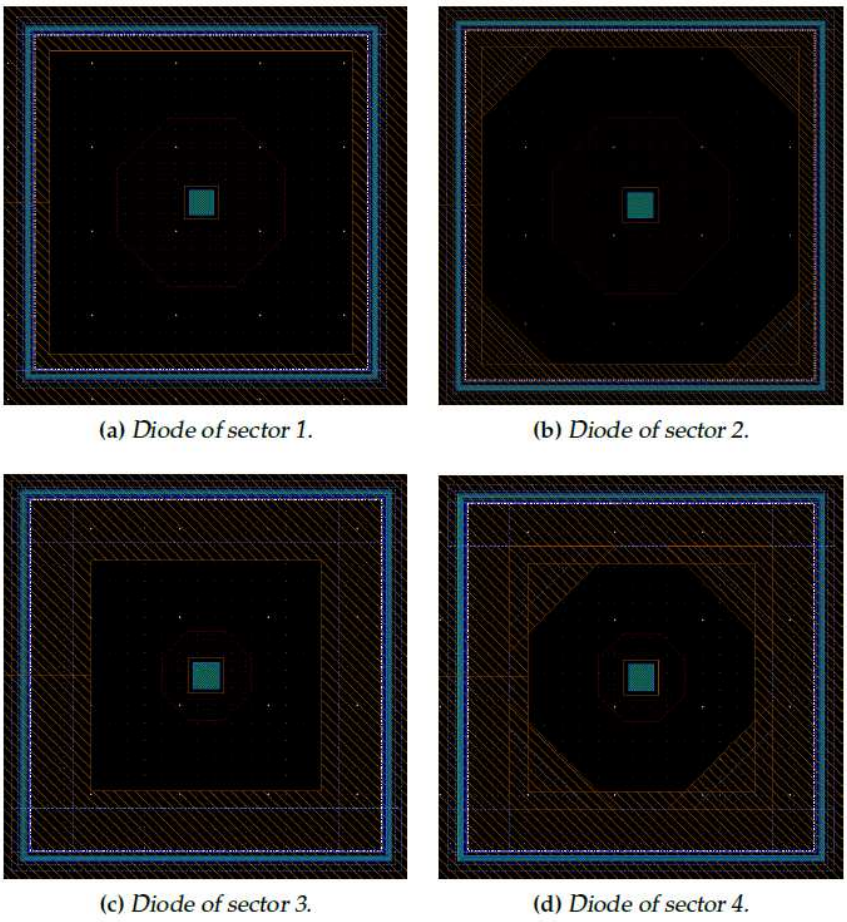

(a) *Diode of sector 1.* (b) *Diode of sector 2.*

(c) *Diode of sector 3.* (d) *Diode of sector 4.*

Figure 4.2: MATISSE: layout of the sensors in the different sectors. [16]

the signal, two switches, and four buffers for signal and baseline data transfer.

The digital part, made of blocks of three flip flops (FF) and buffers, is devoted to the readout process. There is the read FF to readout the signal of a single pixel, the TP FF for the test pulse mode, and a mask FF to switch off noisy pixels. On the bottom part of the pixel area, there is the End Of Column (EoC) block, which hosts all the digital logic needed to process the information collected by the pixels.

The four sectors can be read in parallel. Each sector has a horizontal shift register to address the columns and the readout is controlled by two clock signals: the first clock is used to select the column, while the second one, with a frequency that is 24 times larger, is used to read all the pixels of the selected column. [11, 12]

The sensor that has been tested is 300µm thick and can be fully depleted applying a sufficiently large negative backside voltage $<$ -100 V. The peculiarities that make MATISSE an ideal sensor to test the laser setup are many:

- The backside silicon surface has been processed and polished. While the frontside has several metal layers which makes it very difficult for IR photons to enter the sensing volume, the backside has no metal deposition and therefore light reflection and absorption is minimised.
- Being fully depleted, with backside illumination photons enter directly inside the depleted volume.
- MATISSE is mounted on a mezzanine board, needed to connect the chip with the DAQ system. On the backside a hole has been drilled so that at least a part of the sensor matrix can be directly illuminated from the backside.
- The pixel cell size is reasonably large.

The drawback of this sensor is that having a large thickness (300 µm) that is fully depleted, laser beam can undergo severe changes in terms of beam waist and depth of field, as already discussed in 3.2.1, leading to broader laser spot sizes.

4.1.1 DAQ system and acquisition software

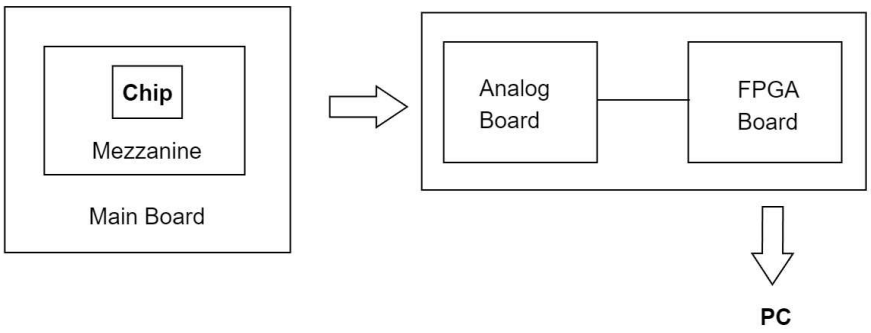

Figure 4.3: Sensor + DAQ scheme

The DAQ system used is a versatile system developed to be used with different pixel detectors making minimal changes: it is described in [1].

It consists of a custom analog board with 5 independent analog channels with tunable gain and impedance that can be used to connect sensors with up to 5 parallel output channels or up to 5 different single channel detector. The analog board has a 100 MS/s 14-bit ADC that is driven by a 100 MHz reference clock provided by the board itself or by an external clock.

The analog board is connected via two high-speed SAMTEC connectors to a commercial FPGA board, Xilinx Virtex 5. The communication between the FPGA and the PC is via a USB 2.0 cable and it provides about 25 Mb/s of continuous stream capability. [1]

For the acquisition with MATISSE, the DAQ system is connected to a first board, the MATISSE Main Board, which is provided with two connectors the mezzanine board hosting the chip can be plugged in. These two boards are detector-specific and host the first part of the electronic readout chain. The scheme with the different elements is shown in Fig.4.3 and Fig.4.5.

The DAQ system comes together with a devoted software based on ROOT/C++ and with a ROOT GUI graphical interface [2].

From the software interface, shown in Fig.4.4, it is possible to control the data acquisition and set several parameters, such as the acquisition settings mode, the DAQ parameters, such as the readout clock frequency, and perform different types of online processing of the data. The software provides also an online visualisation of the pixel matrix. Several measurements and plots can be checked online. The pixel matrix visualisation provides also real time clustering.

4.2 Experimental and data analysis procedure

4.2.1 Experimental procedure

MATISSE

The acquisition is organised the following way.

- A frame is the basic unit of the acquisition data: when the matrix is readout, all the information related to all pixels are recorded in a frame.
- A burst is a sequence of consecutive frames; a typical burst consists of 16 frames.

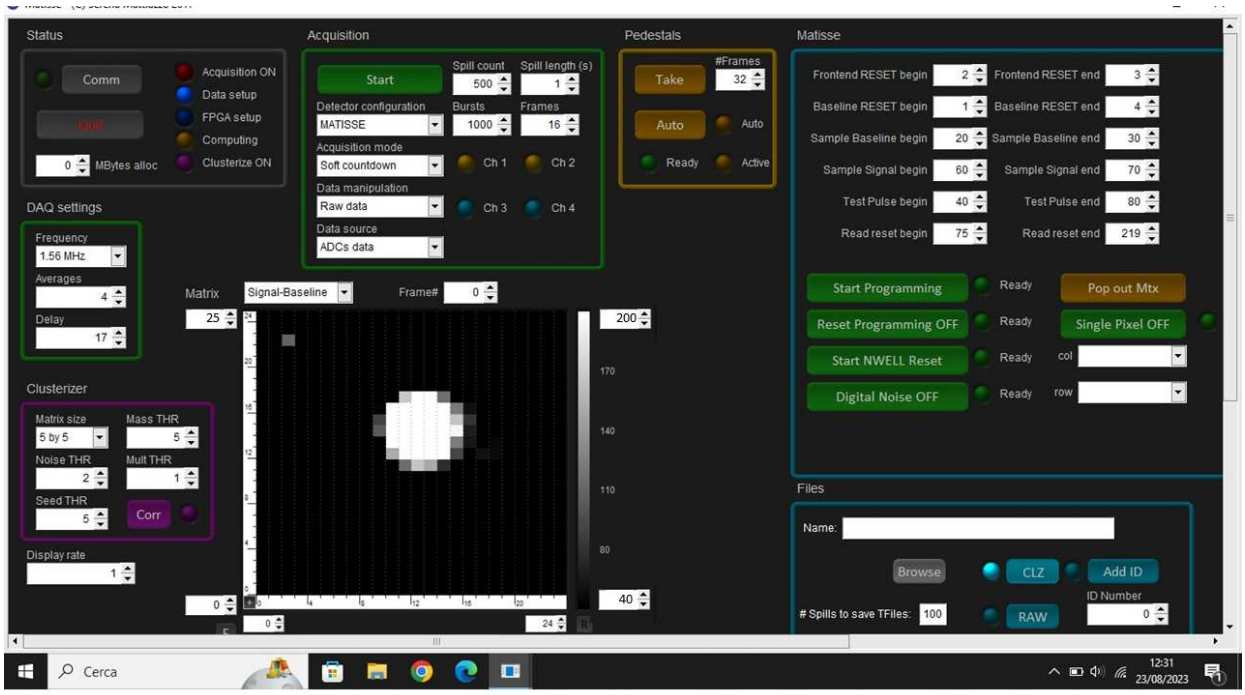

Figure 4.4: Cool software interface. A large spot is shown in the display in real time.

- A spill contains a certain number of bursts of 16 frames; a typical spill has 1000 bursts, for a total of 1600 frames.
- The number of spills corresponds to the number of output file generated.

The DAQ system can run in three ways, both in software or hardware trigger:

1. single shot mode: the system acquires a single burst;
2. continuous mode: the system is free running and the operator can stop it at anytime;
3. countdown mode: the system runs until a specified number of spills is reached. This mode allows one to control the number of frames in order to, for instance, unify the statistics of different data taking runs.

The output files can be saved as RAW or CLZ (cluster). In RAW files, all the information related to every pixel is saved, whereas in CLZ mode, that is the one the sensor is typically operated in during data acquisition, the DAQ performs an analysis based on the signal-to-noise ratio (SNR) to select the pixels of interest, called seed, and it saves all the information for a matrix of typical size 5×5 around the seed pixels. This will be further explained in 4.2.1.

The sensor is fully depleted setting the bias voltage to V = -134 V and a DC power supplier is used to power the electronics of the Main Board with ±5V. On the software, a 1.56MHz clock frequency is set. The acquisition mode is set in software countdown.

Laser source, trigger, and number of photons

The laser source can operate with an external trigger to synchronise the laser frequency in order to be sure that the laser pulse is hitting the sensor within the acquisition window of the readout cycle. Looking at the readout cycle signals in Fig.4.6, this window is the time interval between the rising edge of the sample baseline and the falling edge of the sample signal. At the chosen clock frequency (1.56 MHz) and window duration (40 clock cycles), it lasts about 30 μs.[2] The DAQ provides a sample

[2]Fig.4.6 is shown as a reference of the sequence of signals of the readout cycle; however, the time scale indicated in the figure is not correct, since it depends on the chosen frequency. At the working clock frequency of 1.56MHz, all the time intervals between the different signals are about 10 times larger.

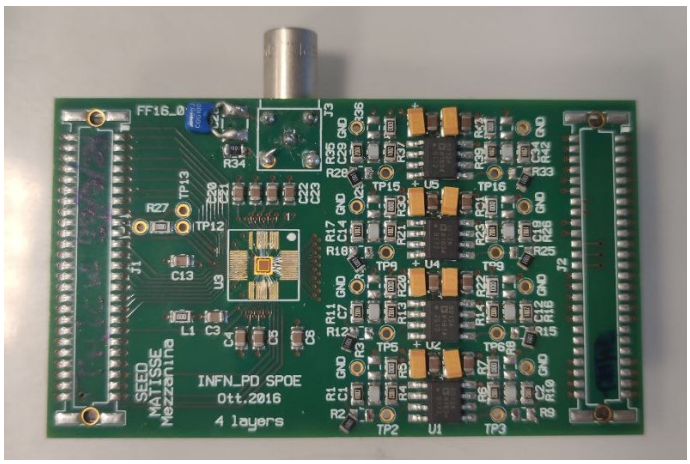

(a) MATISSE chip: sensor and mezzanine board

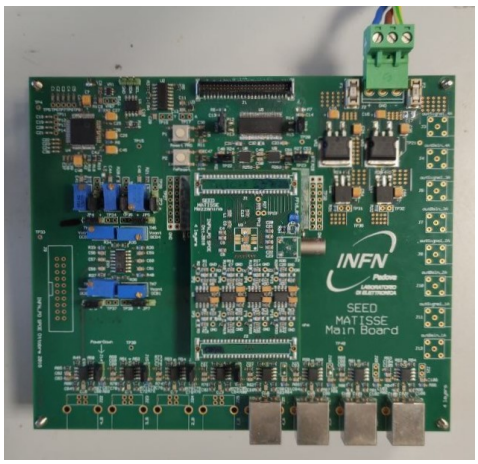

(b) MATISSE on the Main Board

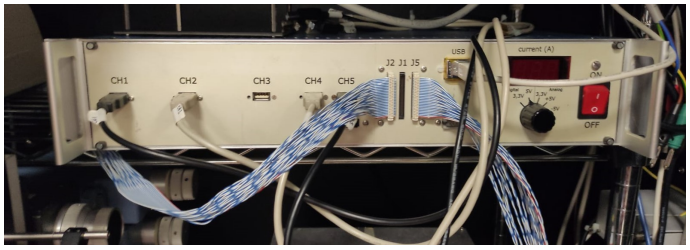

(c) DAQ box

Figure 4.5: Setup: MATISSE chip with relative boards and DAQ

baseline signal that, once manipulated, can be sent to the laser source as an external trigger signal. For this purpose the sample baseline signal the voltage level must be reduced to 1.5 V and delayed (by about 170 ns); this is done using a pulse generator.

The amount of charge injected into a sensor is directly related to the number of photons per laser pulse, and this can be varied using different methods:

- the supply voltage of the laser can be varied in the 14-50 V range;
- the actual laser power on the device under test can be changed using an optical lever diaphragm (iris) placed before the beam splitter;
- different optical fibres and coupling can be used.

Photodiode

The photodiode signals are acquired and saved on the PC using the TekScope Utility software. The photodiode acquisition, as already mentioned in Sec.3.2.2, cannot occur at a higher frequency than about 1Hz. As it will be discussed in the following section, this does not affect too much the measurements provided that the acquisition time is sufficiently long to ensure adequate statistics of photodiode output waveforms.

Motorised translation stage

The motion of the translation stage can be remotely controlled connecting the stage via USB to the PC either using the Thorlabs Kinesis® software or via scripts in Python implementing the .NET Command Line libraries. A Python script has been written and tested, but for the measurements presented in this thesis, the sensor was moved, using the provided software, to make separate acquisition runs for different positions and the soft countdown acquisition mode was used in order to have the same statistics in different runs. We have not yet tested a system to externally trigger the motion stage whereby we could automatise the motion procedure.

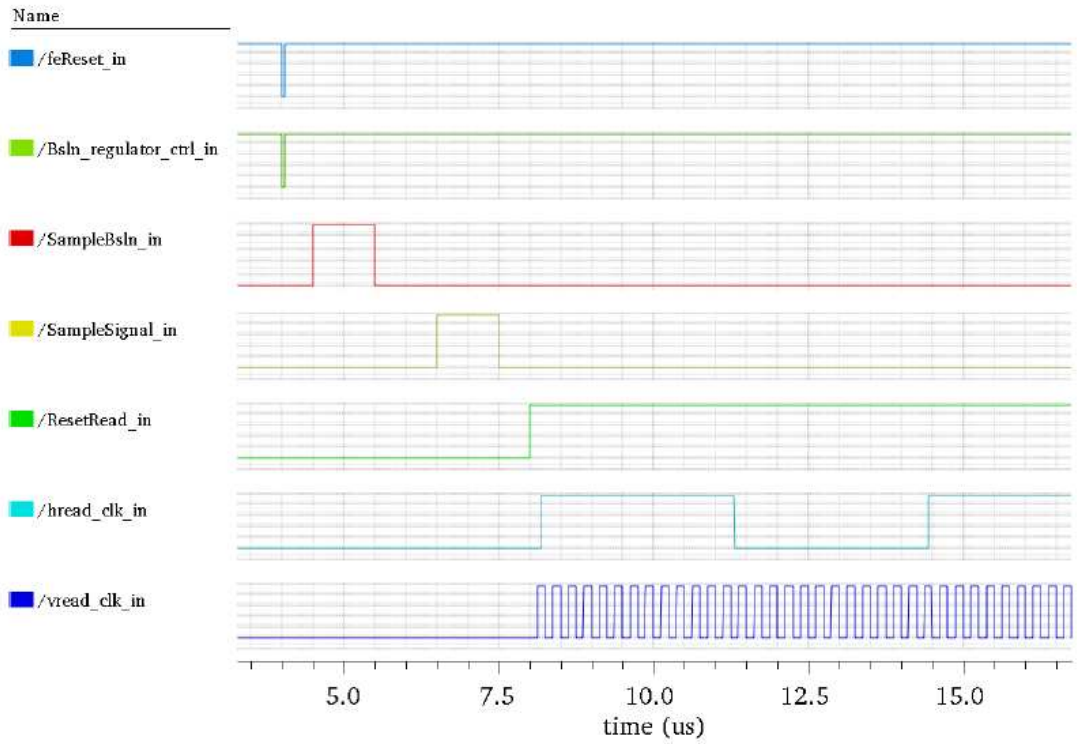

Figure 4.6: DAQ: Readout cycle signals [16]

4.2.2 Data analysis procedure

An acquisition run is structured as follows. First, a pedestal run is performed to get the noise and baseline values for every pixel. This run consists of a certain number of frames (32) that are used to fill a histogram of the signal measured for every pixel. The resulting distribution is fitted with a gaussian: the mean of the gaussian fit is the baseline value of the pixel, and its noise is the sigma.

The laser is turned on and the acquisition in software countdown is enabled. During the acquisition, for each pixel, the ratio between its signal and noise values is compared to a threshold, called seed threshold, which is set to 5. If the ratio is above the seed threshold for a certain pixel, that pixel is considered a seed, the signal is called a seed signal, and the information (noise, baseline, signal, ...) of all the pixels in a 5×5 matrix centered on the seed of size is saved (Fig.4.7).

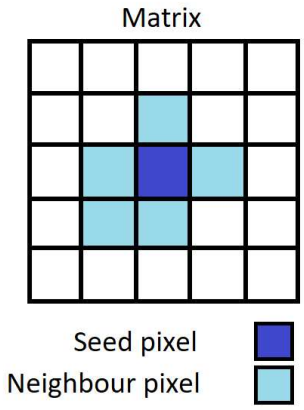

Figure 4.7: The 5×5 matrix centered on a seed pixel and a cluster with a multiplicity equal to 6 (see the text for the definitions of cluster and multiplicity)

Offline, a software is used to re-analyse the information of all the 5×5 matrices of the seeds saved during the acquisition. Typically, in the offline analysis, the seed threshold is raised to 6 and a second

threshold, named noise threshold, lower than the seed threshold, is established. For a given seed, the pixels of its 5x5 matrix[3] are assigned to be part of a cluster (of pixels) if the ratio between the pixel signal value and noise value is above the noise threshold, usually set to 4. A sketch that can be useful to visualise the analysis is given in Fig.4.7: the pixel highlighted in blue is the seed pixel, the pixels in light blue are the neighbour pixels, and the cluster is composed of the seed pixel and the neighbour pixels. The multiplicity of a cluster is defined as the number of pixels that belong to the cluster. Therefore, the multiplicity quantifies the number of pixels that gives a signal related to the same event, i.e. the total charge collected of the event.

4.3 Preliminary tests

The hole in the mezzanine board we used is smaller than the matrix area and, depending on how the chip has been positioned and glued, might not be centered under the laser beam. In order to check which part of the chip can be illuminated without being too close to the borders of the hole, a check was made using a large spot size and moving the board along the pixel matrix.

Four pictures, that provide a reference of the available area, are shown in Fig.4.8. They were acquired using the live visualisation of the pixel signal provided by the GUI software. As can be seen, the hole is centered in sector 2, while a few columns of sector 1 and 3 are partially illuminated, while sector 0 is completely hidden.

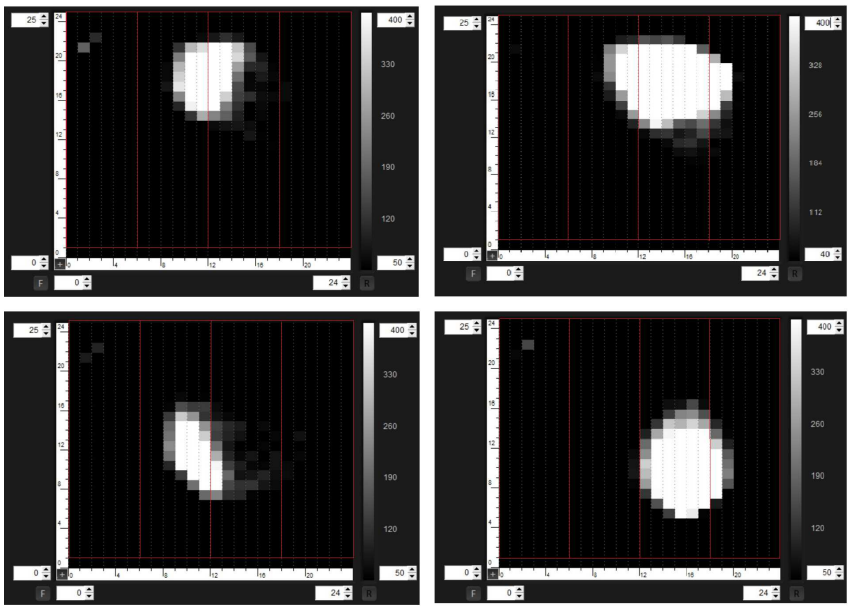

Figure 4.8: Determination of the pixels that are illuminated through the backside hole on the mezzanine board

4.3.1 Energy calibration with a Fe-55 source

A data acquisition with a ^{55}Fe radioactive source has been performed to calibrate the sensor response in energy. The ^{55}Fe radionuclide decays via electron capture to ^{55}Mn emitting Auger electrons and X-rays. The relevant transitions in our case are the k-α1 X-ray with the energy E=5.899 keV with a relative intensity of 16.2±0.7%, and the k-α2 X-ray with the energy E=5.888 keV with relative intensity 8.2±0.4%.[4] The energy resolution of the sensor is not high enough to distinguish the two peaks; for this reason we use, as reference energy, the combined value of 5.9 keV.

[3] In the offline analysis it is possible to confine this cluster analysis to smaller 3×3 matrices

[4] Data taken from the NNDC BNL database: `https://www.nndc.bnl.gov/nudat3/DecayRadiationServlet?nuc=55Fe&unc=NDS`

The source was positioned on top of the sensor using a supporting platform with a hole. The data acquisition was 90 minutes long. Performing the analysis of the clusters, the histograms shown in Fig.4.9 have been obtained for each sector of the matrix. Every histogram was fitted with a gaussian distribution in order to get the mean value expressed in ADC that would correspond to the energy of the X-ray peak. The parameters, expressed in electrons/ADC and fC/ADC, are the ones in Tab.4.1, computed starting from the mean ADC value of the gaussian fit, $\bar{x}$, and applying the following formula, recalling that 3.6 eV is the average energy needed to produce an electron-hole pair in silicon.

$$G = \frac{5900[eV]}{\bar{x}[ADC] \cdot 3.6[eV/electrons]} = \frac{1638}{\bar{x}} \left[\frac{electrons}{ADC}\right] = \frac{0.2624}{\bar{x}} \left[\frac{fC}{ADC}\right] \tag{4.1}$$

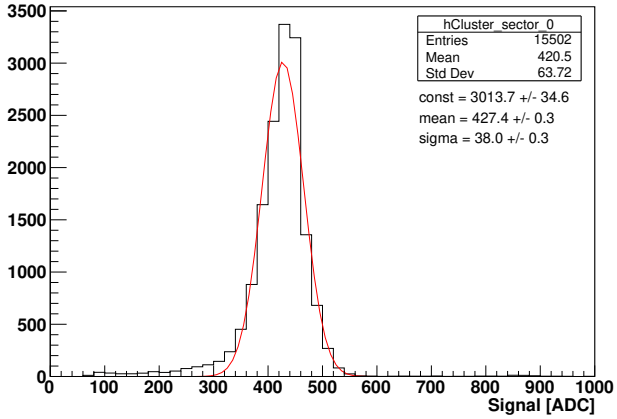

(a) Sector 0

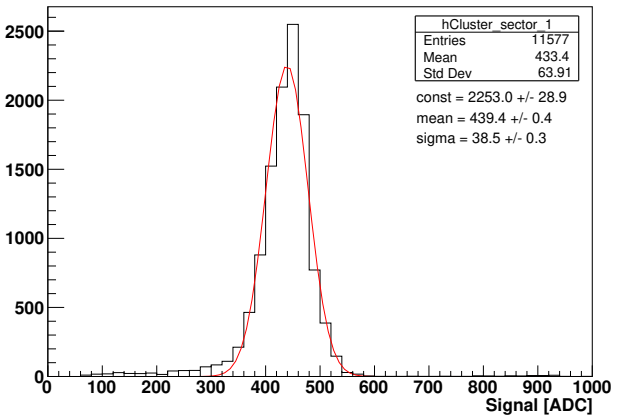

(b) Sector 1

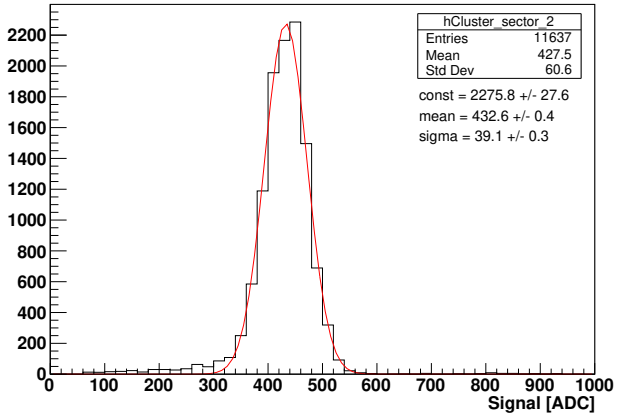

(c) Sector 2

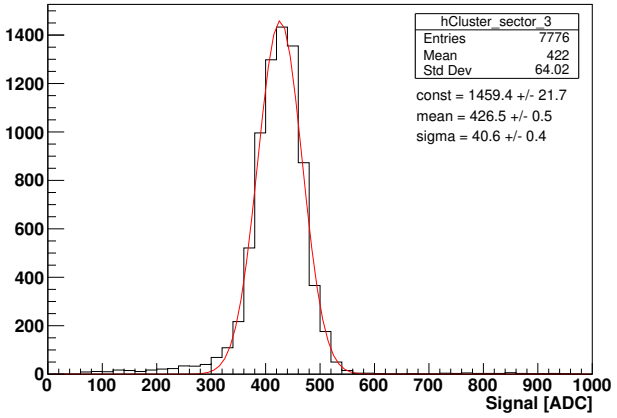

(d) Sector 3

Figure 4.9: Measurement with Fe-55: Cluster signal distribution for all sectors

Table 4.1: Calibration factors for every sector

sector	G [electrons/ADC]	G [fC/ADC]
0	3.825 ± 0.003	$(6.13 \pm 0.04)\ 10^{-3}$
1	3.729 ± 0.003	$(5.97 \pm 0.05)\ 10^{-3}$
2	3.788 ± 0.004	$(5.61 \pm 0.06)\ 10^{-3}$
3	3.842 ± 0.005	$(6.15 \pm 0.06)\ 10^{-3}$

Chapter 5

Measurements

The measurements performed with MATISSE are reported in this chapter. In particular, the emulation of a MIP signal, the analysis of the difference between the two possible working wavelengths, 910 and 1060 nm, and the response of pixels in terms of linearity and charge collection are discussed. Being MATISSE a well-known and reference sensor, these measurements can be used to validate and demonstrate the setup capabilities.

5.1 Introduction

In this chapter the plots that are shown are:

- Seed signal distribution: the histogram of the signal in ADC counts of the seed pixels.
- Cluster signal distribution: the histogram of the total signal in ADC counts obtained summing the signals of all the pixels belonging to the same cluster in a specific sector.
- 2D cluster maps: for every cluster, a bidimensional map is built considering a 5×5 matrix and assigning to every pixel the corresponding signal; the 2D map of an acquisition run is then obtained summing all the maps. This provides a useful and immediate visualisation of the charge distribution in the clusters.
- Other plots with additional information: the seed coordinates are given in terms of row and column number histograms; the multiplicity can be studied looking at the distribution of the number of pixels in the clusters.

The histograms are often presented not in terms of ADC, but in terms of electrons. This is done using the calibration measurements presented in 4.3.1. Given how low energy photons interact in silicon (see Sec.2.3.1), the number of electrons released in silicon is equal to the number of incident photons that have been absorbed.

5.2 Emulation of a MIP signal

The goal of these measurements is to evaluate the capability of a laser to reproduce the signal of a MIP. There are several differences that have to be taken into account when comparing a real MIP signal and an equivalent signal induced by a laser pulse traversing the sensor:

- Longitudinal charge density distribution: a MIP releases 80 $e^-/\mu m$ uniformly along its track through the active thickness of a sensor (Fig. 2.4). On the other hand, in the case of a laser pulse, there is an exponential absorption of photons. For these measurements, at the chosen working wavelength of 910 nm, the distribution of the charge is not uniform as $(1 - 1/e) \times 100$ = 63% of the photons are absorbed in the first 37 μm; i.e. most of the charge is released in the initial thickness. A better emulation of a MIP signal could be obtained choosing a longer light

wavelength, since it corresponds to a shorter absorption depth and, thus, to a weaker photon absorption. This implies that the released charge deposition would be much more uniform. For a wavelength of 1060 nm, the characteristic absorption thickness is $\mu = 845\mu m$ and only 30% of the photons are absorbed in the full 300 µm sensor thickness [1]. However, a longer working wavelength has drawbacks in terms of optical processes that can occur such as possible reflections from the metal layers on the frontside of the sensor, that are much more unlikely to take place using the 910 nm source, since in that case the 99.97% of the beam is absorbed in a depth equal to the sensor thickness. Measurements have been done in both cases, and results are shown and discussed in 5.2.1 and 5.2.2

- Transversal charge density distribution: an ideal MIP track is normally incident on the sensor surface. To first approximation, disregarding possible misalignment, the laser beam is normally incident on the surface, but the beam spot can be relatively huge, compared to the cross-section of the ionisation deposit of a MIP track, and variable in terms of size as it propagates into the silicon.

- Due to the different type of interaction processes, the deposited energy distribution of MIPs in a 300 µm thick sensor is a Landau distribution, whereas a photon beam gives a Gaussian. The reference value of 80 $e^-/\mu m$ is related to the Most Probable Value (MPV) of the Landau distribution.

5.2.1 Working wavelength 910 nm

The goal was to achieve a calibrated laser induced signal that would be, in terms of released charge, equivalent to that of the most probable value of a MIP; i.e. with the laser gaussian centered on the MPV of the MIP Landau. The laser beam was focused on the surface of the sensor checking the symmetry of clusters with the online cluster visualisation of the acquisition software, and using the xy translation stage in order to center the beam on one pixel of sector 2. The laser power was tuned to get the desired signal in terms of incident photons on the sensor.

As can be seen from Fig.5.1, in sector 2 the seed signal is always found on the same pixel, as wanted. The analysis of the clusters was performed considering 5×5 matrices of pixels. The mean value of the multiplicity is 6.788 ± 0.002, with only 0.007% of the clusters with multiplicity 10, that is the maximum value of multiplicity.

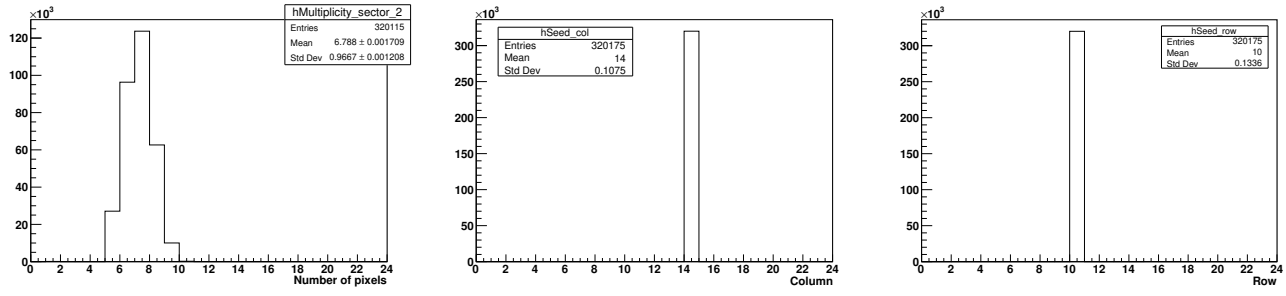

(a) Cluster multiplicity (b) Seed column (c) Seed row

Figure 5.1: Multiplicity of the cluster, seed column, and row

The histograms of the energy loss in terms of electrons (obtained using the calibration factors given in 3.1.2) are shown in Fig.5.2. From the gaussian fit of the energy loss spectra in electrons, the average value is obtained and shown in Tab.5.1 [2].

[1] $[1 - exp(-300\mu m/\mu)] \times 100 = 30\%$

[2] The characteristic attentuation length of 910nm photons is 37 µm. The charge deposition is exponentially decreasing. In the 1060 nm case discussed in 5.2.2 instead the charge deposition is much more uniform, as the attentuation length is 845 µm, and it will make sense to divide the deposited charge by the thickness of the sensor to obtain the released charge per micron.

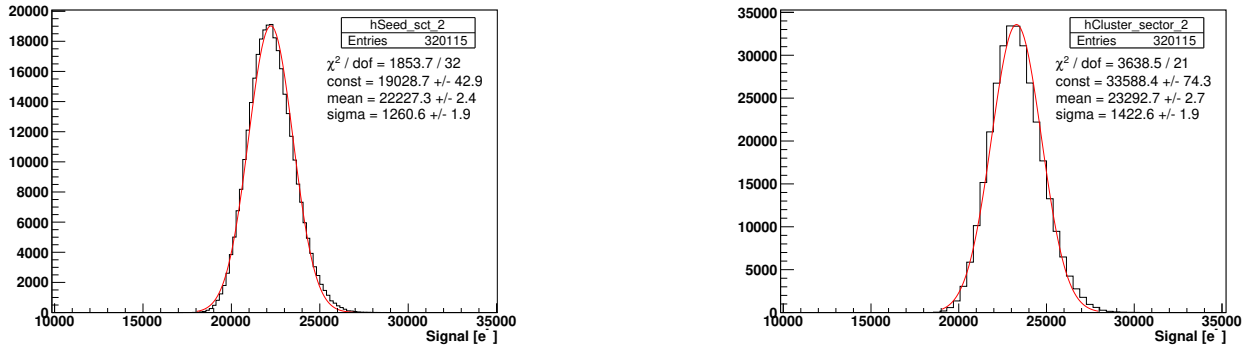

(a) Energy loss distribution for seed pixel

(b) Energy loss distribution for cluster

Figure 5.2: 910 nm working wavelength: Emulation of a MIP signal

Table 5.1: 910 nm working wavelength: released charge in terms of e^-

signal	$\bar{Q}$ (e^-)
seed	22227 ± 2
cluster	23293 ± 3

The total charge released in the entire thickness of the sensor is close to an ideal MIP signal, smaller by only a factor of 3%.

From these measurements, some considerations on the laser beam behaviour in the sensor can be made. A map of the cluster, in terms of charged measured by each pixel in the cluster, is computed starting from all analysed clusters. This is done by summing the measured pixel signals in ADC counts pixel by pixel for all clusters. In Fig.5.3, the cluster map is shown both as a 2D plot in log scale and as a 3D plot in order to clearly visualise the relative difference between the different pixels.

In Fig.5.3b, the 2D plot has been rescaled in terms of relative percentage pixel signal. The central pixel signal is the 89% of the cumulative sum of all cluster signals; the four pixels at the sides of the seed pixel are 2–4% of the sum. The distribution is quite centered, although, comparing the relative signal of the pixel at the external corners, it can be seen that there is a small positive offset in the x-direction and a smaller negative offset in y-direction can be appreciated by looking at the difference in the sum of measured signals on the rightmost column.

To first approximation, since the pulsed laser is exiting from a single mode fibre, it can still be assumed that it behaves as a gaussian beam. From these measurements, one can estimate the maximum beam spot diameter along the propagation of the beam through the sensor thickness. In fact, for a gaussian distribution, the 86% of the area is found within the beam waist. Therefore, it can be estimated that the maximum beam diameter, occurring during beam propagation in the sensor, is less than the 50 µm pixel size.

Given this distribution, one can estimate the displacement of the centre of the distribution, with respect to the centre of the pixel, by computing the centroid in terms of mean value of the row signals and column signals. The (x,y) coordinates of the centroid are (14.02744, 10.00057) in matrix coordinates. Assuming that the the laser spot does not move (that movements of the optics and of the supporting elements, on an event-by-event basis, are negligible), this result provides an estimate of the shift in position of the beam spot centre with respect to the centre of the seed pixel. The results are: $\Delta x = (1.3720 \pm 0.0003)$ µm and $\Delta y = (0.0285 \pm 0.0003)$ µm. The uncertainties are extremely small as they are only the statistical uncertainties of the mean values.

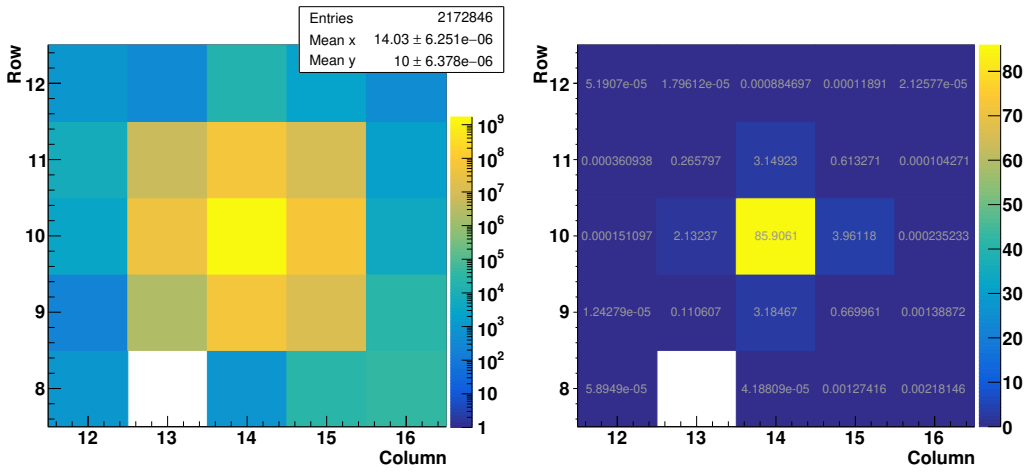

(a) 2D map of total cluster signal (log scale) (b) 2D map of total cluster signal (relative signal in percentage)

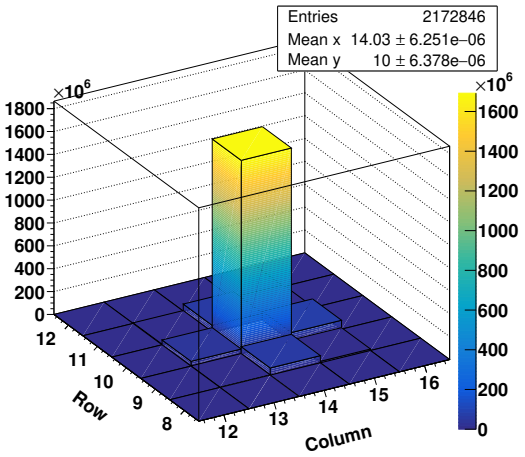

(c) 3D map of total cluster signal

Figure 5.3: 910 nm: charge distribution in cluster (z-coordinate unit is ADC counts)

5.2.2 Working wavelength 1060 nm

As already mentioned, measurements in order to emulate a MIP signal have been performed also using the laser pulsed beam with λ=1060 nm. The optical fibre 1060XP was used as it is optimised for the working wavelength. The beam was attenuated tuning down the laser power, and by changing the diaphragm opening and lens position.

During measurements, secondary clusters of lower signal intensities were detected, with multiplicity and signal intensity that increase with the laser supply voltage. Figure 5.4a shows the seed map of sectors 2 and 3 (with no cuts on the columns) with the laser illuminating the pixel, the true seed, at position (14,14). The presence of an important secondary seed on the same row but with a horizontal shift of three pixels to position (14,17) is clearly visible looking at the seed column and row distribution in Fig.5.4b and Fig.5.4c. Figure 5.5 shows the distribution of the cluster signal in sector 2 with the laser illuminating pixel (14,14). Indeed two distinguishable populations are visible: the higher ADC population is the true cluster signal; the lower ADC population is the signal of the secondary clusters. A possible explanation of the appearance of these secondary clusters is that they are due to photons of the laser pulse that are reflected by metal layers on the front side of the chip.

In this specific case, the secondary cluster would be actually removed during the offline analysis due to the fact that its seed pixel is on the rightmost column of sector 2: such seeds are always excluded as their clusters straddle between two sectors. However, in order to reject the above mentioned secondary seeds, it is sufficient to set a higher seed threshold.

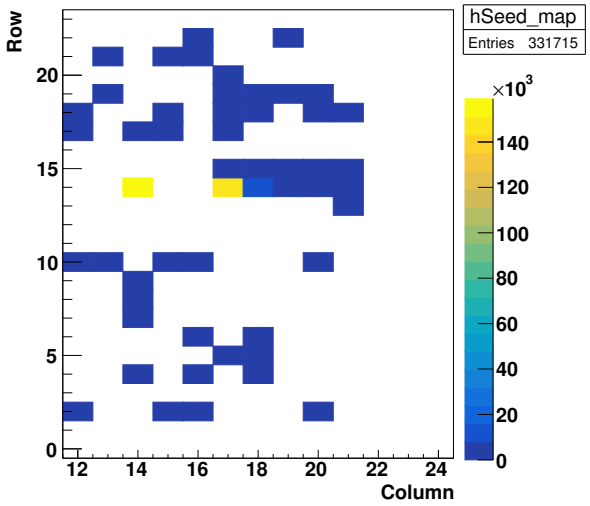

(a) Seed map for sector 2 and 3. The true seed pixel is in column 14 and row 14; the secondary seed is in 3 pixels to the right, in column 17. An even weaker secondary cluster is in column 18, barely visible, with a lighter shade of blue.

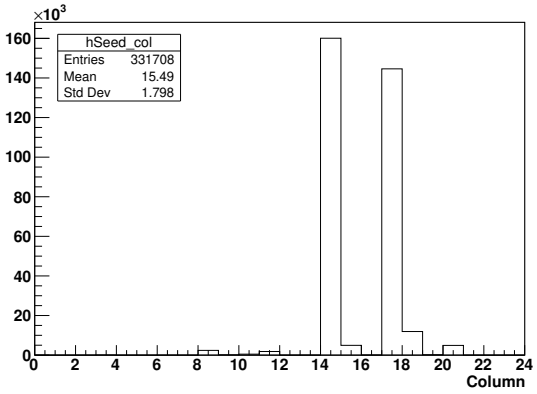

(b) Seed column

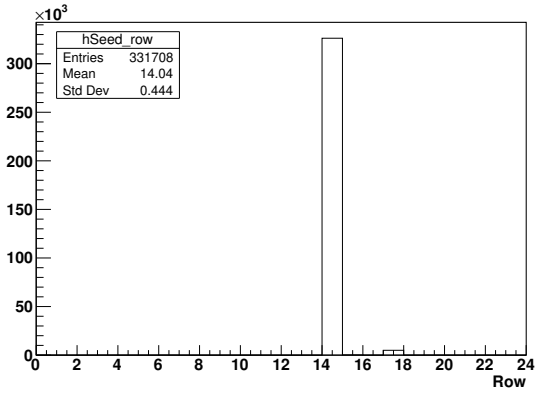

(c) Seed row

Figure 5.4: 1060 nm working wavelength: seed map, seed row and column distributions. Secondary seeds are visible.

Setting the seed threshold to 12 instead of 6 rejects the seed at column 17, as it can be seen from the row and column histograms in which only the entry related to the index 14 is filled, see Fig.5.6. In the cluster signal plot, in Fig.5.6c, the peak centered at 6900 ADC counts is unchanged, but the population at lower values is no longer present.

The seed signal and cluster signal distribution, converted in electrons, are shown in Fig.5.7b. From the values of the mean of the fit, the equivalent average deposited charge can be computed. Furthermore, as the attenuation length in silicon of 1060 nm photons is 845 µm, one can calculate the equivalent charge per micron. The results are shown in Tab.5.2. The equivalent charge per micron obtained from the cluster signal is about 8% larger than the reference value for a MIP.

Table 5.2: 1060 nm working wavelength: released charge in terms of e^- and $e^-/\mu m$

signal	$\bar{Q}$ (e^-)	$\bar{Q}$ / µm (e^- / µm)
seed	19303 ± 1	64.340 ± 0.003
cluster	25962 ± 2	86.540 ± 0.007

In this case, there is a much more significant difference between seed and cluster signal mean value

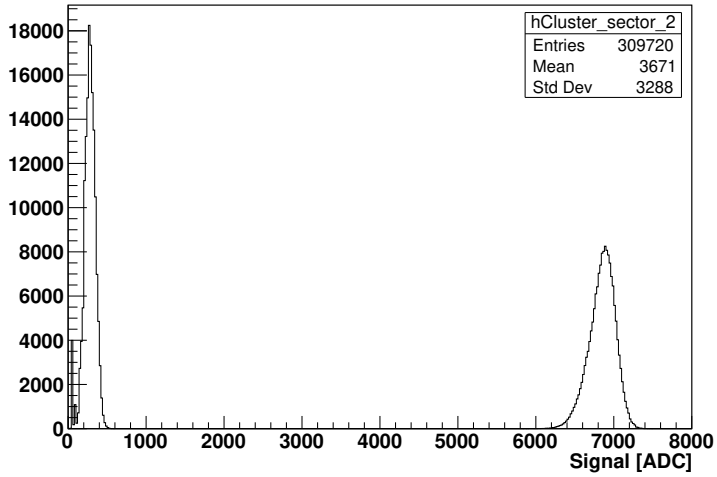

Figure 5.5: Signal distribution for clusters in sector 2. The true cluster signals are around 6900 ADC counts; the secondary cluster signals are around 300 ADC counts.

and, comparing the mean value of the multiplicity in Fig.5.1a and Fig.5.7c, the cluster multiplicity in the 1060 nm case is larger. Possible explanations are that in this case the beam spot broadens, due to the weaker absorption, and that it was not as well centered as in the previous case. In fact, from Fig.5.8a and 5.8b, it can be seen that the centroid is shifted with respect to the centre of the seed pixel with Δx = 7.5 and Δ y = 5.5 µm. This slight displacement bring much less symmetric seed and cluster distributions that show a left tail.

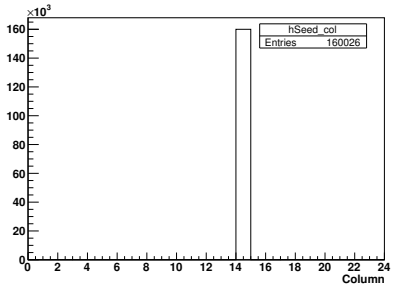

(a) Seed column

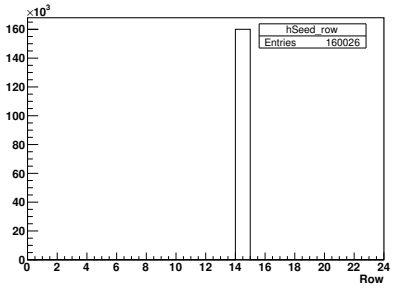

(b) Seed row

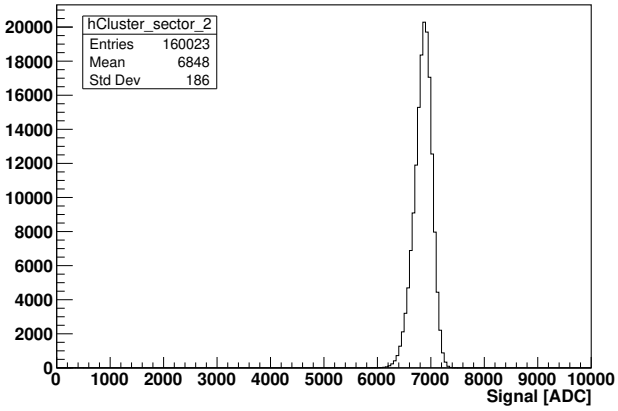

(c) Signal cluster distribution after the change of threshold. The peak centered at about 6900 ADC counts in unchanged.

Figure 5.6: Analysis of the data with a higher seed threshold set to 12 instead of 6. Only the cluster signals related to the seed (14,14) are left.

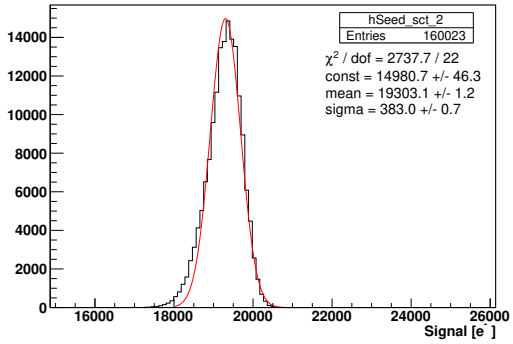

(a) Signal distribution for seed pixel

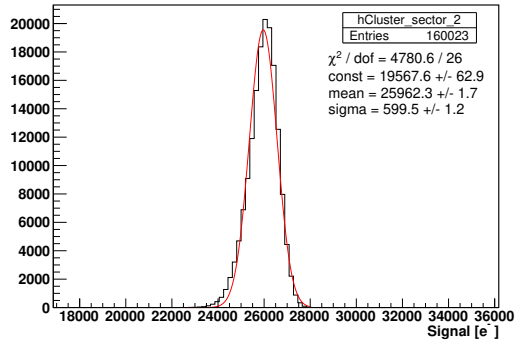

(b) Signal distribution for clusters

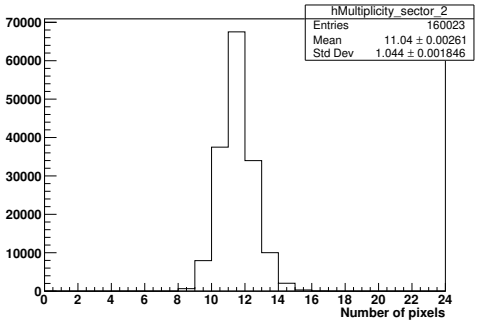

(c) Cluster multiplicity

Figure 5.7: 1060 nm working wavelength: emulation of a MIP signal with modified seed threshold

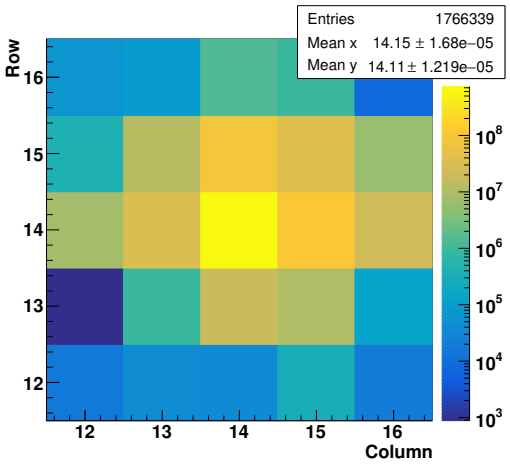

(a) 2D map of total cluster signal (log scale)

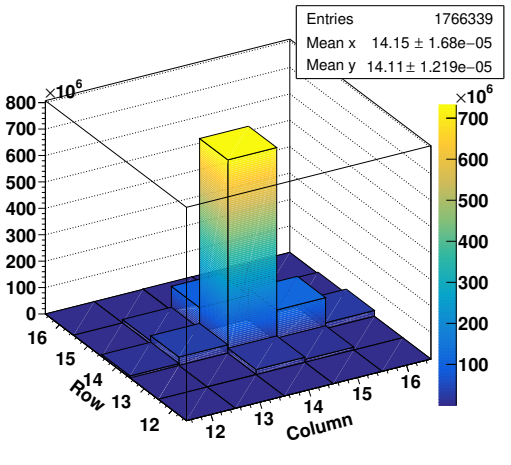

(b) 3D map of total cluster signal

Figure 5.8: 1060 nm working wavelength: charge distribution in cluster (z-coordinate unit is ADC counts)

5.2.3 Minimal cluster multiplicity

The emulation a MIP-like signal with the 910 nm and 1060 nm laser pulses leads to a relatively large cluster multiplicity: about 7 in the 910 nm case and 11 in the 1060 nm, as can be seen in Figures 5.1a and 5.7c respectively.

The minimal cluster multiplicity achieved was obtained using the 910 nm laser with an equivalent number of incident photons/pulse on the sensor of about 5000. In this case the average multiplicity is about 2, as can be seen in Fig. 5.9a, using the standard threshold value for clustering defined in 4.2.1, and the ratio between the mean value of the gaussian fit of the seed in Fig.5.9b and the matrix

histogram, computed considering all pixels belonging to the 5x5 matrix, in Fig.5.9c, is 88%.

This special condition can be used to test single pixels, for example in terms of charge collection as it will be discussed in 5.5. Using the 1060 nm instead, it is challenging to go below 4 pixels per cluster due to the broadening of the beam.

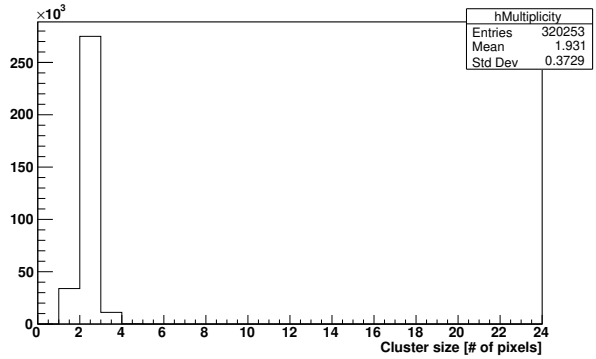

(a) Cluster multiplicity

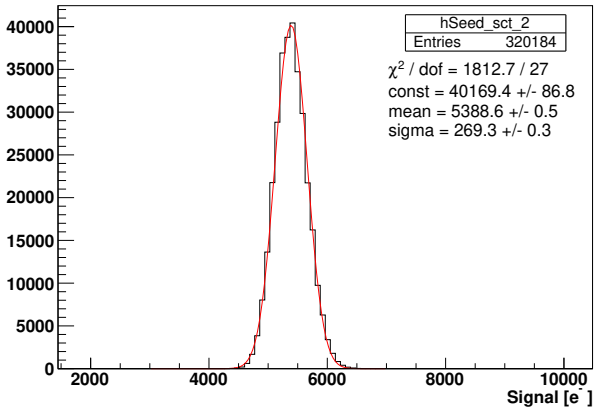

(b) Seed signal distribution

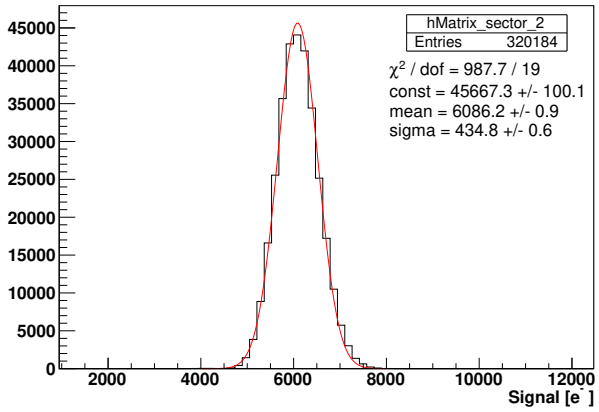

(c) Matrix signal distribution

Figure 5.9: Plots relative to the minimum condition achieved in terms of cluster multiplicity

5.3 Pixel response

As the setup allows simultaneous reference measurements of the laser power, the response of pixels as a function of the reference signal can be studied. This pixel response study was done with both the 910 nm laser and 1060 nm.

For the 910 nm study, the laser beam power was varied by decreasing the working supply voltage. Four different voltages have been set, with a maximum of 25V. For each data acquisition, the mean value of the gaussian fit of both the seed and cluster distribution has been obtained. The plots of the mean values of the seed and cluster signal, as a function of the correspondent signal measured with the photodiode, are shown in Fig.5.10. Both sets of data, related to the seed signals and to the cluster signals, show a linear behaviour which is confirmed by the results of the linear interpolation. The slope of the fit of the points related to the cluster signal is larger with respect to the seed, reflecting the fact that, with increasing laser power, the multiplicity goes up and the relative signal of the cluster pixels with respect to the single seed pixel increases.

A similar measurement was performed also using the 1060 nm in the same range of signals on the sensor, but the considerations in 5.2.2 were applied. As in the 910 nm case, the laser pulse power was varied lowering the supply voltage, that has been set to five different values in the range [14, 34] V. For each supply voltage value, the data acquired with the sensor were analysed and the mean value

of the gaussian fit of the cluster distribution is obtained, converting into electrons always using the calibration factor given in 4.1. For the last two data sets, a higher seed threshold (12 instead of 6) was used, as explained in 5.2.2. Having modified the seed threshold only for few experimental points, only the cluster signal response is tested. The values are plotted as a function of the correspondent simultaneous signal, in electrons, measured with the photodiode, as can be seen in Fig.5.11. The data show a linear dependency; however, the result of the fit is worse than the one related to the 910 nm.

As discussed in 3.2.2 and 4.2.1, the laser is externally triggered by MATISSE so that, for every acquisition frame, a laser pulse arrives on the sensor. However the photodiode acquisition is much slower as it runs at a frequency of about 1Hz. Consequently the statistical uncertainty of photodiode measurements are always much larger than the sensor ones.

In both studies, the linearity is proved, however the slopes of the two fits are not comparable. This is to be expected as the ratio of photons absorbed in the photodiode and in the sensor changes with wavelength, due to the different absorption coefficient and different thickness of the two devices.

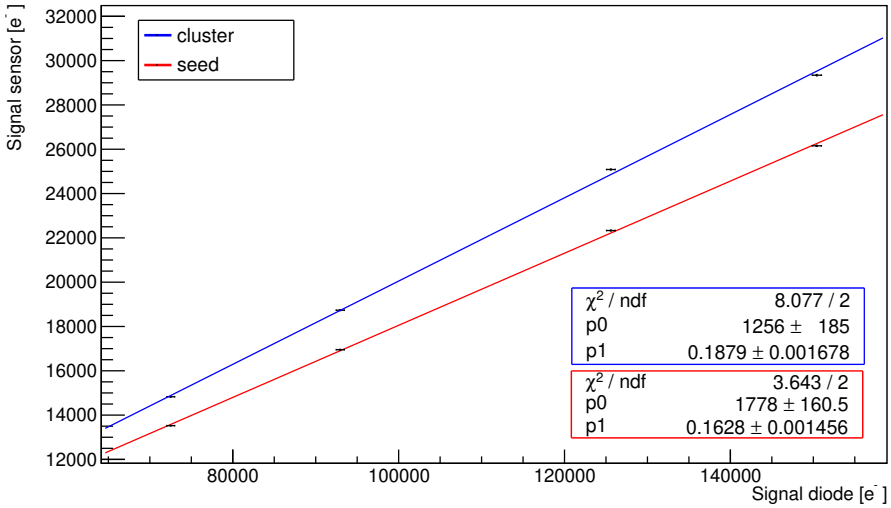

Figure 5.10: Response of the sensor with respect to the signal on the photodiode done with the 910 nm

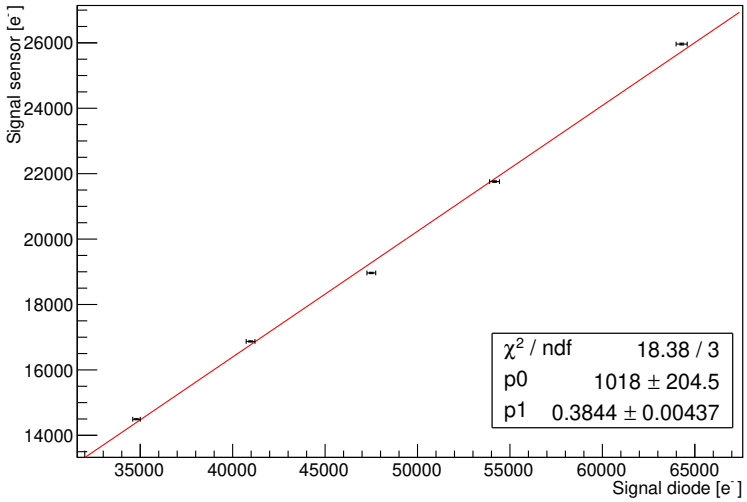

Figure 5.11: Response of the sensor with respect to the signal on the photodiode done with the 1060 nm

In the rest of the measurements presented the 910 nm wavelength is used, because it shows a much better performance in terms of beam spot size, and therefore cluster multiplicity, and shows none of the spurious effects related to the long absorption depths discussed in 5.2.2.

5.4 Response of pixels at different positions

One of the most significant advantages of using a laser pulsed beam source is that the sensor can be moved to perform measurements in well defined positions. In this section, we describe measurements carried out to test the performance, in terms of spatial control and alignments. These measurements have been done in column 14 and 15, which are at the centre of sector 2 and have the largest number of accessible pixels.

Column scan

The motorised stage has been used to perform a scan of some of the pixels in column 15, starting from pixel (15, 19). As it can be seen in Fig.5.13, the scan was done up to row 13, moving in steps that correspond to the size of the pixel pitch, e.g. 50 µm. At every position, the data have been analysed building clusters in 5×5 matrix. It has to be mentioned that these measurements have not been normalised to the reference signal; for this reason the height of the seed pixels is not uniform.

From the 2D cluster map obtained for every position, the centroid is computed. In Fig.5.13b, one can observe how it changes while moving the sensor. The maximum displacement, along the motion, is equal to Δx = (-4.512 ± 0.003) µm and Δy = (5.317 ± 0.003) µm.

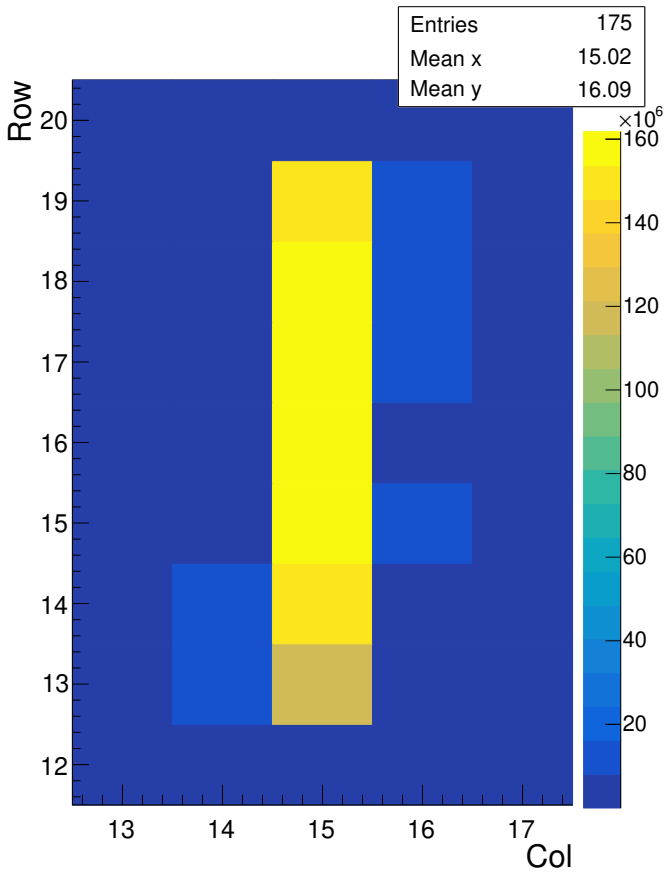

(a) 2D cluster signal map along the scan (z-coordinate unit is ADC counts)

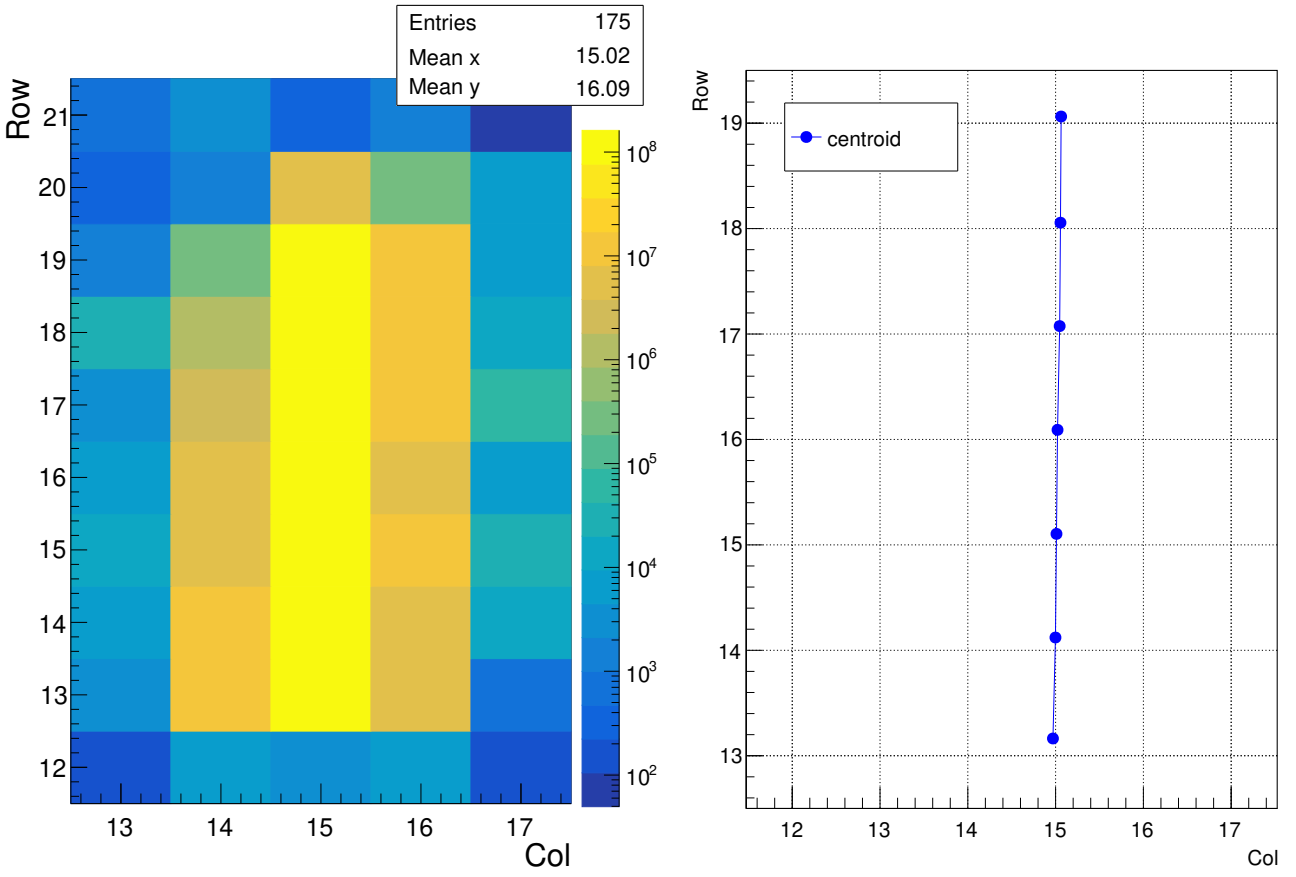

(a) 2D cluster signal map along the scan (log scale)

(b) Centroid position along the scan

Figure 5.13: Measurement moving the laser along one column with steps of 50.0 µm

Signal comparison of two pixels of the same column

The aim of this measurement is to compare the signal measured at two different positions, keeping the same laser settings and optical configuration, and then performing two sequential measurements. The beam spot was centered in pixel (14,17), using the fine motion of the xy stage. A step of 400 µm in the vertical direction was done to hit the pixel with indices (14,9).

Aiming at comparing the signal at two different position, to have a more accurate estimate of the uncertainty on the total collected charge, the fit is perfomed on the histogram in ADC counts. Then, the mean value of the gaussian fit is converted into electrons using the calibration factor. To compute the uncertainty on the signal in electrons, both the uncertainty on the calibration factor and the uncertainty on the mean value in ADC obtained from the fit are propagated. During the data acquisition, about 250 wavepulses were saved and the signal released in the photodiode in terms of electrons is obtained starting from the mean value of the histograms in 5.14e and 5.14f using the calibration in 3.2. The ratio between the sensor and the reference signal can then be computed.

The seed and cluster signal histograms, and the photodiode histogram are shown in Fig.5.14, respectively in ADC and volts (V). All the results are given in Tab.5.3 with the associated uncertainties computed by error propagation.

Looking at Fig.5.14 and comparing the seed and cluster signal distribution, the seed signal is equal to the 82% of the cluster signal for pixel (14,17) and to 78% for pixel (14,9). This is due to the fact that the beam spot gets slightly off center. In particular, it can be clearly seen in Fig.5.15 that, after moving the sensor, the pixels on the upper part of the matrix are contributing more to the total cluster signal. This means that the sensor was moved an effective distance that is less than the actual set length. Computing the difference between the x- and y- centroid coordinates, shown in Fig.5.15a and

Fig.5.15b, and considering only the statistical uncertainties, the results are $\Delta x = (2.6770 \pm 0.0008)$ µm and $\Delta y = (394.1960 \pm 0.0007)$ µm.

Table 5.3: Comparison of the cluster normalised signal of the two pixels

pixel coordinate	cluster signal (e^-)	photodiode signal (e^-)	cluster signal/photodiode signal
(14,17)	22660 ± 30	32700 ± 200	0.695 ± 0.004
(14,9)	23620 ± 30	33400 ± 200	0.707 ± 0.004

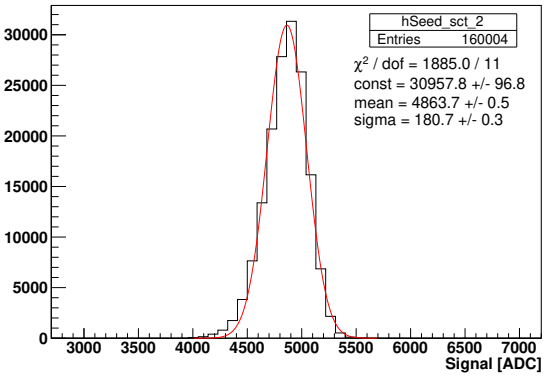

(a) Seed signal pixel(14,17)

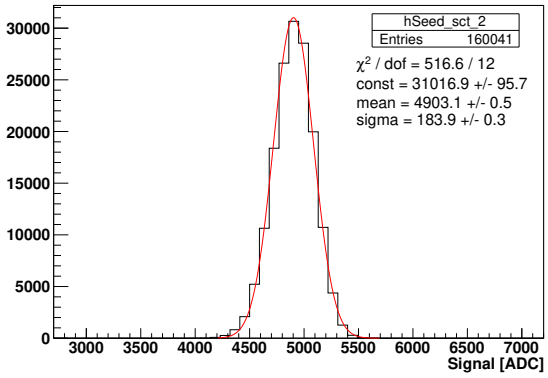

(b) Seed signal pixel(14,9)

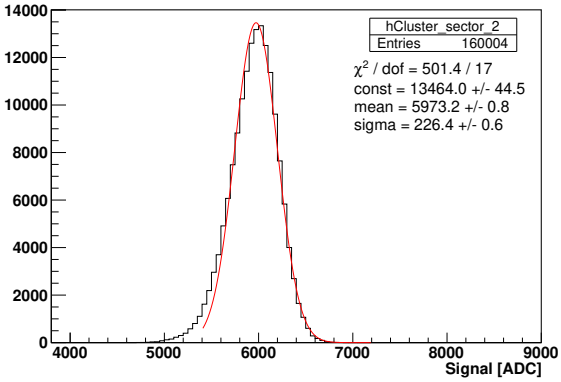

(c) Cluster signal pixel(14,17)

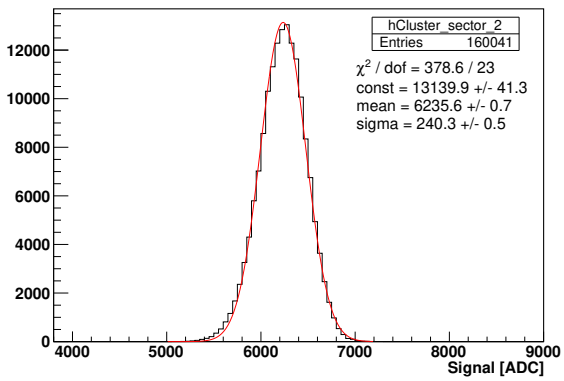

(d) Cluster signal pixel(14,9)

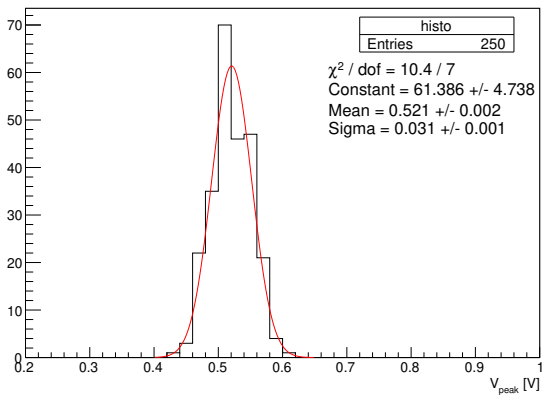

(e) Photodiode signal for the run on pixel(14,17)

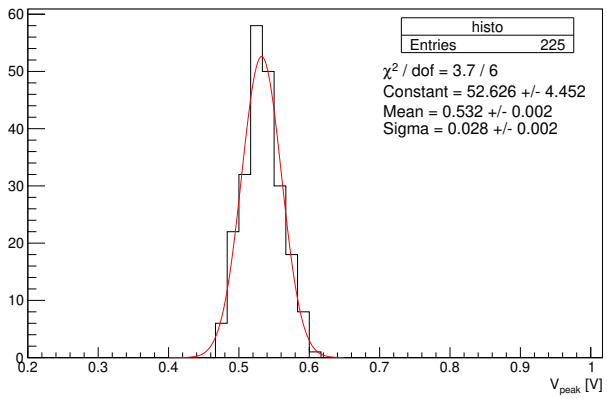

(f) Photodiode signal for the run on pixel(14,9)

Figure 5.14: Measurement with the same laser beam conditions on two different pixels of Sector 2

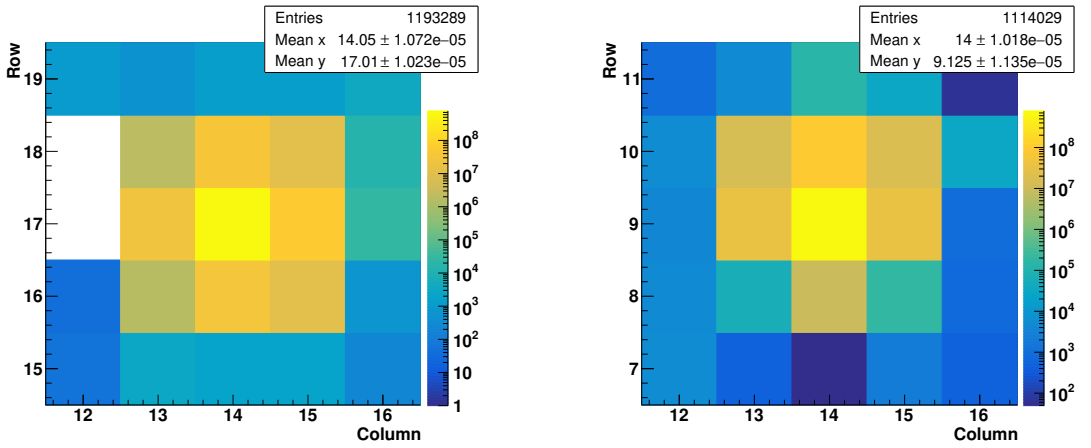

(a) 2D cluster map for seed pixel (14,17) in log scale

(b) 2D cluster map for seed pixel (14,9) in log scale

Figure 5.15: Measurement with the same laser beam conditions on two different pixels of Sector 2

This measurement shows that, even moving a distance that is 8 times larger than the pixel pitch (50 µm), the signals are still comparable. The two ratio of the signals are given in Tab.5.3. Given the uncertainties, the two values are compatible within 2σ.

The ratio in Tab.5.3 cannot be simply compared with the fit results shown in 5.3. In 5.3 the measurements regarding the linear response of pixel were performed with a different optical configuration, both in terms of position of the lens and the setting of diaphragm before the splitter, to attenuate the laser beam at the sensor position without affecting too much the signal on the photodiode. The two optical arms are not symmetric: they have a different length and have different components. This has been done in order to have a signal on the photodiode that is always much larger then the one on the sensor, because the photodiode can measure a large photon flux whereas the pixels saturate at a relatively small number of photons per pulse.

It was verified that, as expected, the ratio between the signal at the reference position and at the sensor position is constant if the position of the lens and the diaphragm setting are not changed.

5.5 Linear scan of single pixel

With the xy translation stage, it is possible to perform a micrometric scan of a single pixel to characterise the uniformity of charge collection. In the following subsections, two studies with this aim are presented. The two cases are:

- First scan: a horizontal direction, with a number of incident photons/pulse on the sensor of the order of 13000.
- Second scan: a vertical direction, with number of incident photons/pulse on the sensor of the order of 5000.

The ideal experimental condition would be to send the laser pulses at the centre of the side of a single pixel and perform measurements while moving the sensor in a specific direction. However, this is very challenging. With the setup, it is not possible to see the laser spot on the sensor with the CMOS camera, for several reasons: the distance between camera and sensor is large; the camera in use is not optimised for the IR range, and the laser beam is pulsed with a very low power. The only tool available, before performing the offline analysis, is the online visualisation of the pixel matrix given by the acquisition software (see Fig.4.4).

The sensor was moved in steps of 5µm in order to scan one pixel along its full length. Given the specification of the xy stage (see 3.1.3), an uncertainty equal to the bidirectional repeatability, i.e.

± 1.0 µm, was assigned to the position of the sensor in these measurements. Both acquisitions have been performed using the 910 nm pulsed laser beam, setting the supply voltage to 25V and 14.2V.

5.5.1 Horizontal direction

The sensor was positioned so that the laser spot straddles between two pixels (column 17 and 16, row 10) and then moved in steps of 5 µm, for a total of 11 steps, to horizontally scan pixel (16,10).

For each position, an acquisition run of 20 spills has been performed. The mean value of the gaussian fit of the seed histogram is used to estimate the charge collected by the pixel, and then plotted as a function of the position in Fig.5.16. The seed signal is normalised to the reference signal of the photodiode.

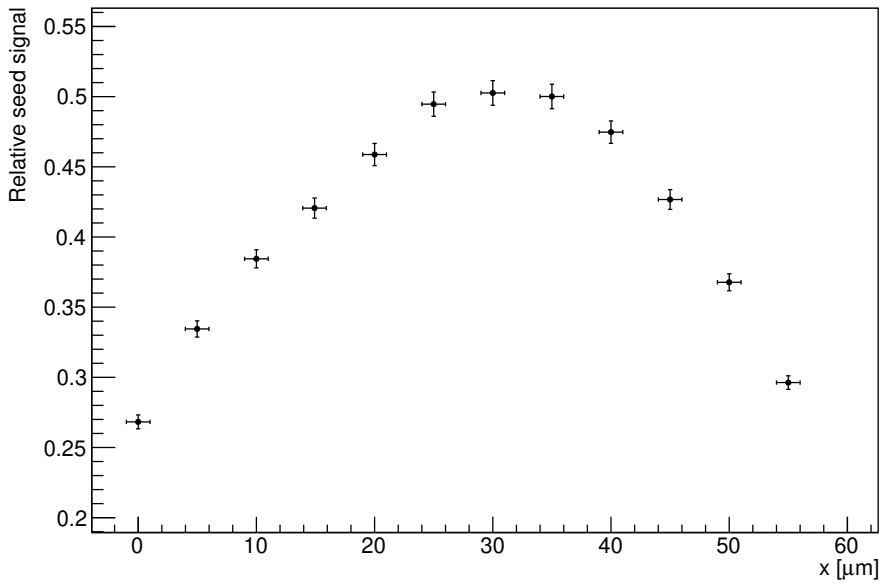

Figure 5.16: Seed signal as a function of the position of the sensor

The plot is shown in Fig.5.16. As expected, the seed signal increases, gets to a maximum, and then decreases. Comparing the value of the relative seed signal at the first position and the maximum value, the first is equal to the 53% of the latter: such a condition is consistent with the fact that the generated charge is collected mainly by two pixels if the laser spot is centered in between them. However, the data behaviour is asymmetric: the falling slope is larger than the rising slope. In fact, the relative signal goes back to its initial level after 55µm, that is larger than the pixel size. In addition, the maximum value of the relative signal occurs at about 30µm, instead of at 25 µm which is the centre of the pixel.

To explain these results, a detailed analysis has been done. In this case, the pixel that is horizontally scanned is located at column 16, which is one column away from sector 3, as the sector 2 spans from column 12 to column 17. For this reason, 3×3 matrices were considered in the presented cluster maps. It has been verified that this choice does not affect the analysis performed because in the 3×3 matrix the relative signal of the surrounding pixels with respect to the seed one is very low; considering even more pixels would make no difference. First of all, looking at the 2D map built around the seed pixel of the first and last measurement of the scan (see Fig.5.17), it can be seen that the signal distribution is displaced in both x and y direction, resulting in Δx = (-44.231 ± 0.001) µm and Δy = (-6.339 ± 0.007) µm.

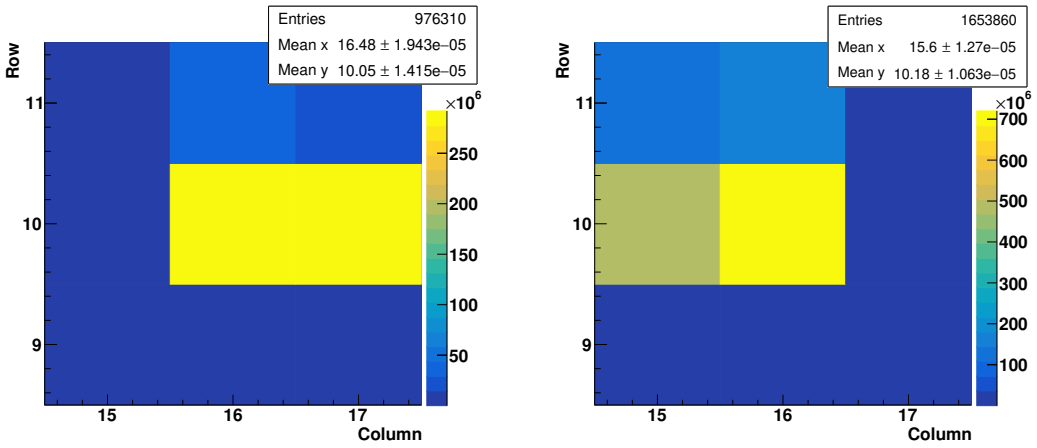

(a) First position x = 0 µm (b) Last position x = -55 µm

Figure 5.17: 3x3 matrix around the seed pixel for the initial and final position

We conclude that the measurement was along a diagonal direction, rather than purely horizontally[3]. The effective length scanned can be estimated to be equal to (44.7 ± 0.1) µm. As a result of these considerations, the x-axis in the following plot has been rescaled to take into account this effect.

Another issue due to the non negligible displacement in the y-direction (that is about 12% of the pixel size) is that, while performing the scan, a charge sharing effect occurred: part of the charge generated was indeed collected by the pixels on the upper row, and therefore did not contribute to the seed signal. The analysis has been redone considering the seed pixel of row 10 and the three pixels on top (row 9; column 15, 16, 17).

The result is shown in Fig.5.18. It can be seen that the behaviour is much more symmetric, and the maximum signal occurs at the centre of the pixel, i.e. about 25 µm. [4]

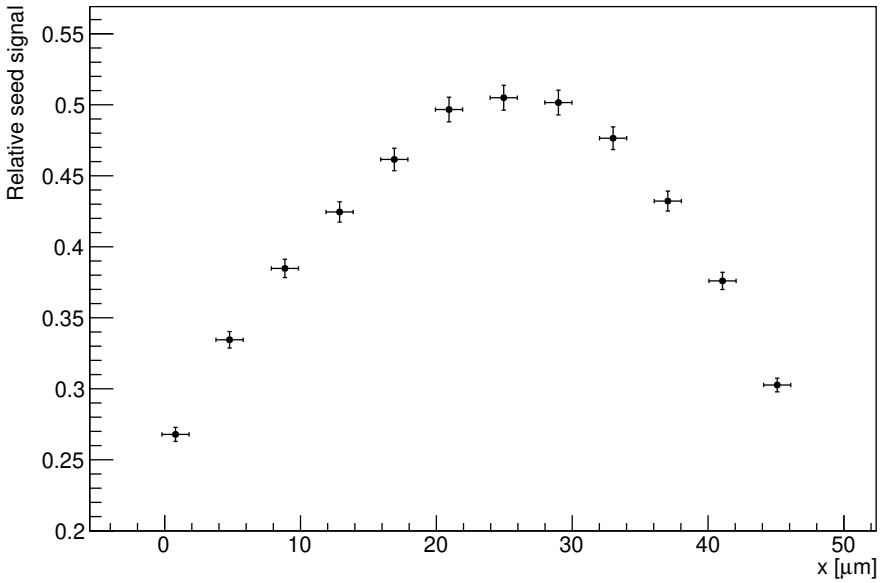

Figure 5.18: Seed signal as a function of the position of the sensor with misalignment corrections (horizontal scan)

[3]The cause of this not perfectly horizontal motion is not clear at the time of writing. It could be an effect of the chip being slightly rotated with respect to the board or that the stepper motor is not perfect.

[4]Another step would have been needed to cover the full pixel length; however, at the time of the measurement, we were not yet aware that the motion was diagonal.

5.5.2 Vertical direction

Recalling the considerations in 5.2.3, the vertical scan was done lowering the laser power in order to get a smaller number of photons. so to limit the charge sharing effects with other pixels.

The pixel (14,13) is scanned along the vertical direction with 11 steps of 5µm. The fit of the seed histogram is computed and the result, in electrons, is normalised to the reference signal.

The result is shown in Fig.5.19. The plot is symmetric and required no corrections: the charge collection with other pixels, in this vertical motion, is negligible. For this $\Delta y = 50$ µm motion, the seed signal is restored to the initial value (x = 0), and, scanning up to 55µm, the curve rises again as the laser enters the adjacent pixel on the same column.

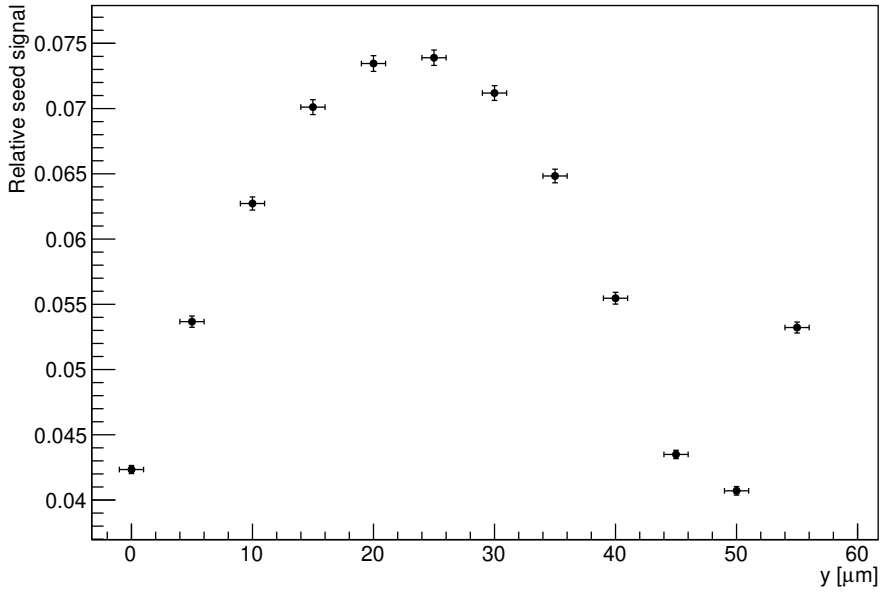

Figure 5.19: Seed signal as a function of the position of the sensor (vertical scan)

From both analysis, the behaviour of charge collection in the vertical and horizontal directions in terms is similar and smooth, that was foreseen as the sensing diode is found at the centre of every pixel cell as seen in Fig.4.2.

Chapter 6

Discussion and prospects

In the context of the research activities on future trackers for which several new MAPS prototypes are being developed, characterisation studies with the use of lasers represent an easy and convenient approach that can be adopted in addition to test beams.

With the measurements and analysis performed in Section 5, the proposed table-top setup has been tested in detail. The setup is a useful tool for MAPS characterisation, and the implementation of laser pulses for sensor characterisation comes with several features that were validated:

- *Compactness and versatility*: it is a very compact and versatile setup because, switching the optical fibre, different pulsed laser beams sources can be used. The working wavelength is chosen based on the characteristics, thickness, and geometry of the device.
- *Large statistics measurements*: compared, for instance, to measurements done with radioactive sources, it is possible to perform measurements with very large statistics in a short time. By implementing the external trigger of the laser source, a laser pulse can be made to occur within every acquisition time window of the device, as is done during the characterisation measurements.
- *Spatial control and sensor scans*: measurements can be performed at specific positions of a device under test by moving it with micrometric precision using motorised translation stages. As the current R&D activities on MAPS aim at developing larger sensors, laser tests could be used to test the uniformity of large pixel matrices.
- *Control on the signal generated on the sensor*: it has been shown that it is feasible to have a signal, in terms of total released charge in the sensor, equivalent to the signal generated by a MIP, with the current setup. In addition, it is possible, acting on the optics and laser settings, to vary the laser power, and, consequently, the number of photons arriving at the sensor. The drawback of laser sources is that they are often unstable in terms of power in time, being subject to fluctuations and thermal drifts; however, this can be monitored and corrected for by implementing a simultaneous power measurement system, as was demonstrated with the photodiode power meter system.
- *Single-pixel characterisation*: the measurements with MATISSE prove that it is possible to characterise and study the response and charge collection of single pixels of size of the O(50 μ m), given the characteristics of the laser beam, in terms of depth of field and radius, achieved with the current optical system.

Limits of the current setup and possible improvements

Some considerations can be made about improvements and developments of the current setup concept and implementation.

- *Vertical motion control*: the current setup does not provide a fine motorised z-axis translation stage; at present the focusing of the laser beam on the sensor is made using the z manual

translation stage of the bearing structure. Implementing an xyz motorised stage to move the device under test, it would be possible not only to have a much higher accuracy in the focusing of the laser on the sensor, but also to perform z scans of the sensor.

- *Photodiode acquisition system*: the acquisition system currently implemented for the photodiode is limited. With regard to the acquisition rate, the bottleneck is represented by the process of saving the waveforms measured with the oscilloscope on the computer. Ways to speed up this process could be tested. In the case of MATISSE, or any chip that can be readout with the same DAQ system, a more ambitious approach would be to digitise the photodiode output signal and send it to one of the DAQ channels. This way the signal measured with the photodiode would be acquired as an additional information related to the corresponding frame of the sensor. This way it would be possible to perform a normalisation of the sensor signal on a pulse by pulse basis and not an average normalisation on the full acquisition run.
- *Automatisation of the translation stage motion*: As mentioned in 4.2.1, it would be useful to implement a system that externally triggers the motion stage: once the acquisition run stops the motion of the stage starts, the acquisition run restarts automatically after the translation of the stage is finished, and stops after a preset number of acquisitions.
- *Visualisation of the beam spot on the sensor surface*: this would require having a camera with very high sensitivity in the IR range. This would be extremely useful when testing sensors that do not provide acquisition software with the online visualisation of the signals. In the MATISSE case, the real time cluster visualisation was very helpful in finding the focus and checking if the laser beam was hitting the sensor at the right position.

Characterisation of other types of MAPS

It must be noted that, due to time constraints, the measurements were performed with one single chip, MATISSE, which, as discussed, has some peculiar features: being fully depleted, thick, and providing access to backside illumination. The latter feature is essential: it is very unlikely that photons arrive inside the active region if the sensor is illuminated from the top, where many metal layers are present[1].

For future development, this setup can be used to test other types of sensors.

Fully depleted MAPS with smaller thickness can be tested with wavelengths of the order of 900 nm, reducing the effects related to the strong absorption that occur when dealing with sensors with a large thickness and having a more uniform release of charge in the sensor. If the beam traverses a shorter path in silicon, it is easier to keep the beam focused, and this would make it feasible to test and characterise the response of single pixels, even in the case of a smaller pixel pitch. The 910 nm and 1060 nm wavlengths used in the study of MATISSE were not the ideal working wavelengths because the first is characterised by an attenuation length that is about 8 times smaller than the sensor thickness and the latter one about 3 times larger.

MAPS with a fully depleted epitaxial layer can be studied using long wavelengths in the IR range because, in this case, photons have to traverse the full thickness of the substrate before entering the epitaxial layer that represents the active region where charges are collected by drift. This study would be extremely interesting, since the exponential absorption of photons is less relevant if the depth is very short and the signal induced by the laser would be much more comparable with a MIP signal in terms of charge density.

[1] As an example, the ALPIDE chip has 11 µm of metal layers on top.

Conclusions

We successfully designed, built, and validated a fully working, pulsed laser beam table-top setup for testing MAPS. The photoelectron signal induced in the device under test emulates MIP signals. We demonstrated that it can be used to perform characterisation studies of the device, in terms of linearity of the response of pixels and uniformity of charge collection with respect to the injection point within the pixel cell. To commission the setup in preparation of the ALICE sensors testing, we used it to test a well known sensor, the MATISSE, and verified that the results indeed match the known literature, and previous test campaigns. Other than the ALICE sensors test campaign, the system will be very useful to carry out other characterisation campaigns of sensor during their R&D phase, when many different chip flavours and versions are produced. Furthermore, the specific setup and, more in general, the laser technique we developed, could be further improved to allow studying other semiconductor sensor properties, as the 3D shape of the depleted volume in pixel devices.

Appendix

Gaussian Beam Optics

The formal description of laser beam propagation is based on the theory of Gaussian beams. [18]
A gaussian beam is one of the solutions of the Helmholtz paraxial equation.
Requiring that a wavefronts with a complex amplitude, that is a perturbation of a plain waveform, satisfy the Helmholtz paraxial equation, one can get the gaussian beam solution:

$$U(\vec{r}) = \frac{A}{q(z)} e^{-ik\frac{\rho^2}{2q(z)}} e^{-ikz} \tag{A.1}$$

where $q(z) = z + iz_R$ with z_R known as the Rayleigh parameter. The function $q(z)$ can be rewritten highlighting the real and complex part.

$$\frac{1}{q(z)} = \frac{1}{R(z)} - i\frac{\lambda}{\pi w^2(z)} \tag{A.2}$$

Therefore, the complex amplitude can be rewritten as:

$$U(\vec{r}) = A_0 \frac{w_0}{w(z)} \left[e^{-\frac{\rho^2}{w^2(z)}} \right] \cdot \exp\left[-i\left(k\left(z + \frac{\rho^2}{2R(z)} \right) - \tan^{-1}\left(\frac{z}{z_R} \right) \right) \right] \tag{A.3}$$

From the complex amplitude, the intensity is directly derived:

$$I(\vec{r}) = |U(\vec{r})|^2 \implies I(\rho, z) = I_0 \left[\frac{w_0}{w(z)} \right]^2 e^{-\frac{2\rho^2}{w^2(z)}} \tag{A.4}$$

At a fixed z, the intensity is a gaussian function and this gives the name of gaussian beam to this particular solution.
The width is related to the beam waist $w(z)$. Computing the power of the gaussian beam as the integral of the intensity on the beam section:

$$P_{tot} = \int_0^\infty I(\rho, z) 2\pi\rho d\rho = \frac{I_0}{2}\pi w_0^2 \tag{A.5}$$

Integrating instead from 0 to $w(z)$, it is obtained that the ∼86% of the power is transported inside the radius $w(z)$.
For this reason, $w(z)$ is assumed as the radius of the gaussian beam spot.
The geometry of the gaussian beam is completely determined by the Rayleigh parameter, in fact:

$$w(z) = w_0 \sqrt{1 + \left(\frac{z - z_0}{z_R} \right)^2} \quad with \quad w(0) = \sqrt{\frac{\lambda z_R}{\pi}} \tag{A.6}$$

The Eq.A.6 describes the beam waist as a function of z, the coordinate along the direction of propagation.

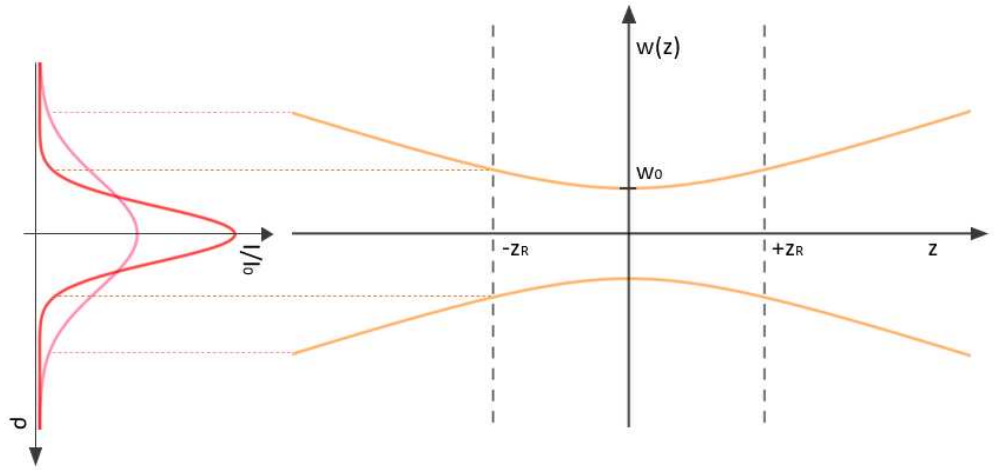

Figure 6.1: Gaussian beam propagation: beam waist as a function of z and beam intensity at fixed z

At z=z_0, the beam is focused: the beam has the minimum waist $w_0 = w(z_0)$. For $|z| > z_0$, the beam waist increases.

It is defined as depth of field the range $2z_R$ in which it can be assumed that the beam waist stays almost constant.
In fact, at $z = z_0 \pm z_R$, the beam waist is enhanced by a factor $\sqrt{2}$.
Therefore, as a practical description of laser beam propagation, the two fundamental quantities are the depth of focus $2z_R$, which tells us where we can assume that the beam stays focused, and the minimum spot size w_0.

Bibliography

[1] M. Battaglia, D. Bisello, D. Contarato, P. Giubilato, D. Pantano, and M. Tessaro. A DAQ system for pixel detectors R&D. *Nuclear Instruments and Methods in Physics Research A*, 611(1):105–110, November 2009. doi:10.1016/j.nima.2009.09.008.

[2] R. Brun and F. Rademakers. Root - an object oriented data analysis framework. *Nuclear Instruments and Methods in Physics Research Section A*, 389(81), 1997. New Computing Techniques in Physics Research V, See also http://root.cern.ch/, Release v6.28/04, 07/05/2023. URL: https://www.sciencedirect.com/science/article/pii/S016890029700048X, doi:https://doi.org/10.1016/S0168-9002(97)00048-X.

[3] M. Buckland. Development of the its3: A bent-silicon vertex detector for alice in the lhc run 4. *Nuclear Instruments and Methods in Physics Research Section A: Accelerators, Spectrometers, Detectors and Associated Equipment*, 1039:166875, 2022. URL: https://www.sciencedirect.com/science/article/pii/S0168900222003436, doi:https://doi.org/10.1016/j.nima.2022.166875.

[4] ALICE Collaboration. Letter of intent for ALICE 3: A next generation heavy-ion experiment at the LHC. Technical report, CERN, Geneva, 2022. 202 pages, 103 captioned figures, 19 tables. URL: https://cds.cern.ch/record/2803563, arXiv:2211.02491.

[5] B Abelev et al and (The ALICE Collaboration). Upgrade of the alice experiment: Letter of intent. *Journal of Physics G: Nuclear and Particle Physics*, 41(8):087001, jul 2014. URL: https://dx.doi.org/10.1088/0954-3899/41/8/087001, doi:10.1088/0954-3899/41/8/087001.

[6] Maurice Garcia-Sciveres and Norbert Wermes. A review of advances in pixel detectors for experiments with high rate and radiation. *Reports on Progress in Physics*, 81(6):066101, 05 2018. URL: https://doi.org/10.1088%2F1361-6633%2Faab064, doi:10.1088/1361-6633/aab064.

[7] Martin A Green. Improved silicon optical parameters at 25° c, 295 k and 300 k including temperature coefficients. *Progress in Photovoltaics: Research and Applications*, 30(2):164–179, 2022. doi:10.1002/pip.3474.

[8] Fox Mark. *Optical Properties of Solids.* Number Vol. 3 in Condensed Matter Physics. OUP Oxford, 2nd edition edition, 2010. URL: https://search.ebscohost.com/login.aspx?direct=true&db=nlebk&AN=702066&site=ehost-live.

[9] M. Munker, M. Benoit, D. Dannheim, A. Fenigstein, T. Kugathasan, T. Leitner, H. Pernegger, P. Riedler, and W. Snoeys. Simulations of CMOS pixel sensors with a small collection electrode, improved for a faster charge collection and increased radiation tolerance. *Journal of Instrumentation*, 14(05):C05013–C05013, may 2019. URL: https://doi.org/10.1088%2F1748-0221%2F14%2F05%2Fc05013, doi:10.1088/1748-0221/14/05/c05013.

[10] Francesco Noferini and on behalf of the ALICE Collaboration. Alice results from run-1 and run-2 and perspectives for run-3 and run-4. *Journal of Physics: Conference Series*, 1014(1):012010, 05 2018. URL: https://dx.doi.org/10.1088/1742-6596/1014/1/012010, doi:10.1088/1742-6596/1014/1/012010.

[11] Elias Jonhatan Olave, Serena Mattiazzo, Serena Panati, Fabio Cossio, Angelo Rivetti, Devis Pantano, Natale Demaria, Lucio Pancheri, Piero Giubilato, and Manuel Dionisio Da Rocha Rolo. MATISSE: a Low Power Front-End Electronics for MAPS Characterization. *PoS*, TWEPP-17:016, 2018. doi:10.22323/1.313.0016.

[12] Serena Panati, J. Olave, A. Rivetti, L. Pancheri, F. Cossio, P. Giubilato, D. Pantano, S. Mattiazzo, M. D. Da Rocha Rolo, and N. Demaria. Matisse: A versatile readout electronics for monolithic active pixel sensors characterization. In *2017 IEEE Nuclear Science Symposium and Medical Imaging Conference (NSS/MIC)*, pages 1–4, 2017. doi:10.1109/NSSMIC.2017.8532806.

[13] Lucio Pancheri, Raffaele A. Giampaolo, Andrea Di Salvo, Serena Mattiazzo, Thomas Corradino, Piero Giubilato, Romualdo Santoro, Massimo Caccia, Giovanni Margutti, Jonhatan E. Olave, Manuel Rolo, and Angelo Rivetti. Fully depleted maps in 110-nm cmos process with 100—300-µm active substrate. *IEEE Transactions on Electron Devices*, 67(6):2393–2399, 2020. doi:10.1109/TED.2020.2985639.

[14] F. Reidt. Upgrade of the ALICE ITS detector. *Nuclear Instruments and Methods in Physics Research Section A: Accelerators, Spectrometers, Detectors and Associated Equipment*, 1032:166632, jun 2022. URL: https://doi.org/10.1016%2Fj.nima.2022.166632, doi:10.1016/j.nima.2022.166632.

[15] Arganda-Carreras I. Frise E. Kaynig V. Longair M. Pietzsch T. ... Cardona A. Schindelin, J. Fiji: an open-source platform for biological-image analysis. *Nature Methods*, 9(7):676–682, 2012. doi:doi:10.1038/nmeth.2019.

[16] SEED Project INFN Sez. Torino. *MATISSE USER GUIDE*, 06 2016.

[17] Sally Seidel. Silicon strip and pixel detectors for particle physics experiments. *Physics Reports*, 828(C), 10 2019. URL: https://www.osti.gov/biblio/1803557, doi:10.1016/j.physrep.2019.09.003.

[18] O. Svelto. *Principles of Lasers*. Springer, 2010. URL: https://books.google.it/books?id=KxyJcgAACAAJ.

[19] Arturo Tauro. ALICE Schematics. General Photo, 2017. URL: https://cds.cern.ch/record/2263642.

[20] N. Wermes. Pixel detectors for charged particles. *Nuclear Instruments and Methods in Physics Research Section A: Accelerators, Spectrometers, Detectors and Associated Equipment*, 604(1-2):370–379, jun 2009. URL: https://doi.org/10.1016%2Fj.nima.2009.01.098, doi:10.1016/j.nima.2009.01.098.